Università degli Studi di Padova

Sede Amministrativa: Università degli Studi di Padova

Dipartimento di Biologia

SCUOLA DI DOTTORATO DI RICERCA IN BIOSCIENZE E BIOTECNOLOGIE
INDIRIZZO BIOTECNOLOGIE
CICLO XXV

ENTRAPMENT OF HEMOCYANIN CONFORMERS AS A TOOL FOR THE DEFINITION OF THE STRUCTURAL MODEL OF COOPERATIVITY

Direttore della Scuola : Ch.mo Prof. Giuseppe Zanotti
Coordinatore d'indirizzo: Ch.mo Prof. Giorgio Valle
Supervisore: Ch.mo Prof. Mariano Beltramini

Dottorando: Fabrizio Minute

Abstract

Allostery has been established as a fundamental mechanism of regulation in most biological processes (Changeux, 2012). The most studied allosteric protein is hemoglobin, that has long been considered a paradigm for the investigation of allostery and cooperativity in macromolecules (Cui & Karplus, 2008). A phenomenological characterization of the cooperative oxygen binding in hemoglobin has been given by the classic Monod, Wyman, Changeux model (MWC) (Monod et al., 1965), which described the cooperativity process as the allosteric transition between two different allosteric conformers: the high oxygen affinity R-state and the low oxygen affinity T-state.

In this work we wanted to characterize the highly cooperative oxygen binding process of the hemocyanin (in its dodecameric state) from the arthropod *Carcinus aesturaii*, which represents a more complex case study. To this aim the functional and structural properties of the different conformational states were investigated, through the encapsulation of the hemocyanin into a sol-gel matrix to avoid the allosteric transition between T- and R-state.

Firstly we characterized the structural and optical properties of the sol-gel matrix in order to find the better conditions for protein encapsulation. The effect of the pH, glycerol and aging time was assessed by collecting Small Angler X-Ray Scattering spectra of undoped sol-gel matrices at ELETTRA (Trieste, Italy). The fractal analysis of all the spectra did not evidence any significant effect of the three factors on the properties of the matrix, with the exception of the decrease of the radius of the silica particles that form the gel network in presence of glycerol. Moreover, the spectroscopic analysis of the undoped matrix revealed a good transparence of the matrix.

The key point of the work was to evaluate if the sol-gel matrix was a suitable way for the entrapment of hemocyanin in a single conformational state, through the analysis of the oxygen binding curves and the Hill-plots of the hemocyanin entrapped into the silica matrix (in presence and absence of oxygen). The results suggested that the sol-gel matrix can avoid the allosteric transitions, although the full entrapment of distinct conformers strongly depend on the pH. Oxygen binding experiments performed in presence of different concentrations of salt demonstrated that

changes of the charge to charge interactions between protein and matrix may play an important role in conformational entrapment. The entrapment of different conformers was confirmed by spectroscopic analysis that revealed small but significant differences in the shape of the CD-spectra in the aromatic region and shifts of the peaks of fluorescence emission for the two conformers.

To verify if the oxygen equilibrium data were in agreement with the MWC model we compared the equilibrium constants of the curves obtained by the hemocyanin entrapped into the sol-gel with those predicted by the model, suggesting that the cooperativity in this hemocyanin occurs in a more complicated way. A three-state model was proposed.

The validation of the three-state model was performed through Small Angle Neutron Scattering (SANS) measurements at ILL neutron radiation facility (Grenoble, France), that allowed us to characterize the structure of the conformers both in the oxy- and deoxygenated state. The analysis of the SANS spectra seems to confirm the presence of three different conformers, with a different arrangement of the two hexamers.

In order to determine if these differences in the quaternary structure were correlated to changes in the active sties, we collected XAS spectra at ESRF (Grenoble, France), which shown differences between the different conformers, suggesting a different coordination geometry of the active sites in the deoxygenated form.

An investigation of the functional and structural effects of the positive allosteric effector lactate was also performed, by the analysis of oxygen binding curves and SANS spectra.

In conclusion, with this work it is defined a structural model of cooperativity for hemocyanin, with a functional and structural characterization of the different conformers. We also proposed a possible mechanism to describe how the quaternary conformational changes are linked to the different coordination geometry of the active site during the oxygen binding process.

This study method can be exported to other cooperative systems and the results also provide a solid start point for the development of an oxygen biosensor.

Riassunto

L'allosteria rappresenta un meccanismo fondamentale nella regolazione della maggior parte dei processi biologici (Changeux, 2012). La proteina allosterica maggiormente studiata è l'emoglobina, che per molto tempo è stata considerata come un paradigma per lo studio dell'allosteria e della cooperatività nelle macromolecole (Cui & Karplus, 2008). Un caratterizzazione fenomenologica del legame cooperativo dell'ossigeno nell'emoglobina è stata fatta tramite l'applicazione del classico modello di Monod, Wyman e Changeux (MWC), che descrive il processo cooperativo come una transizione allosterica tra due diverse conformeri allosterici: lo stato ad alta affinità per l'ossigeno R, e quello a bassa affinità T.

In questo lavoro il nostro obiettivo era quello di caratterizzare il processo di legame dell'ossigeno, altamente cooperativo, dell'emocianina (in forma dodecamerica) dell'artropode *Carcinus aestuarii*, che rappresenta un caso di studio più complesso rispetto a quello dell'emoglobina. Per questo scopo, le proprietà funzionali e strutturali dei diversi stati conformazionali sono state indagate, attraverso l'incapsulamento dell'emocianina all'interno di una matrice sol-gel che consente di limitare le transizioni allosteriche tra lo stato T e quello R.

Per prima cosa abbiamo caratterizzato le proprietà funzionali e strutturali della matrice sol-gel, in modo tale da trovare le condizioni migliori per l'intrappolamento della proteina. L'effetto del pH, del glicerolo e dell'a*ging* sono stati valutati tramite misure SAXS di matrici senza proteina ad ELETTRA (Trieste, Italia). L'analisi frattale degli spettri non ha evidenziato effetti significativi dei tre fattori sulle proprietà della matrice, con l'eccezione della diminuzione del raggio delle particelle silicee che costituiscono il network del gel, in presenza di glicerolo. Le analisi spettroscopiche della matrice senza proteina inoltre hanno evidenziato una buona trasparenza della matrice.

Il punto cruciale del lavoro era quello di valutare se la matrice sol-gel rappresentava un utile approccio per l'intrappolamento dell'emocianina in un singolo stato conformazionale, attraverso l'analisi delle curve di ossigenazione e dei grafici di Hill dell'emocianina incapsulata nella matrice silicea (in presenza ed assenza di ossigeno). I risultati ottenuti suggeriscono che la matrice sol-gel è in grado di impedire le transizioni allosteriche, anche se il blocco totale dei diversi

conformeri dipende fortemente dal pH. Curve di ossigenazione ottenute in presenza di diverse concentrazioni di sodio cloruro hanno dimostrato che queste differenze sono dovute probabilmente a cambiamenti nell'interazione elettrostatica tra la proteina e la matrice. In ogni caso, l'intrappolamento dei diversi conformeri è stato confermato dalle analisi spettroscopiche che hanno evidenziato piccole ma significative differenze nella forma degli spettri CD nella regione aromatica e spostamenti dei picchi di emissione di fluorescenza dei due conformeri.

Per verificare se i dati dell'equilibrio con l'ossigeno erano in accordo con il modello di MWC, abbiamo confrontato le costanti di equilibrio delle curve ottenute dall'analisi dell'emocainina incapsulata nel sol-gel con quelle predette dal modello, suggerendo per questa emocianina un processo cooperativo più complesso. Un modello a tre stati è stato proposto.

La validazione del modello a tre stati è stato fatta tramite misure SANS a ILL (Grenoble, Francia), che hanno consentito di caratterizzare la struttura dei conformeri, sia nella forma ossigenata che deossigenata. L'analisi degli spettri SANS sembrerebbe confermare la presenza di tre diversi conformeri, contraddistinti da un diverso orientamento spaziale dei due esameri.

Per determinare se queste differenze nella struttura quaternaria erano correlate a cambiamenti del sito attivo, abbiamo effettuato misure XAS a ESRF (Grenoble, Francia) che hanno evidenziato differenze tra i diversi conformeri, suggerendo una diversa geometria dei siti attivi nella forma deossigenata.

Inoltre è stata effettuata un'analisi anche degli effetti funzionali e strutturali del lattato, un effettore allosterico positivo, attraverso l'analisi delle curve di ossigenazione e degli spettri SANS.

In conclusione, con questo lavoro è stato definito un modello strutturale per la cooperatività dell'emocianina, con una caratterizzazione funzionale e strutturale dei diversi conformeri. Abbiamo inoltre proposto un possibile meccanismo per descrivere in che modo i cambiamenti nella struttura quaternaria modificano la coordinazione degli atomi di rame nel sito attivo durante il processo di legame dell'ossigeno.

Questo lavoro può essere preso a modello per lo studio di altri sistemi cooperativi. Inoltre i risultati ottenuti costituiscono un solido punto di partenza per lo sviluppo di biosensori per l'ossigeno.

1 Introduction

In 1935 L. Pauling proposed a model for intramolecular control in hemoglobin to explain the positive cooperativity observed in the binding of oxygen molecules (Pauling, 1935). However only in 1961 the adjective "allosteric" was coined by Jacques Monod and Francois Jacob, to describe the experiments of the PhD student Jean-Pierre Changeux on the enzyme L-threonine deaminase, in which the end-product L-isoleucine inhibit the enzyme without competing with the reactant L-threonine. These experiments represented the start point in the conceptual evolution of the theory that revolutionized the view of the allostery: the two state allosteric model of Monod, Wyman and Changeux, published in 1965 (Monod et al., 1965). This model was in contrast with the other classic allosteric model, the sequential Pauling-KNF model (Koshland et al., 1966).

In the last 20 years, the allosteric models were used to investigate many different biological processes, allowing the characterization of several allosteric systems, including pharmacological receptors for neurotransmitters and other macromolecules involved in intracellular and intercellular communications. Clearly, these models provide just a phenomenological description of experimental observations, and can't explain how allostery occurs at an atomic level. For this reason, it is fundamental to integrate the functional information of the allosteric systems investigated with structural, thermodynamic, and kinetic studies.

1.1 Oxygen binding and transport proteins

1.1.1 Oxygen transport proteins OTPs

In almost all higher organisms, oxygen transport proteins (OTPs), also known as respiratory pigments, have been evolved to bind and transport dioxygen in the blood. The evolution of simple oxygen-binding proteins into multisubunits circulating proteins, simply dissolved in the plasma or carried in circulating cells, made possible the transport of oxygen on a significant scale from the periphery of the organism to metabolizing cells in its interior (Terwillinger, 1998). Indeed, with the increase in size of metazoan animals in the early Cambrian period, the

transport of dioxygen simply dissolved in the blood was not sufficient to the oxygen demand of tissues.

At least three main classes of OTPs can be described, each one with specific structural and functional properties: hemoglobin, hemerythrin and hemocyanin (Decker & van Holde, 2011). In all these proteins, the transport of dioxygen from the gills/lungs to the tissues occurs through the binding of dioxygen to active sites containing either Fe(II) or Cu(I), which change reversibly their oxidation number. The principal characteristics of these proteins are indicated in **Table 1.1**.

Protein type	Phylogenetic distribution (sources)	Metal	Number of O2-binding sites	Localization occurence
Hemoglobin	*Many phyla* Vertebrates Invertebrates (annelids, some arthropods, molluscs, minor phyla)	Fe heme	4 2-144	Intracellular Some intrecellular, some extracellular
Hemerythrin	*Rare, in 3 phyla* Sipincudis, brachiopods, occasionally annelids	Fe-Fe	3-8	Intracellular
Hemocyanin	*2 phyla* Only molluscs Only arthropods	 Cu-Cu Cu-Cu	 70-160 6-48	 Extracellular Extracellular

TABLE 1.1. General characteristics of oxygen transport proteins (Table from Decker & van Holde, 2011)

1.1.2 Allosteric properties of the oxygen transport proteins

1.1.2.1 A definition of allostery

Allostery was defined for the first time by Monod et al., (1965) as "*indirect interactions between distinct binding sites...mediated by some kind of allosteric transition which is induced or stabilized by the protein when it binds an allosteric ligand*". Due to this definition, allostery is associated to proteins characterized by at least two binding sites, located on the same subunit or on different subunits. Furthermore, to be considered an allosteric protein, the two or more binding sites must be in communication one with each other, with the ligand

binding at one site that affects the ligand binding at the second one (Peracchi et al., 2011).

Contrary to simple monomeric oxygen-binding proteins (e.g. myoblobin), almost all the OTPs are multi-subunits proteins exhibiting two types of allosteric interaractions: *homotropic* end *heterotropic*.

Homotropic interactions generally refer to the binding of a ligand to one subunit that affects the binding of the same ligand to other subunits of the protein. This type of interaction is known as *cooperativity* and can be *positive* or *negative*, depending on the amplification or inhibition of the functional activity of the protein, respectively. Heterotropic interactions instead refer to the interactions of different ligands binding at two different sites. Also in this case the functional properties of the protein can be enhanced or inhibited, depending on the nature of o the heteretropic ligand.

In the OTPs, these two types of interactions represent very important mechanisms of regulation of the respiratory physiology, enabling living organisms to adapt to changes of the environmental conditions. Due to the importance of these allosteric properties, the OTPs (in particular human hemoglobin) represent the most studied and well defined allosteric proteins.

1.1.2.2 Cooperative oxygen-binding: physiological implications

In order to better understand why cooperativity has been evolved in respiratory pigments, it's important to briefly described the role of these proteins and what are the advantages of a cooperative oxygen behavior compared to a non cooperative one.

The physiological role of the OTPs is to increase the oxygen capacity of the circulating fluids; the oxygen content of the biological fluid includes both the oxygen bound to the respiratory pigment and the freely dissolved oxygen. The latter represents only a small fraction of the total capacity. Therefore, considering that the oxygen capacity mainly depends on the concentration of the respiratory pigment, the content of oxygen is commonly indicated as *saturation %* of the active sites, allowing the comparison between animals characterized by different concentrations of respiratory pigments.

In **Figure 1.1** two different oxygen binding curves are shown, in which the *saturation %* is expressed as a function of the *partial pressure of oxygen* pO_2. From these curves the oxygen affinity can be quantified; it is conventionally indicated as p_{50}, which corresponds to the partial pressure of oxygen at which the 50% of the active sites are saturated. Low p_{50} values indicate high oxygen affinity, while high p_{50} values low oxygen affinity.

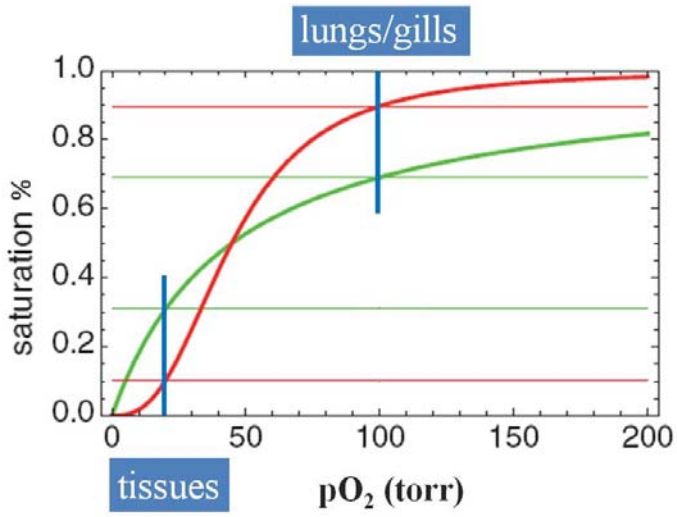

FIGURE 1.1. Hyperbolic (*green*) and sigmoidal (*red*) oxygen-binding curves (Image modified from Ferrel, 2009).

The first observation is the different shapes of the curves, hyperbolic and sigmoid, representative of *non-cooperative* and *cooperative* oxygen binding, respectively.

The adaptive role of the OTPs is to bind a large amount of oxygen in the lungs/gills, where the partial pressure of oxygen is high (about 100 torr in the lungs), and then transport and release it to the peripheral tissues where the oxygen concentration is low.

If we consider the simplest case of a monomeric protein, it can bind a single molecule of oxygen:

$$OTP + O_2 \leftrightarrow OTP \cdot O_2$$

Equation 1.1

The reversible oxygen binding equilibrium can be described by the Langmuir equation:

$$Y = \frac{pO_2}{K + pO_2}$$

Equation 1.2

where Y is the fraction of saturation, pO_2 (torr) the partial pressure of oxygen and K ($torr^{-1}$) the dissociation constant. As shown in **Fig.1.1**, the plot of this equation gives an hyperbola (*green curve*) and allows for an oxygen deliver to the tissues of around 38%. This oxygen behavior perfectly fit the oxygen binding curves of proteins with a single binding site, like myoglobin.

But as we have already seen in **Table 1.1**, the OTPs are characterized by several oxygen binding sites for single molecule. In these cases, the Hill equation (Hill, 1910) will usually considered:

$$Y = \frac{{pO_2}^n}{p50^n + {pO_2}^n}$$

Equation 1.3

wher *n* is the *cooperativity index* (or Hill coefficient) that defines and quantifies the magnitude of the cooperative oxygen binding:

- n = 1 non-cooperative oxygen binding
- n > 1 positive cooperativity
- n < 1 negative cooperativity

Note that if n = 1 (non-cooperative binding) **Eq. 1.3** is reduced to **Eq. 1.2**, wher K = p50. Another way to write the Hill equation (**Eq. 1.4**) is the following:

$$\frac{Y}{1-Y} = \frac{{pO_2}^n}{p50^n}$$

Equation 1.4

As shown in **Fig.1.1,** the fit of this equation results in a sigmoidal oxygen binding curve (*red curve*), with lower O_2 affinity at low pO_2 (tissues) and higher O_2 affinity at high pO_2 (lungs/gills) compared to the non-cooperative curve (*green curve*). This means that cooperative oxygen binding behavior helps the OTPs to pick up more oxygen in the lungs/gills and to unload it more completely to the tissues (~90% of O_2 delivered).

1.1.2.3 Hill-plot: a graphical investigation of cooperativity

A useful tool to rapidly investigate the equilibrium constants of oxygen binding proteins is represented by the Hill-plot. This graph is obtained by the plot of the Hill-equation (**Equation 1.4**), written in its logarithmic form (**Equation 1.5**).

$$\log \frac{Y}{1-Y} = n \log pO_2 - n \, log \, p50$$

Equation 1.5

As it is shown in the representative **Fig. 1.2**, Hill-plots readily identify the differences between non-cooperative (Mb) and cooperative (Hb) oxygen binding behavior.

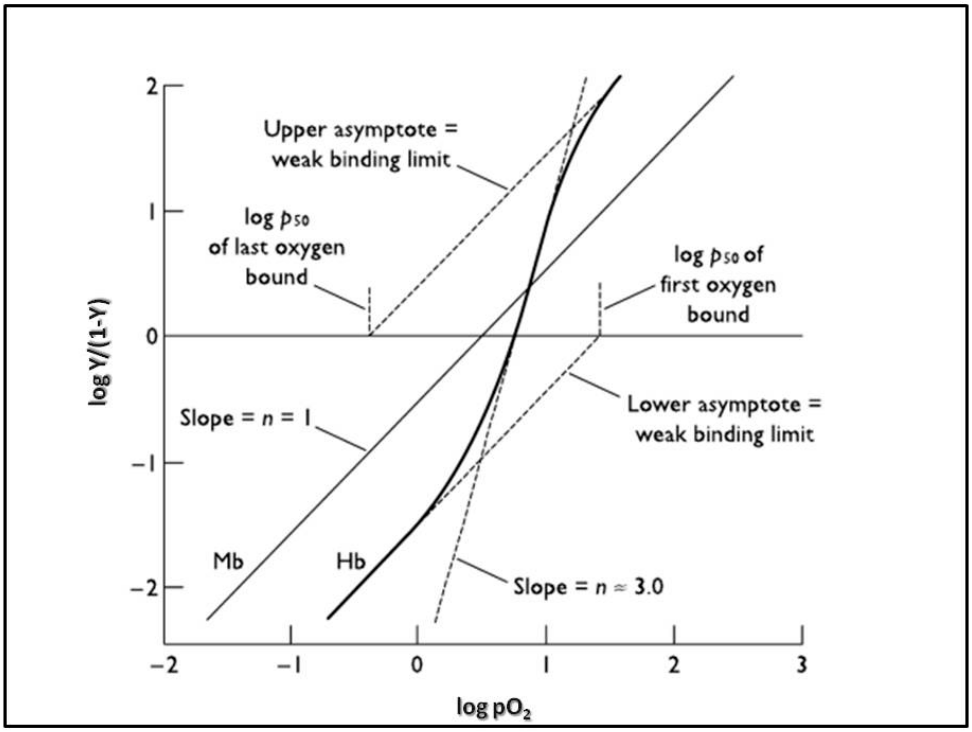

FIGURE 1.2. Hill plot of human myoglobin (Mb) and hemoglobin (Hb) oxygen binding (Image from Haynie, 2008).

For non-cooperative binding a straight line with slope of 1, corresponding to the cooperativity index *n*, is always observed. The curve for cooperative binding instead is more complicated, with the transition between different binding states (depending on the complexity of the cooperativity process). The first and the last binding events are well defined by the upper and lower asymptotes, both

characterized by a slope of 1. The quantification of the cooperative binding instead is given by the slope at log Y/(1-Y)=0. Both for cooperative and non-cooperative proteins the intercept of the line on the log Y/(1-Y)=0 axis gives the log value of p50. Finally, for cooperative proteins is possible to estimate the log p50 of the protein during the first and the last oxygen binding event through the extrapolation of the two asymptotes (**Fig. 1.1**: *dashed lines*).

1.1.2.4 Models of cooperativity

Hill equation is useful as a mathematical tool to quantify the magnitude of a cooperativity process, but it is unrealistic from a molecular perspective. Indeed the assumption of this model is that all oxygen molecules jump onto their binding sites simultaneously, and this seems completely unreasonable at a molecular level. A phenological characterization of the cooperative oxygen binding has been given by the two classic allosteric models: the Monod, Wyman, Changeux (**MWC**) concerted model (Monod et al., 1965) and the Pauling sequential model (Pauling, 1935), later elaborated by Koshland, Nemethy and Filmer (**KNF**) (Koshland et al., 1966).

1.1.2.4.1 Monod, Wyman and Changeux (MWC) model

MWC model postulated that a cooperative oxygen binding protein can exist in two alternative conformations, indicated as R for "relaxed" and T for "tense". Graphically, these two conformations correspond to the upper and lower asymptotes of the Hill-plot for a cooperative protein (**Chapter 1.1.2.3**). Furthermore, the model replaced the Hill's assumption of the simultaneous binding of all the oxygen molecules with the hypothesis of concerted conformational changes among all the subunits of the oligomer. This means that if a subunit was in R-state or T-state, all the others would be in the same conformational state. In absence of ligand, it was assumed the establishment of an equilibrium between the two states R_0 and T_0, defined by the allosteric constant $L_0=[T_0]/[R_0]$. Finally the model assumed that the two conformations are characterized by different dissociation constants K_R and K_T, with an higher oxygen binding affinity for the R-state compared to the T-state. According to the "concerted postulate", the K_R and K_T are the same for all the subunits in each of

the two states, independently by their ligand occupancy. Cooperativity is due to the progressive shift of the T-R equilibrium in favour of the R-state as a function of ligand saturation (**Fig. 1.3**).

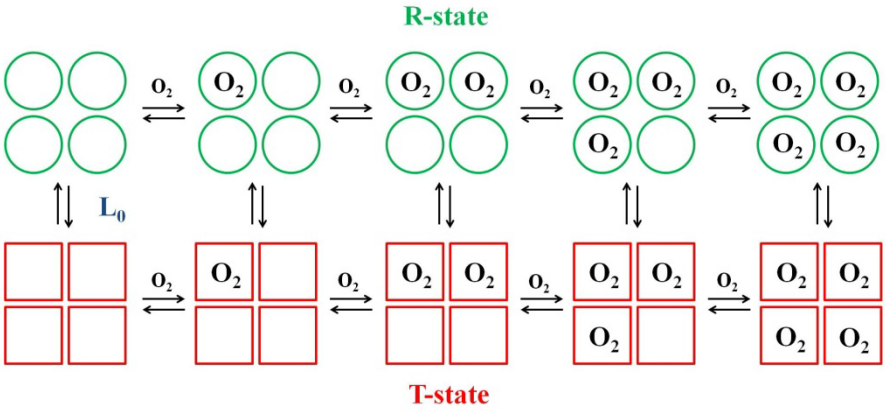

FIGURE 1.3. Schematic view of the MWC model. A protein with four active sites is used as example.

The whole cooperativity process can be defined by the analytical expression (Zhou et al., 1989):

$$Y = nK_R\, pO_2 \frac{(1 + K_R pO_2)^{n-1} + Lc(1 + cK_R pO_2)^{n-1}}{(1 + K_R pO_2)^n + L(1 + cK_R pO_2)^n}$$

Equation 1.6

where

$$c = {}^{K_T}\!/_{K_R} \qquad L_0 = {}^{[T_0]}\!/_{[R_0]}$$

1.1.2.4.2 Koshland, Nemethy and Filmer (KNF) model

Contrary to the MWC model, the KNF model postulates that in absence of ligand the protein occurs in a single conformation, and that the cooperative oxygen binding is mediated by tertiary conformational changes of the single subunits. Indeed each subunit can exist in two different conformations, one with low oxygen affinity and one with high oxygen affinity (**Fig. 1.4**). The model assumes that the binding of an oxygen molecule to the active site of a subunit in the low affinity state induces a conformational change of the neighbor subunit, resulting in a increase of its oxygen affinity. So cooperativity can be described as conformational changes of the single subunits, mediated by allosteric "signals" transmitted between neighboring subunits.

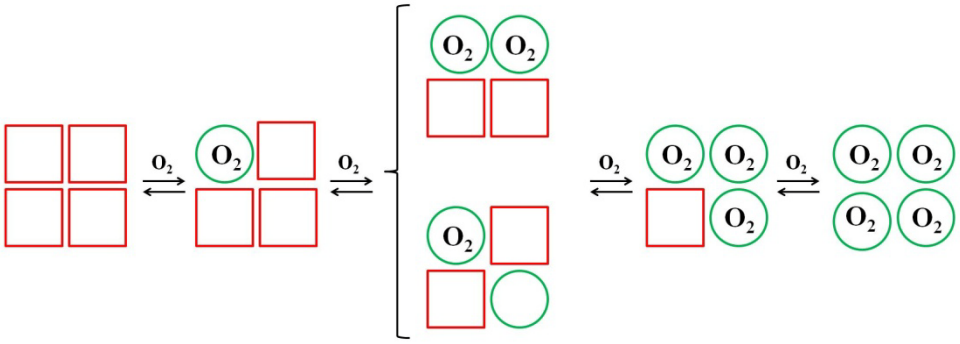

FIGURE 1.4. Schematic view of the KNF model. High affinity conformation is denoted by circles, while low affinity one by squares. The four subunits are represented in a square geometry to clarify the permissible subunit interactions and do not necessary correspond the arrangement of the subunits in three dimensional space (Koshland et al., 1966).

1.1.2.5 Hemoglobin: the paradigm of allostery

Hemoglobin is considered the paradigm of allosteric proteins (Cui & Karplus, 2007; Eaton et al., 2007), and both the previously described MWC and Pauling-KFN models have been applied to phenologically characterize the cooperative oxygen binding of this macromolecule. In particular, as described in the review of Eaton et al. (1999), the model of MWC provides a very accurate description of the cooperative oxygen binding behavior, even if in a somewhat elaborated form.

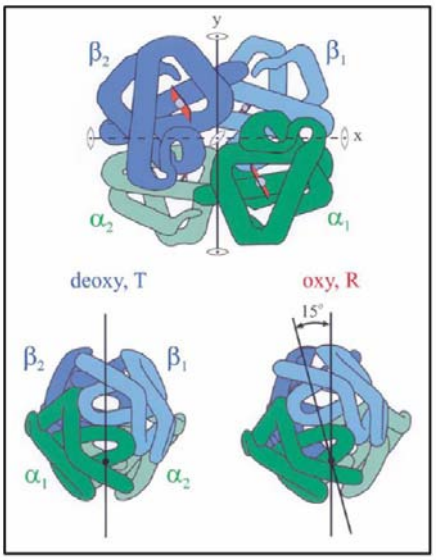

FIGURE 1.5. Schematic structure of hemoglobin fully deoxygenated (T-state) and oxygenated (R-state) (Image from Dickerson & Geis, 1983)

According to the MWC model, X-ray structures of fully oxygenated and fully deoxygenated hemoglobin confirmed the presence of two distinct quaternary structures of the tetramer, widely accepted to represent the structure of R-state and T-state (Perutz et al., 1970). The two structures differ in the arrangement of the αβ dimers, that are rotated by 15° in the R-state compared to the T-state (**Fig. 1.5**). Furthermore, the oxygen-binding curves performed for pure T and R states crystals confirmed that oxygen binding occurs in a non-cooperative way in absence of quaternary

transition (Mozzarelli et al., 1991;); the functional symmetry within each quaternary state, a fundamental postulate of the model, was also confirmed through the encapsulation of hemoglobin into a sol-gel matrix (**Chapter 1.3**), overcoming the major criticism of a non-cooperative binding due to crystal lattice constraints (Shibayama & Saigo, 1995).

However, even if the MWC-model accurately describes the homotropic effects in hemoglobin, it does not take into account for the contribution of heterotropic ligands that can modulate the tertiary structure and function within the T or R quaternary structure (Bruno et al., 2001; Safo et al., 2011). An explanation of the heterotropic effects has been described by the "tertiary two-state" (TTS) model (Henry et al., 2002), that preserves the essential MWC idea of a non-cooperative oxygen binding in absence of quaternary changes, but assumes that the primary role in the cooperative process is due to tertiary conformational changes of the single subunits rather than quaternary changes. More in detail, high *r* and low *t* affinity conformations of individual subunits exist in equilibrium within each quaternary structure, and this conformational equilibrium $t \leftrightarrow r$ is strongly influenced by the quaternary structure of the macromolecule, that favor the *t* conformation if the whole hemoglobin is in the T state or the *r* one if it is in the R state. So the changes of the oxygen affinities upon binding of heterotropic effectors, within a single quaternary state, can be described by the shift of the equilibrium $t \leftrightarrow r$. The identification of two distinct affinity conformations of the T-state entrapped into sol-gel matrix is consistent with this model (Shybayama & Saigo, 2001).

1.1.2.6 A more complicated case of cooperativity: hemocyanin

Although hemoglobin is usually taken as paradigmatic example of allostery, it does not represent the most complicated case of a cooperative protein. Indeed, the comparison between the number of active sites and the complexity of the quaternary structures of hemoglobins and hemocyanins, points to a much more complicated oxygen binding behavior in the case of the latter proteins (**Fig. 1.6**). In particular, due to the large number of active sites and the complex quaternary structure, mostly extension of the classic two-state MWC model are used to describe the oxygen binding behavior of hemocyanin. Only some hexameric

hemocyanins exhibit an oxygen binding behavior which is in agreement with the simplest MWC model (Sanna et al., 2004). Among various extensions of the classic two state model, the three-state MWC model (Minton et al., 1974; Johnson et al., 1988; Richey et. al, 1985) and the nested model (Decker et al., 1988; Decker & Sterner, 1990) seem to describe better the hemocyanins cooperativity process. A schematic view of the two models is reported in **Fig. 1.7**.

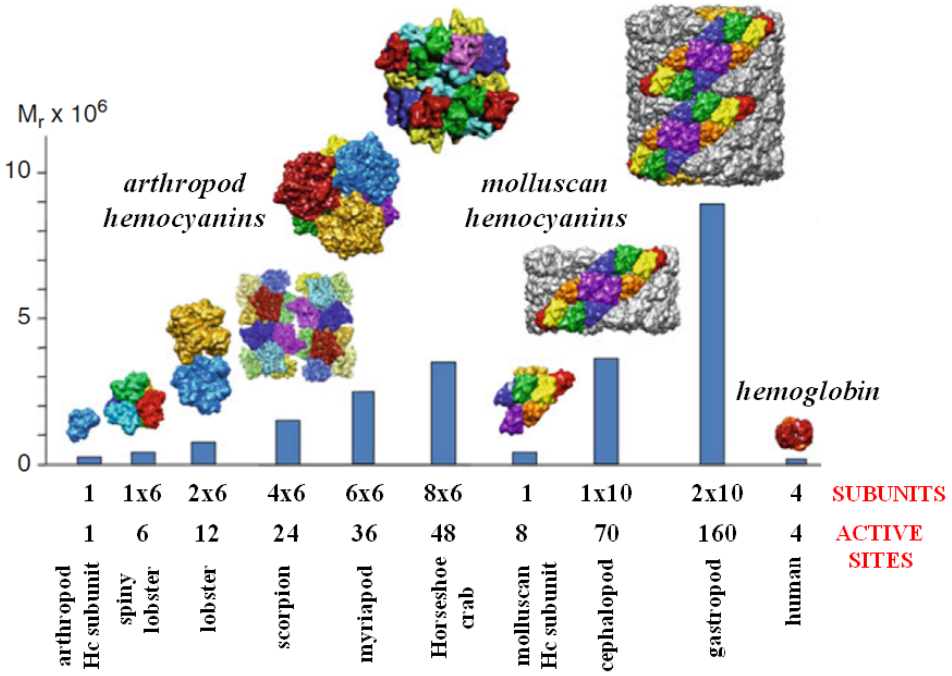

FIGURE 1.6. Comparison of the main features of arthropod and molluscan hemocyanins and human hemoglobin (modified from Decker and van Holde, 2011)

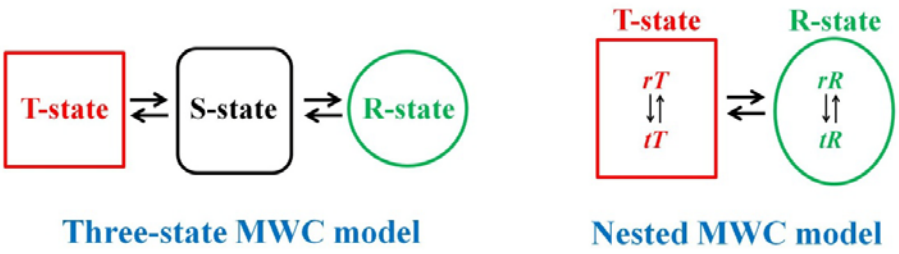

FIGURE 1.7. Schematic view of the two extensions of the classic two-states model of MWC: the three state model and the nested model. The three-state MWC model postulates the presence of a third conformational state, called S-state, between the T- and the R-states. The nesting model instead assumes the presence of two distinct levels of allosteric units: the bigger allosteric units can adopt two conformations, T or R, while the smaller allosteric units are incorporated within the bigger ones and exists in two pairs of conformations, tR and rR or tT and rT, depending on the conformation of the bigger allosteric unit.

In the three-state model, the oxygen binding process is described by the presence of three distinct conformers (T-, R- and S-state), each one characterized by its own oxygen binding constant (K_T, K_S and K_R). The two allosteric equilibrium constants L_T and L_S define the ratio of the unliganded conformers ([T_0], [S_0], [R_0]). The binding polynomial which describes the oxygen equilibrium is written as:

$$P = (1 + K_R\, pO_2)^n + L_T(1 + K_T\, pO_2)^n + L_S(1 + K_S\, pO_2)^n$$

Equation 1.7

where

$$L_T = {[T_0]}/{[R_0]} \qquad L_S = {[S_0]}/{[R_0]}$$

As extension of the classical MWC model, also the nested model proposes that two overall quaternary states, R and T, are involved in the oxygen binding process. However, in this case there are two substates nested within both the R-state (tR and rR) and the T state (tT and rT). Taking into account the presence of two levels of allosteric units (*n* and *m*), the following binding polynomial describes the oxygen binding:

$$P = \left\{(1 + K_{rR}\, pO_2)^{\,n} + l_R(1 + K_{rR}\, pO_2)^{\,n}\right\}^m + \Lambda\left\{(1 + K_{rT}\, pO_2)^{\,n} + l_T(1 + K_{tT}\, pO_2)^{\,n}\right\}^m$$

Equation 1.8

where

$$l_T = {[tT_0]}/{[rT_0]} \qquad l_R = {[tR_0]}/{[rR_0]}$$

$$L = {[T_0]}/{[R_0]} \qquad \Lambda = L\frac{(1 + l_R)^m}{(1 + l_T)^m}$$

Despite these models provide a convincing phenomenological description of the hemocyanins functional properties (Robert et al., 1987; Dainese et al., 1998;

Hellmann et al., 2010), actually thorough structural studies confirming either the presence of three different conformations or the involvement of different types of allosteric units, are still lacking.

1.2 Arthropod hemocyanins

1.2.1 Background

Hemocyanins are the respiratory pigments freely dissolved in the hemolymph of arthropods and molluscs. In arthropods are found as single hexamers (1x6mers) or multiple of hexamers (2x6mers, 4x6mers, 6x6mers, 8x6mers) (**Fig. 1.6**), with a hierarchical organization of the whole structure. The specific aggregation state is species-specific (Decker et al., 2007) and it is stabilized by the presence of divalent cations.

The different oligohexameric level is responsible for the different complexity of the cooperative process observed in species characterized by different aggregational states. Indeed, more complex structures are generally correlated to higher level of cooperativity, with Hill coefficients *n* up to 11, the highest observed for any biomolecule (Erker et al., 2005).

In the following chapter an overview of the main functional and structural properties of arthropod hemocyanin is presented.

1.2.2 Active site

1.2.2.1 X-ray crystallographic investigations

The oxygen binding site of arthropod hemocyanin is common to the type-3 copper proteins (Yoon et la., 2009), in which two copper atoms are coordinated by three histidines. Due to the correlation between oxygen reactivity and active site structure, several studies have been focused on the investigation of the Cu-Cu distance and coordination geometry of the active site (Baldwin et al., 1992; Solomon et al., 1994). Despite these studies, the only detailed information derived from three X-ray crystallographic investigations of the subunit II of the horse shoe crab *Limulus polyphemus* (Magnus et al., 1991; Hazes et al., 1993) and the hexamer of the spiny lobster *Panulirus interruptus* (Volbeda et al., 1989). Prior to analyze the structures, it is important to consider the different solution conditions

from which the proteins were crystallized. Both oxygenated and deoxygenated *L. polyphemus* crystals were obtained in a comparable pH range, 6.2 and 6.5-7 respectively. Deoxy *P. interruptus* crystals instead grown at 4.8. In **Fig. 1.8**, the structure of the oxygenated active site of subunit II of *L. polyphemus* is reported. This is the only example of oxygenated structure actually available.

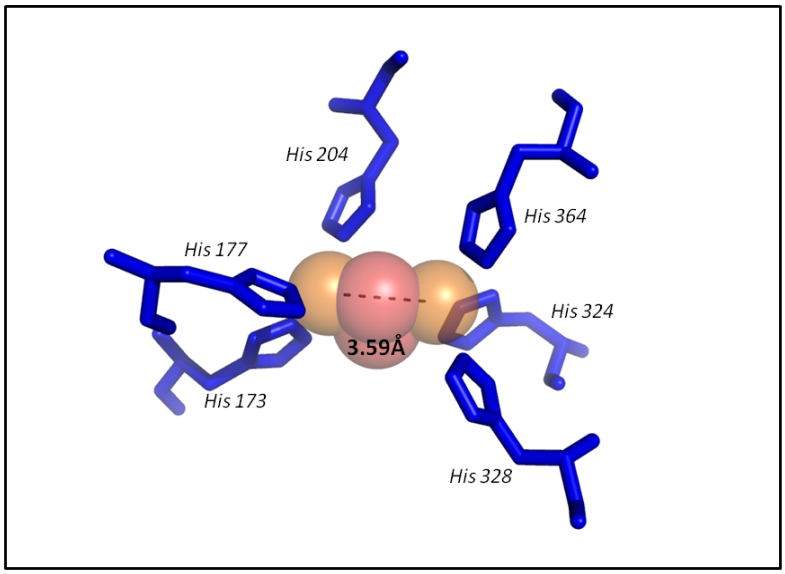

FIGURE 1.8. View of the oxygenated active site of *L. polyphemus* hemocyanin (1OXY.pdb). The two copper atoms (*orange*), coordinated by three histidines (*blues*) each one, bind the oxygen molecule indicated in red. *Pymol* software was used to illustrate the structure.

Binding of oxygen occurs via a reversible two-electrons transfer from the pair of Cu(I) ions in the active site of deoxy hemocyanin. The resulting complex is described as $Cu(II)O_2^{2-}Cu(II)$ complex, with peroxide bound as bridging ligand. Each Cu(II) is coordinated by three histidine in a square pyramidal geometry, in which two histidyl imidazole nitrogens and the oxygen molecule define the equatorial plane, while the third histidyl nitrogen is axially coordinated to copper. The Cu-Cu distance is 3.59Å.

The active site of *L. polyphemus* hemocyanin has been structurally characterized also in the deoxy form. In this case it is not the only structure available, and we can compare it with the active site of *P.interruptus* deoxy hemocyanin. As shown in **Fig. 1.9**, both the active sites are characterized by two Cu(I) coordinated by nitrogen of the three histidine imidazole residues, but superimposing the two structures differences in the coordination geometry of the histidines and in the

metal-metal distances are evidenced (**Fig. 1.9A**). In *P. interruptus* active site, two of the three histidines and a copper atom define a plane from which the third histidine is perpendicularly located, defining a pseudotetrahedral geometry (**Fig. 1.9B**). A trigonal planar coordination geometry instead has been characterized for *L. polyphemus* in the deoxygenated form (**Fig. 1.9C**); in this case the three histidines and the copper atom approximately lie nearly in a plane. The different coordination geometry strongly affect the metal-metal distances of the two active sites, with a distance of 3.16Å for *P. interruptus* and 4.61Å for *L. polyphemus*.

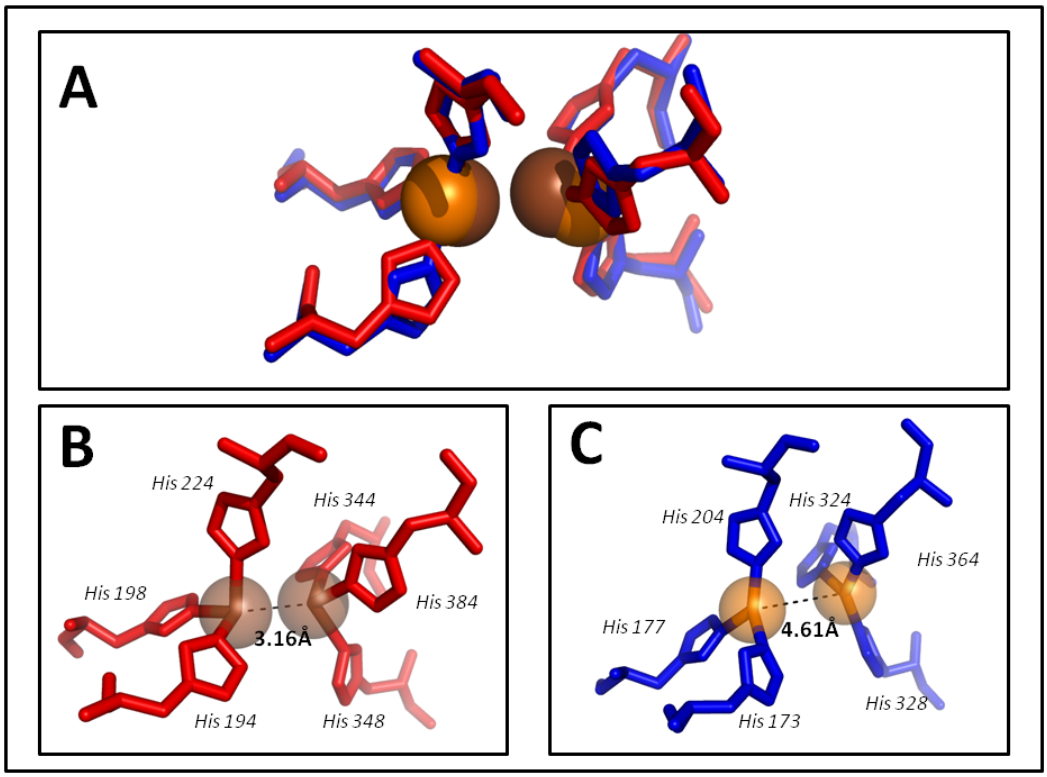

FIGURE 1.9. View of the deoxygenated active sites of *L. polyphemus* (1LLA.pdb) and *P. interruptus* (1HCY.pdb) hemocyanins. In red and blue are indicated the histidines. In brown and orange the copper atoms. **Panel A:** comparison between the coordination geometry of the active site of the two hemocyanins. **Panel B:** *P. interruprus* active site. **Panel C:** *L. polyphemus* active site. *Pymol* software was used to illustrate the structures.

1.2.2.2 X-ray absorption spectroscopy (XAS) investigations

A complementary approach to characterize the geometry of the Hc active site is represented by X-ray absorption spectroscopy (XAS). Due to the lack of color and paramagnetism of cuprous ions, that make deoxy Hc transparent to the

majority of spectroscopic techniques, XAS has emerged as a powerful way to study the local environment of the Cu(I) centers. In **Fig. 1.10** (*left*) the X-ray absorption spectra of *P. interruptus* hemocyanin, in the oxygenated (**a**) and in the deoxygenated form (**b**) are shown. The difference spectrum obtained by the subtraction of the oxy spectrum to the deoxy spectrum evidenced two main peaks, at ~8982eV and ~8985eV, that have been assigned to the 1s → $4p_z$ and 1s→(s+p)* transitions of Cu(I), respectively (Smith et al., 1985).

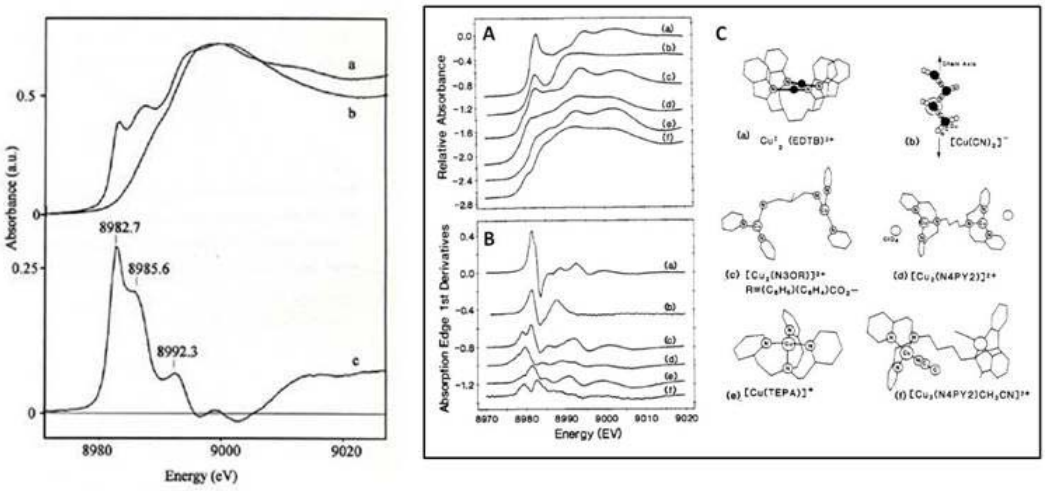

FIGURE 1.10. Left: K-edge absorption spectra of oxygenated (**a**) and deoxygenated (**b**) hemocyanin of *P. interruptus* (**c**) indicates the difference spectrum between oxy and deoxy spectra (Hirota et al., 1998). **Right:** X-ray absorption spectra (**A**) and first derivatives (**B**) of the complexes represented in panel (**C**) (Blackburn et al., 1989).

These intensities are correlated with the coordination geometry of Cu(I) (Brown et al., 1980; Metz et al., 2001). In particular, Blackburn (Blackburn et al., 1989) demonstrated that the intensity of the ~8982eV peak is correlated to the mean displacement of Cu(I) from the plane defined by N_3; the amplitude of the peak decreases as the structure change from trigonal-pyramidal to pseudotetrahedral (**Fig. 1.10; right**).

1.2.3 Quaternary structure of Arthropod hemocyanin

1.2.3.1 Subunits

Arthropod hemocyanins are hexamers (1x6mers) or oligohexamers (*n*x6mers) made up of 75KDa subunits. The subunits comprise three distinct

domains (**Fig. 1.11**), each one with a specific functional role. Domain I (**Fig. 1.11;** *green***)** is mainly α-helical with one β-strand at its C-terminal end. Domain II (**Fig. 1.11;** *red*), rich in α-helical, is packed in between the first and the third domains and contains the active site. This domain is also structurally important because it dominates the intersubunit contacts within the examer. Domain III (**Fig. 1.11;** *grey*) has a seven-stranded β–barrel topology, and it seems to play an important role in the stability of the monomer structure.

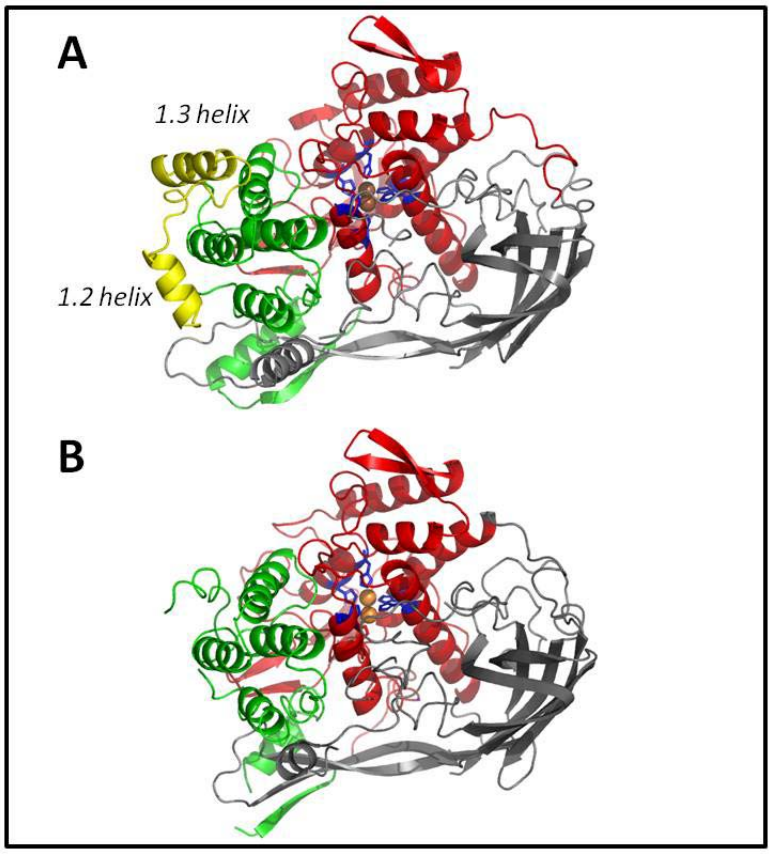

FIGURE 1.11. Arthropod hemocyanin subunit structure of subunit a of *P. interruptus* (1HYC.pdb) (**A**) and subunit II of *L. polyphemus* (**B**). **Domain I**: in *green*. **Domain II**: in *red*. **Domain III**: in *grey*. In yellow are indicated the helix 1.2 and 1.3 absent in subunit II of *L. polyphemus*. *Pymol* software was used to illustrate the structures.

Despite the same architecture of the three domains, the comparison between the X-ray structures of the subunits of *P. interruptus* and *L. polyphemus* evidenced some differences, especially in domain I. Two helixes in domain I (helix 1.2 and 1.3) observed in *P. interruptus* are absent in subunit II of *L.polyphemus*, due to the deletion of 21 residues in the cheliceratan Hc sequence when compared to the

crustacean Hcs sequences. Another difference is the orientation of domain I, which is rotated by 7.5° with respect to the second domain in *L. polyphemus*. Magnus et al. (1994) postulated this rotation plays an important role in cooperativity and regulation of oxygen affinity in all arthropod hemocyanins (See also **Fig. 1.19**). However this structural difference could be an artifact due to the different pH at which the crystals were obtained.

1.2.3.2 1x6-meric hemocyanin: the "building block" of arthropod hemocyanins

For a number of crustaceans, like spiny lobster and many isopods (Sanna et al., 2004; Markl, 1986), hemocyanin consists of only one hexamer, which represents the basic building block of all higher-ordered arthropod hemocyanins. Actually, its structure is the only quaternary structure of arthropod hemocyanin known at crystallographic resolution, that was solved for the hemocyanin of *P. interruptus* (Volbeda et al., 1989). The 3.2Å resolution crystal structure is shown in **Fig. 1.12.** The six subunits, indicated with different colours, are arranged to form two layers of trimers with a threefold symmetry axis, rotated of 60° one respect to the other (Herskovits, 1988) (**Fig. 1.12A**). Each subunit is strongly connected to a subunit of the other layer along a two-fold symmetry axis (**Fig. 1.12B**), allowing to describe the hexamer like a trimer of dimers rather than a dimer of trimers (Gaykema et al., 1986).

The structure shown in **Fig. 1.12** was obtained by the *in vitro* reassembly of equal quantities of subunits *a* and *b*, while native *P. interruptus* hemocyanin contains three different subunit types (Neuteboom et al., 1992). Even if this structure wasn't obtained from the native molecule, it can be considered representative of all the 1x6-meric hemmocyanins. Indeed, the 1x6-mer cryo-EM structure of the European spiny lobster *Palinurus elephans* (Meissner et al., 2003), with an high sequence identity (> 80%) with *P. interruptus*, and the quaternary structure of the homoexamer of subunit II from *L. polyphemus* hemcyanin (Magnus et al., 1991), show a close structural correlation with the structure previously described.

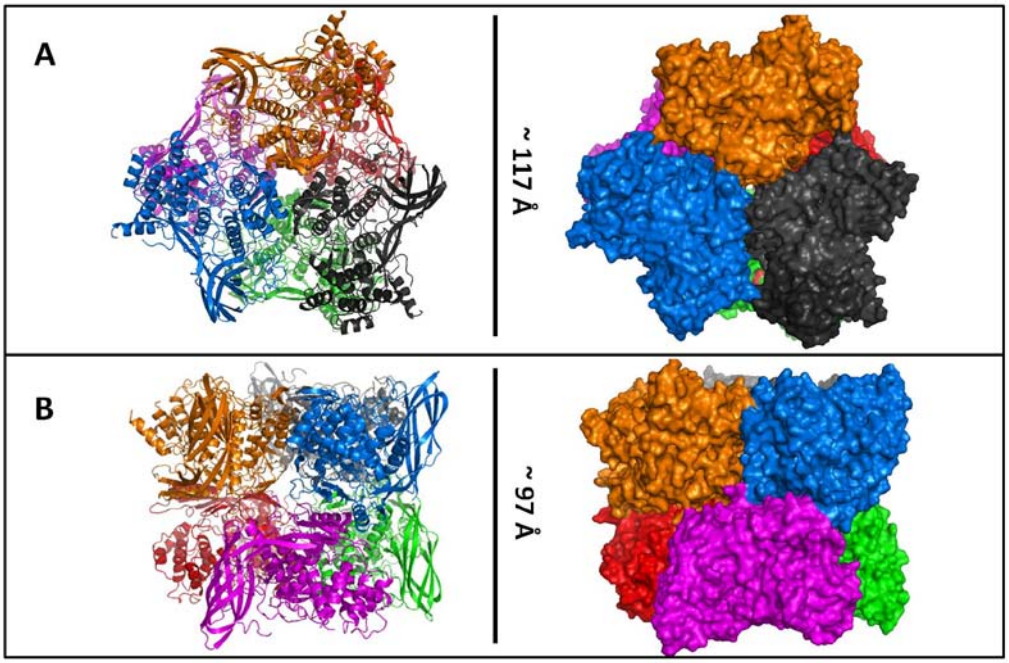

FIGURE 1.12: 1x6-meric hemocyanin of *P. interruptus* (1HYC.pdb). The single subunits are indicated with different colours. **A:** ring view. **B:** lateral view. *Pymol* software was used to illustrate the structures.

1.2.3.3 Investigations of the *n*x6-mer structure of hemocyanin: small-angle X-ray scattering (SAXS)

From the aggregation of *n* examers, more complexes quaternary structures can be observed: the 2x6-meric hemocyanins, typical of most Reptantia, notably Astacura and Brachyura, the 4x6-meric hemocyanins, common among the Arachnida, the 6x6-meric hemocyanin, detected in the centipede *Scutigera coleoptrata* (Kusche et al., 2003), and the 8x6-meric Hc of *L. polyphemus*, which represents the largest arthropod hemocyanin known (Martin et al., 2007).

The absence of more complex quaternary structures than the 1x6-meric solved at crystallographic resolution has stimulated other approaches for the investigation of the structure of *n*x6-mer hemocyanins, such as cryoelectron microscopy (cryo-EM) and small-angle X-ray scattering (SAXS). These techniques allow to solve hemocyanin multimer structure with a resolution as good as ~7Å in case of cryo-EM and 20-30Å in case of SAXS.

In particular, SAXS technique was used to characterize the quaternary structures of three different arthropod hemocyanins, the portunid crab *Carcinus aestuarii*, the stomatopod *Squilla mantis* and the thalassinid shrimp *Upogebia pusilla*

(Micetic et al., 2010). The first two hemocyanins are 2x6-meric while the third one is 4x6-meric. In **Fig. 1.13**, the structural parameters and geometries of SAXS best-fit models are reported. The first evidence of the three structures is the different arrangement of the hexamers in the molecules. In the dodecameric hemocyanin of *C. aestuarii* (**Fig. 1.13A**) the hexameric building blocks are in contact through their short sides, typical of crustacean and cheliceratan 2x6-metric structures, with the threefold axes of the two stacked hexamers are almost perpendicular to each other. On the contrary, the inter-exameric subunit arrangement of *S. mantis* hemocyanin shows the two examers stacked on their long sides, shifted of 66Å and rotated by 5° along their threefold axis (**Fig. 1.13B**). Analog structures were observed in the half molecules of cheliceratan 4x6-meric hemocyanins (Cong et al., 2009) (**Fig. 1.13D**). Also the 4x6-meric structure of *U. pusilla* hemocyanin is unusual, with its symmetrical, tetrahedral subunits arrangement (**Fig. 1.13C**).

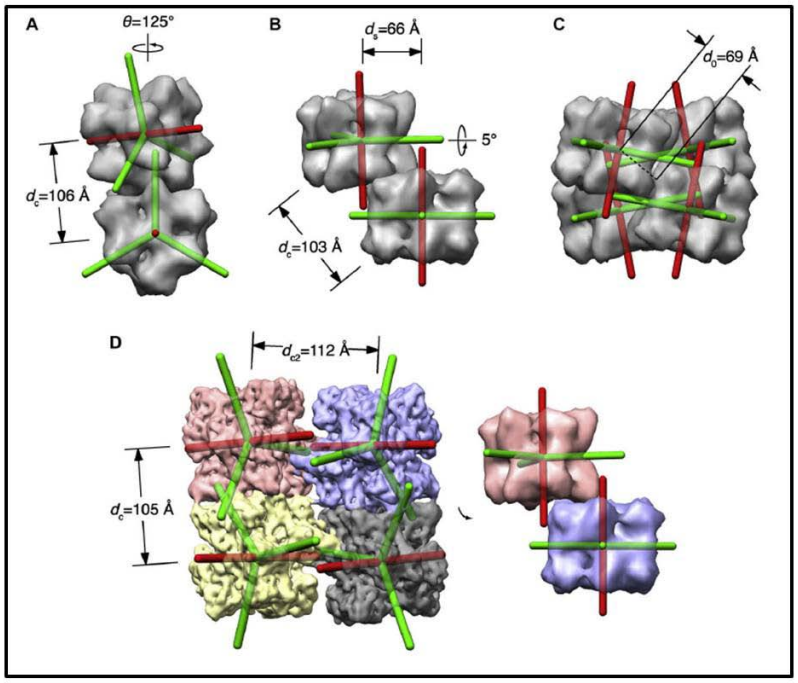

FIGURE 1.13. SAXS best-fit models of the *C. aestuarii* (2x6-meric)**(A)**, *S. mantis* (2x6-meric) **(B)** and *U. pusilla* (4x6-meric)(**C**) Hcs. Panel (**D**) shows the cryo-EM structure of the 4x6-meric *Pandinus imperator* hemocyanin (Micetic et al., 2010).

SAXS technique was also used to detect conformational changes of the 4x6-meric hemocyanin of the tarantula *Eurypelma californicum* (Hartmann & Decker.,

2002), demonstrating the suitability of this technique to investigate the conformations of very large proteins.

Recently, more complex quaternary structures have been solved through cryo-EM: the 6x6-meric hemocyanin of the Myriapoda *Scutigera* (Markl et al., 2009) and the 8x6-meric hemocyanin of *L. polyphemus* (Martin et al., 2007).

1.2.4 Modulation of oxygen affinity: heterotropic effectors

Oxygen binding properties of hemocyanins are finely regulated by the binding of several heterotropic effectors, such as divalent cations and organic ions (Bridges, 2001), that markedly modify its oxygen affinity and cooperativity (Morris et al., 1990). These inorganic and organic allosteric effectors can act either in a positive or negative way, increasing or decreasing the oxygen affinity. A quantification of these effects is given by the expression $\Delta \log p50 / \Delta \log[\text{effector}]$.

Although these allosteric modulators have been widely characterized, only few structural explanations of the mechanisms at which these molecule acts are available. Two of the most investigated effectors are represented by H^+ and L-lactate.

1.2.4.1 Bohr effect

Among the inorganic heterotropic effectors, H^+ play a key role in the modulation of respiratory physiology of arthropods, since hemocyanins are very sensitive to pH changes that can occur in response to both environmental and metabolic factors. Typically, the increase of H^+ concentration in the hemolymph, with a consequently acidification of the medium, causes a decrease of the hemocyanin oxygen affinity. The magnitude of this effect, called Bohr effect, strongly depends by the physiological pH range of the organism, and it has been estimated to be large in decapods crustaceans compared to hemoglobins (Truchot, 1992). A particular case is represented by the reverse Bohr effect observed in *L. polyphemus* hemocyanin, in which the oxygen affinity is increased at lower pH. Recently, the molecular basis of the Bohr effect have been investigated through flash photolysis and X-ray absorption spectroscopy by Hirota et al. (2008); the authors suggested that the changes of the oxygen affinity at different pH are

correlated with structural alterations of the coordination geometry of the active site in the deoxygenated form (**Fig. 1.14**). Furthermore, pH-dependent changes of the R/T equilibrium are also expected.

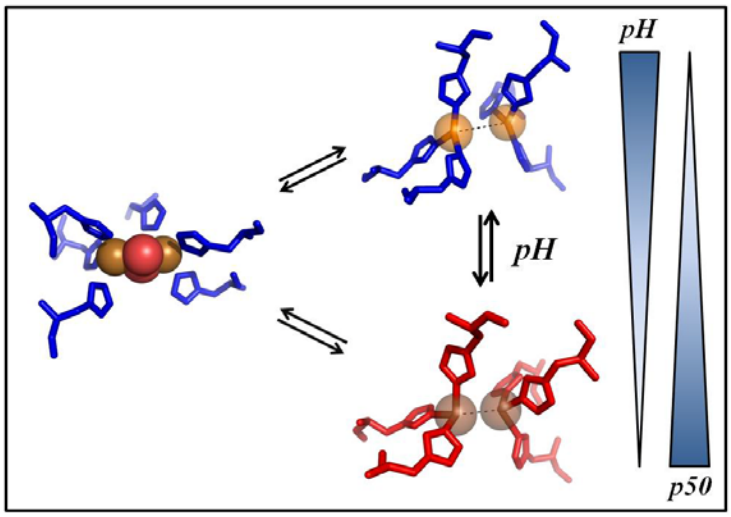

FIGURE 1.14. Schematic representation of the Bohr effect on the coordination geometry of the active site. The geometry of copper in the deoxygenated form changes from pseudotetrahedral at low pH (high p50) towards trigonal planar geometry at alkaline pH (low p50). In oxygenated hemocyanin the geometry of the active site remains unchanged. The active sites here reported are referred to the crystallographic structures of *L. polyphemus* and *P. interruptus* hemocyanin. *Pymol* software was used to illustrate the structures.

1.2.4.2 Lactate

Lactate is the end product of anaerobic metabolism and its concentration in the hemolymph increases under environmental hypoxia or during heavy muscular exercise (Wachter et al., 1997).

The allosteric effect of L-lactate on hemocyanin was discovered for the first time by Truchot (1980), that identified a decrease of the p50 in the hemocyanin of *Carcinus maenas* and *Cancer pagurus.* Although some decapods exhibit low or no sensitivity to L-lactate (Taylor et al., 2000; Sanna et al., 2004), this modulation of the oxygen properties is widely diffused in crustacean (Mangum, 1983b) and represents an important enantiostatic regulation of hemocyanin function. Indeed the lactate-induced increase in oxygen affinity counteracts the Bohr effect caused by the acidification of hemolymph (Booth et al., 1982).

In terms of cooperativity, the binding of lactate causes a decrease of the cooperativity index; in *Cancers magister* this effect is low (Graham et al., 1983), while in *Callinectes sapidus* this variation of the cooperativity is more evident (Johnson et al., 1984).

Contrary to the allosteric effect produced by H^+, L-lactate does not affect the structure of the active site either in the oxygenated or deoxygenated state (Hirota et al., 2010). The increase of the oxygen affinity observed in presence of lactate seems to be governed by a shift of the allosteric equilibrium toward the high affinity R-state (Weber et al., 2008) and a rearrangement of the quaternary structure. The latter interpretation is supported by the SAXS data of the dodecameric hemocyanins of *Homarus americanus* and *Carcinus aestuarii* (Hartmann et al., 2001; Hirota et al., 2010), in which the binding of L-lactate modifies the interhaxameric distances.

The quaternary structural effect of L-lactate on the oxygen affinity of hamocyanin could be explained by the gating mechanism proposed by Hazes et al. (1993), later elaborated by Magnus et al. (1994). In this model, the highly conserved Phe 49 is suggested to play a key role in the allosteric mechanism, acting as the trapdoor for the entrance of oxygen to the actives site (**Fig. 1.15).**

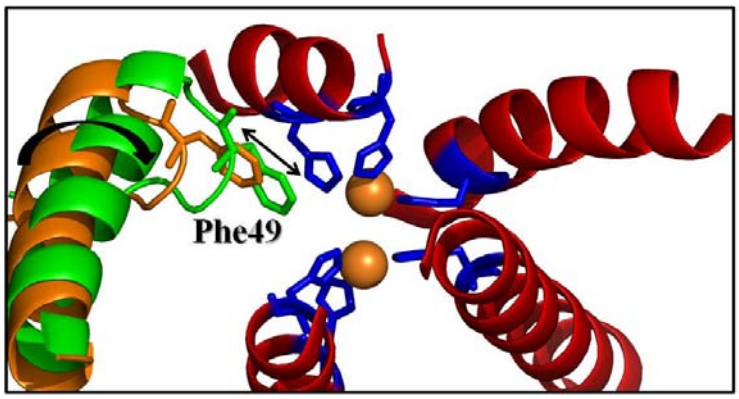

FIGURE 1.15. Structural mechanism of oxygen affinity regulation. The movement of Phe 49, associated with the rotation of domain 1 of 7.5°, affects the oxygen entrance to the actve site. A movement of Phe 49 away from the dinuclear copper ("open door") (*in orange*) increases the oxygen binding affinity. On the contrary, a reduced affinity of the "closed" conformation arises from a closer position of Phe 49 to the active site (*in green*). In orange and green are represented the domain 1 of *P. interruptus* hemocyanin and L. polyphemus, respectively. For clarity, only the active site of *L. polyphemus* hemocyanin is reported. *Pymol* software was used to illustrate the structures.

1.2.5 Spectroscopic signals diagnostic for oxygen binding

1.2.5.1 UV-visible spectra

The absorption spectra of hemocyanin exibits three characteristics bands, at 280 nm, 337 nm and 560 nm, as represented in **Fig. 1.15.**

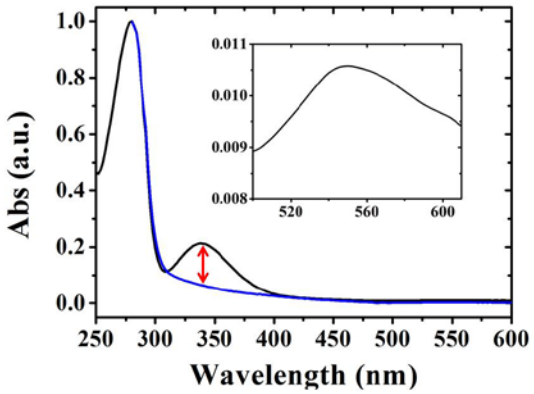

FIGURE 1.15. Absorption spectra of arthropod hemocyanin in the oxygenated (in *black*) and deoxygenated (in *blue*) form. **INSET:** band at 560 nm.

The absorption maxima at 280 is mainly caused by the absorbance of the two aromatic amino acids tryptophan (Trp) and tyrosine (Tyr), and its intensity is proportionally correlated to the protein concentration, according to the Beer's law. Instead, the other two bands are linked to the oxygenation degree of hemocyanin. While the $Cu(I)_2$ form does not exhibit spectroscopic features above 300 nm, the binding of oxygen gives rise to a strong charge transfer (CT) band at 337 nm, and a much weaker band CT band at 560 nm, assigned to $\pi\sigma^* \rightarrow Cu(II)$ and $\pi v^* \rightarrow Cu(II)$ charge transfer (CT) transitions, respectively (Solomon et al., 1994). Thus the intensity of the absorption signal at these two wavelengths represents a direct measure of the oxygen concentration.

1.2.5.2 Fluorescence emission properties

The binding of oxygen to the active site, responsible for the appearance of the absorption bands at 338 and 560 nm, also affects the fluorescense emission properties of hemocyanins. Indeed, the intrinsic tryptophan fluorescence of deoxygeanted hemocyanin (when excited in the near UV) is quenched upon the binding of oxygen molecules (**Fig. 1.16**). This quenching has been descibed as the fluorescence resonance energy transer (FRET) between the tryptophans and the active site in the oxygenated form (Shaklay et al., 1970), and it represents an other useful spectroscopic signal in the investigation of the oxygen binding properties of hemocyanin (Erker et al, 2004).

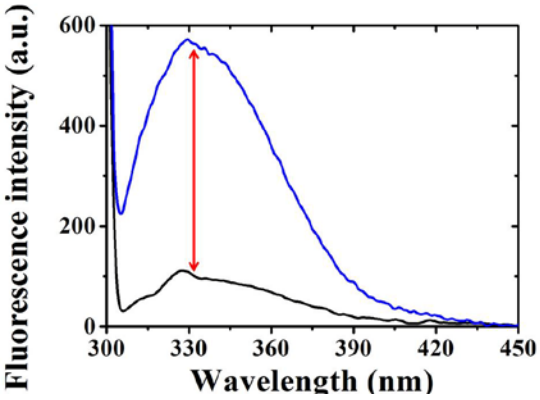

FIGURE 1.16. Fluorescence emission spectra of hemocyanin in oxygenated (in *black*) and deoxygenated (in *blue*) form. **Excitation wavelength:** 295 nm.

Fluorescence measurements also allow to elucidate structural aspects of hemocyanins, in particular some conformational features about the active site and the intersubunit contact areas (Ricchelli et al., 1980, 1984, 1987). Acrylamide fluorescence quenching experiments have revealed that the intrinsic fluorescence contribution of *P. interruptus* hemocyanin is due to three different classes of tryptophan residues: one class of residue exposed to the solvent, the second one of residues in the hydrophobic environment but accessible to the solvent and the last one of residues deeply buried and not accessible to the solvent (Ricchelli et al., 1980). In particular the residues Trp-197,-204,-222 and -248 (**Fig. 1.17; in red**), distributed in close proximity to the active site, are preserved also in hemocyanins of other arthropods, including the subunit *SS2* of *C. aestuarii*. The X-ray structure of *C. aestuarii* hemocyanin is not available but a closely similar distribution of Trp has been suggested (Di Muro et al., 2002)

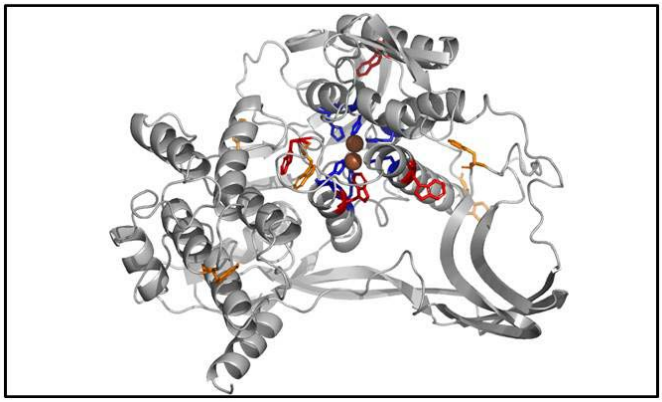

FIGURE 1.17. X-ray structure of subunit a of *P. interruptus*. In orange are indicated the Trp residues. In *red* the Trp residues conserved in arthropod hemocyanins. In *blue* the His. In *brown* the copper atoms. Model based on the atomic coordinates of Volbeda et al. (1989).

1.2.5.3 Near-UV circular dichroism (CD) spectra

The conformational reorientations of the tryptophan residues in the proximity of the copper sites, due to the binding of various ligand molecules, have been investigated through the changes observed in the aromatic region of the near-UV CD spectra of hemocyanin (Beltramini et al., 1992). Indeed the arrangement of the aromatic residues affects the features of the CD curve in the aromatic region, corresponding to the region between 240 and 300 nm. Representatives CD spectra of arthropod hemocyanin in oxygenated (in *black*) and deoxygenated (in *blue*) form are shown in **Fig. 1.18**, which can mainly distinguished by the presence of a broad negative CD band near 340 nm in the oxygenated form.

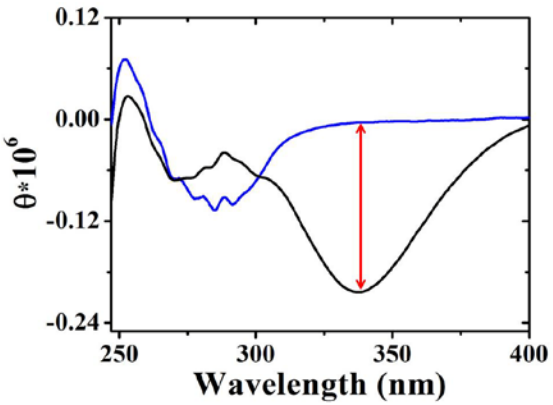

FIGURE 1.18. Near-UV CD spectra of arthropod hemocyanin in the oxygenated (in *black*) and deoxygenated (in *blue*) form.

1.3 Investigation of allosteric proteins: sol-gel matrix

1.3.1 Sol-gel technology

In the last years sol-gel matrix has attracted much attention as ideal material for immobilization of macromolecules within its porous optically transparent matrix, due to its inherent versatility and the simple sol-gel processing conditions. The encapsulation of proteins is based on the physical entrapment of molecules within the pores of the silica matrix, preserving their structures and functionality (Ellerby et al., 1992; Avnir et al., 1994). Furthermore, it has been demonstrated that sol-gel matrix are thermally and photochemically stable and protects encapsulated proteins from self-aggregation and microbial attack (Gupta & Chaudury, 2002). Because of the porous nature of the sol–gel network (diameter pores of ~2-100Å), small ions or molecules can diffuse through the matrix to the site of entrapped proteins (Flora & Brennan, 2001a), producing a detectable signal (using an appropriate sensing scheme). This feature has represented the key point for the development of biosensors based on sol-gel

matrix; optical and electrochemical biosensors for several compounds, such as nitrite (Silveira et al., 2010), organophosphate pesticides (Oujji et al. 2012), lactate (Gomes et al., 2007) and glucose (Chang et al., 2010) have been developed.

Sol-gel technique also represents a useful tool for structural and functional characterization of allosteric proteins, through the ability of the matrix to limit conformational change. Indeed, as reported for hemoglobin (Khan et al., 2000; Samuni et al., 2006; Lepeshkevich et al, 2009), the silica matrix slow down or eliminates the tertiary and quaternary relaxation of the protein, without affecting equilibrium properties of ligand and effector binding. The entrapment of different conformational states have been described also for the large 24-meric *E. californicum* hemocyanin (Ronda et al., 2007).

Mechanical forces and specific electrostatic interactions between the entrapped proteins and the silica walls are implicated to reduce the large-scale dynamics of the entrapped biomolecules (Shibayama & Saigo, 1995; Gilliland et al., 2005).

1.3.2 Sol-gel process

Silica sol-gel process involves hydrolysis and polycondensation reactions of a silicon alkoxide precursor $Si(OR)_4$, such as tetramethyl-orthosilicate (TMOS) ($R=CH_3$) or tetraethyl-orthosilicate (TEOS) ($R=C_2H_5$), with the formation of a colloidal suspension that gelified forming the silica matrix (Hench & West, 1990).

Hydrolysis occurs when the alkoxide precursor is mixed with water (**Eq. 1.9**), with the formation of silanon groups Si-OH and the release of the corresponding alcohol ROH. Due to the slow hydrolysis of alcoxysilanes, the reaction requires either an acid or base catalyst.

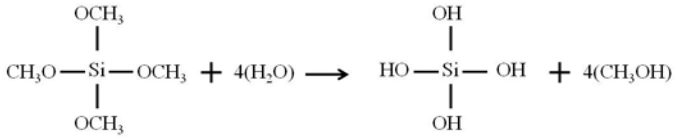

$$TMOS + 4(H_2O) \longrightarrow Si(OH)_4 + 4(CH_3OH)$$

Equation 1.9

During the condensation, the silanol groups (Si-OH) interact forming ≡Si-Si≡ bonds:

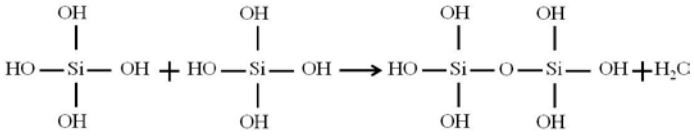

Equation 1.10

Further polycondensation of silanols and siloxanes (**Eq. 1.11**) results in the formation of silica colloidal particles with 2-20 nm diameter (Sakay-Kato & Ishikura, 2009) and a more or less densely crosslinked internal structure. The biomolecule of interest is usually incorporated into the matrix at this step of the sol-gel matrix synthesis.

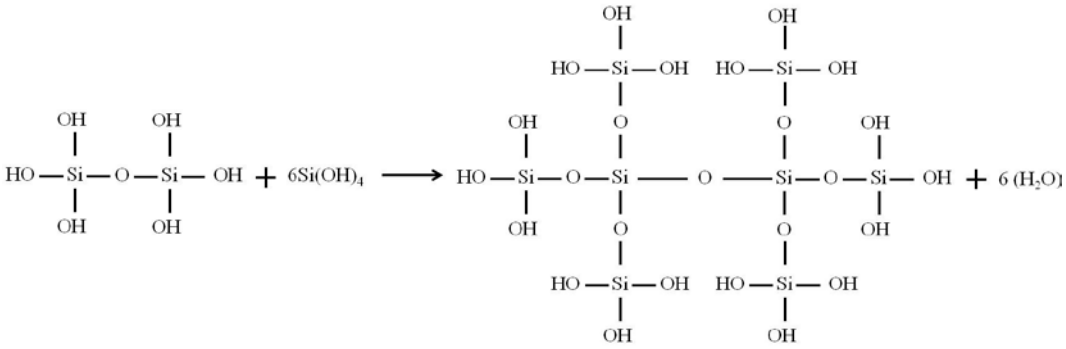

Equation 1.11

With time these colloidal particles interact one each other, with the formation of a three dimensional network with pores of submicrometer dimensions. After gelification, the gel must be maintained completely immersed in liquid for a period of time ranging from hours to days. This step is known as aging and includes the changes that take place after the gel point, resulting in an increase of the strength of the matrix and a decrease of the pore size (Kraus et al., 1993). The chemical changes that occur during aging can be categorized as further hydrolysis and condensation reactions: syneresis (expulsion of solvent with shrinkage of the matrix) and coarsening. Coarsening is due to selective dissolution and reprecipitation of the gel network, resulting in an increase of the thickness of the interparticles necks and a decrease of the porosity (Scherer, 1998).

At the time of gelation, the matrix may be considered as a system consisting of two-phases: a porous solid phase and a trapped aqueous phase. This hydrogel can be dried with the removal of the liquid from the pores of the network; depending on the drying condition, silica matrix with different properties can be obtained (**Fig. 1.19**).

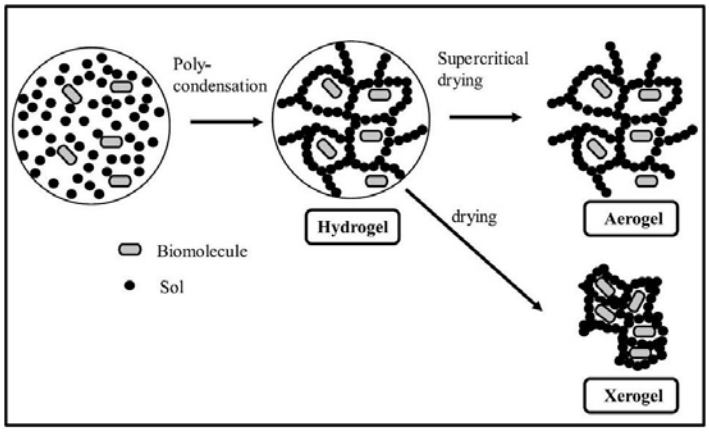

FIGURE 1.19. Schematic representation of the sol-gel synthesis. After the polycondensation process the drying of the hydrogel at supercritical conditions (high temperature and pressure) yeld to aerogel, while xerogel refers to gel dried at temperature close to room temperature and under atmospheric pressure. In the latter case, the elimination of the solvent from the pores is due to the capillary force exerted by the hydrophilic Si-OH side groups of the wet gel. This process causes the shrinkage of the pores (Sakay-Kato & Ishikura, 2009).

1.3.3 Factors affecting the structural properties of the sol-gel matrix

The microstructure of sol-gel matrix is defined by the size of the colloidal particles and the extent of their cross-linking prior to gelation, that are greatly dependent on the rates of hydrolysis and condensation reactions (Gupta & Chaudhury, 2007). These rates are controlled by various factors, such as pH, solvent/water content and temperature. Clearly, precise control of polymerization conditions is fundamental for protein encapsulation since, if not controlled, can influence the native protein conformation and its activity.

As previously described, hydrolysis and polycondensation reactions can be catalyzed under acidic and basic conditions. Under acid-catalyzed conditions the hydrolysis kinetic is favored instead of the condensation and mostly linear structures are obtained, while at higher pH condensation is faster than hydrolysis, resulting in larger and more ramified polymers (McDonagh et al., 1996; Klempere et al., 1988). In terms of pores size, this inverse relationship between the rates of the hydrolysis and condensation reactions tend to yield dense microporous

networks (pores diameter <2nm) at low pH, whereas alkaline conditions favor particulate mesoporous gels (2nm<pores diameter <50nm) (Coradin et al., 2006).
The branching degree of oxo-silanic network also depends on the R ratio $H_2O/Si(OR)_4$. Indeed, as indicated in **Eq. 1.9**, the amount of water strongly influences the hydrolysis and, consequently, the condensation kinetics. The increase of the R ratio favors the formation of more hydrolyzed species (Uhlhorn et al., 1992), resulting in more branched structures after the condensation (Schmidt et al., 1984).
Furthermore, the influence of the temperature on the silica matrix properties was defined as another fundamental parameter to consider during sol-gel synthesis (Cerveau et al., 1999). The porosity of the gels, that is the main textural parameter affected by temperature, can be tuned at low temperature (<3°C) to obtain mainly microporous matrix or mesoporous one at higher temperature (>20C°).

1.3.4 Bioencapsulation

To achieve the entrapment of an active biomolecules into the sol-gel matrix, it is important to provide a suitable environment for the encapsulated protein, in order to reduce the risks of protein denaturation or lost of activity. To this aim, the use of a buffer solution to raise the adverse pH of the post-hydrolysis mixture to physiological range represents an important procedure to avoid protein denaturation (Ellerby et al., 1992).
A disadvantage of sol-gel matrix is the generation of alcohol as by-product of the hydrolysis reaction (**Eq. 1.9**), which in large quantities can be detrimental for the biomolecules. To overcome this problem, several additives have been used to increase the stability of the encapsulated biomolecules, including the osmolytes N-methylglycine and sorbitol (Brennan et al., 2003), polyethylene glycol (PEG) (Gill & Ballesteros,1998) and glycerol (Khan et al., 2000; Fuentes et al., 2004). New biocompatible silane precursors, like sodium silicate (Bathia & Brinker, 2000) and diglyceryl silane (DGS) (Besanger et al., 2003), have been also used to completely avoids generation of alcohol.

1.4 Aim of the project

Several phenomenological descriptions of the functional properties of hemocyanins have been performed according to the allosteric models illustrated in **Chapter 1.1.2.6,** but the structural characterization of any possible conformer is still lacking.

This work is focused on the definition of a structural model of cooperativity for the crab *Carcinus aestuarii* hemocyanin, attemptiong also a functional and structural characterization of the different conformers. We have decided to investigate the 12-meric hemocyanin of this species because its oxygen binding behavior, as a function of both pH and L-lactate concentration, has been widely investigated (Dainese et al., 1998; Hirota et al., 2008; Hirota et al., 2010; Weber et al., 2008). Structural information are also available (Micetic et al., 2010).

To this aim, hemocyanin has been entrapped into silica sol-gel matrix to avoid the allosteric transition between the different conformers. According to the simplest MWC-model, we expect the entrapment of hemocyanin in an high oxygen affinity R-state and a low oxygen affinity T-state. Thus, embedding deoxy-hemocyanin in sol-gel will allow to study the oxygen equilibrium of the low-affinity conformer whereas embedding oxy-hemocyanin will yield the oxygen equilibrium with the high-affinity. Hill analysis of the oxygen binding curves of hemocyanin embedded into the matrix, in presence and absence of oxygen, may describe the R- and T-asymptote of the sigmoidal curve of hemocyanin in solution (**Fig. 1.20**).

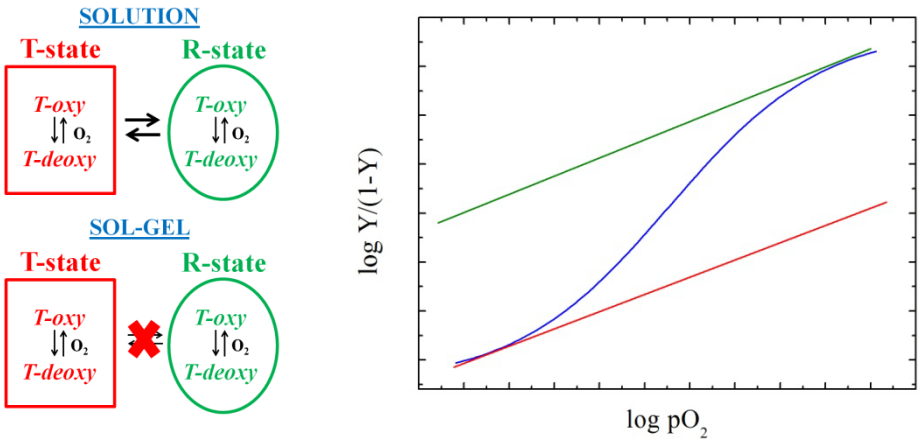

FIGURE 1.20. Representative Hill-plot of the protein in solution (in *blue*) and embedded into the silica matrix in presence (R-state; in *green*) and absence of oxygen (T-state; in *red*).

Moreover, we will verify if our experimental data are in agreement with the MWC model or if extensions of the same one are required to described the overall oxygen binding equilibrium. A further level of investigation will be the determination of the quaternary structure and the coordination geometry of the active site of the different conformers both in the oxy- and deoxygenated state. To date, this information is missing because all structural data available in literature on hemocyanin in solution refer to the R or T conformer in the case of the oxygenated or deoxygenated form (**Fig. 1.20**).

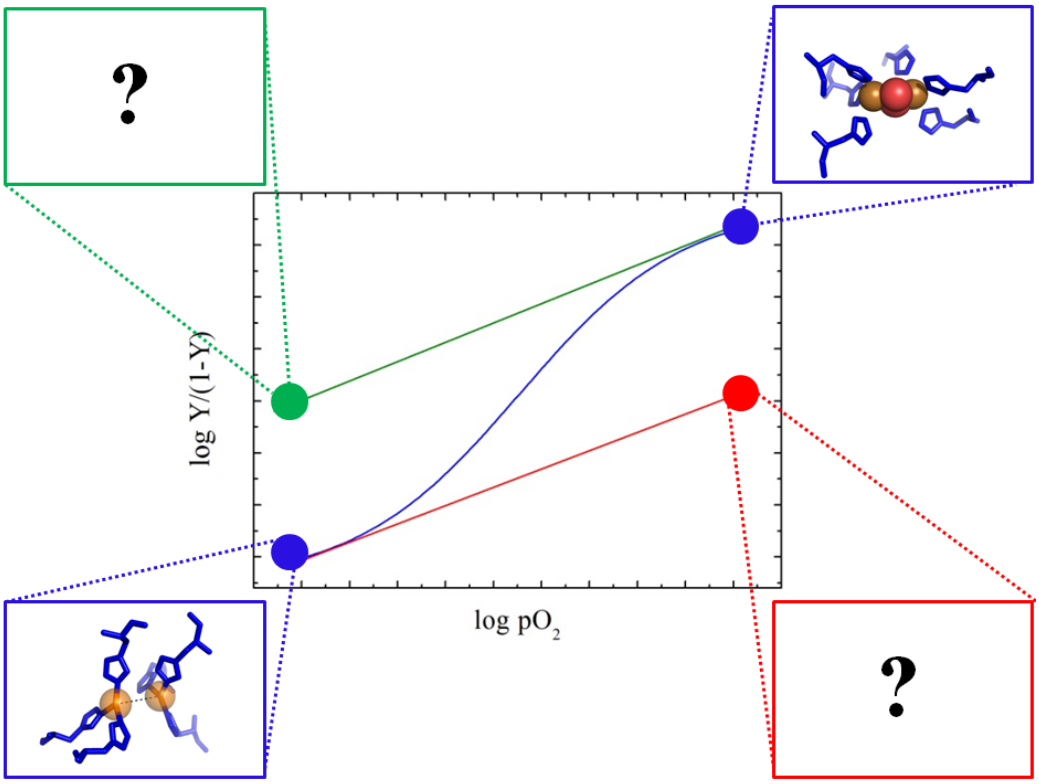

FIGURE 1.20. Coordination geometry of the oxygenated (*top right*) and deoxygenated (*bottom left*) hemocyanin in solution. Structural information about the T-conformer oxygenated (*bottom right*) and the R-conformer deoxygenated (*top left*) are still unknown.

The functional and structural effects of the allosteric effectors H^+ and lactate will be also characterized at the levels of distinct protein conformers.

2. Materials and methods:

2.1 Protein purification:

Hemocyanin was purified from the hemolymph of the crab *Carcinus aestuarii*. The hemolymph was collected by inserting a syringe needle through the dorsal lacunae of living animals, filtered through a gauze and mixed with a 5% (v/v) of protease inhibitor cocktail (P2714 Sigma). Then, hemolymph was dialyzed (membrane cut off: 12000-14000 Da) overnight at 4°C against a buffered solution containing 50mM Tris, 20mM $CaCl_2$, pH 7.5 and centrifuged at 54,841 x *g* for 40 min at 4°C, to eliminate cell debris. The supernatant was ultracentrifuged at 222,592 x *g* for 5h at 4°C, with the sedimentation of a dark blue pellet. Finally the pellet was resuspended and stored in 50 mM Tris, 20 mM $CaCl_2$, pH 7.5 with 20% saccharose, at -20°C. Both the centrifugation and ultracentrifugation steps were performed using a *Beckman XL-70* Ultraspeed Centrifuge (rotor *70Ti*). Before the preparation of the samples, hemocyanin was unfreezed and dialyzed overnight with the buffer 50mM Tris, 20mM $CaCl_2$, glycerol 25% at the desired pH (6.5, 7.5 or 7.8). The purified hemocyanin was quantified, according to the Lambert-Beer law, with a diode-array spectrophotometer (*Hewlett Packard HP8452A*) measuring the absorbance at 280nm. The molar extinction coefficient of *Carcinus aesturaii* hemocyanin is $E_{280}^{0.01\%} = 1.24\ mg^{-1} \times ml \times cm^{-1}$. After each purification the absorbance ratio A_{338nm}/A_{280nm} was calculated: in purified oxy-hemocyanin this value is 0.21.

2.2 Design of Teflon cells for spectroscopic experiments

Spectroscopic experiments involving silica sol-gel matrix required the development of suitable cell and sample holders. To this aim we designed and constructed specific Teflon cells with optical windows (**Fig. 2.1, A**). Teflon material was used because of its chemical inertness and excellent dielectric properties. The dimension of the cells are 9 mm (*weight*) x 32 mm (*height*) x 3 mm (*depth*), allowing the inclusion into quartz cuvettes with a standard size of 12.5 mm x 49 mm x 12.5 mm. Internal optical window with a width of 3mm was designed taking account of the beam size of the spectroscopic techniques applied in this work. We also designed a sample holder for X-ray

absorption spectroscopy (XAS). It consists of two blocks of Teflon (a single block is shown in **Fig. 2.1, B**) with an hollow central rectangular area (9 mm x 32mm x 1.5mm). When the two blocks are combined together they define an internal cavity , having the same size and dimension as the Teflon cell (**Fig. 2.1, C**). Therefore the Teflon cell with the polymerized gel perfectly fit into this pocket. The two optical windows of the sample holder can be covered with Kapton films and the optical window space between the internal Teflon cell and the external surface of the sample holder can be filled with buffer, through the two holes at the top of the holder (**Fig. 2.1, C**).

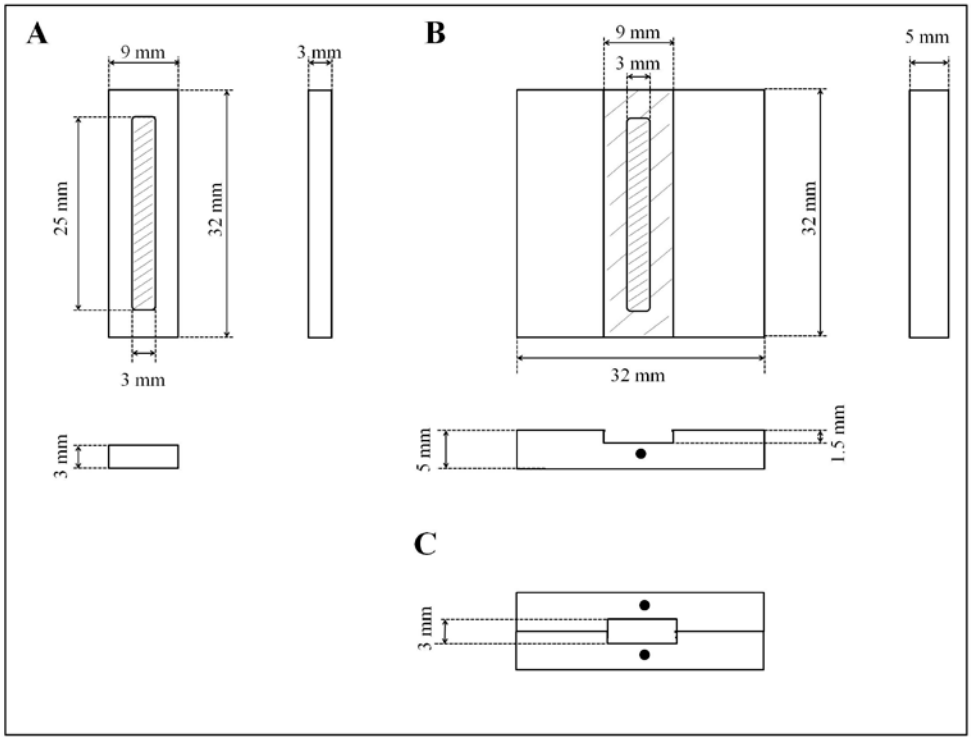

FIGURE 2.1. Details of the Teflon cell and sample holder designed for spectroscopic experiments. Top, front and side views of the Teflon cell (**A**) and "half" sample holder are reported (**B**). Only top view of the "full" sample holder is shown (**C**), with the two holes indicated as black circles.

2.3 Hemocyanin encapsulation

Protein encapsulation in silica gels was carried out following two different protocols. Both protocols are based on the hydrolysis/condensation reactions of the liquid alkoxide precursor tetramethyl orthosilicate (TMOS; 341436 Aldrich). Depending on the spectroscopic technique used, the polycondensation/gelification of the sol-gel matrix was carried out into Teflon cells, quartz capillaries (see **Chapter 2.5.4**) or quartz cuvettes (see **Chapter 2.5.5**). .

One protocol (*protocol A* throughout) is similar to the one described by Shibayama and Saigo (1995), and applied in a modified version by Ronda et al. (2007). A mixture of 200µl of TMOS, 47.2µl of water and 2µl of HCl (10mM) was sonicated for 40 min at low temperature (range 4-10°C). Then, 498.4µl of a solution (50mM Tris, 20mM CaCl2 pH 7.8) containing hemocyanin (~60mg/ml) was added and gently stirred by Vortex.

The second protocol (*protocol B* throughout) is a modified version of the one reported by Khan et al. (2000) and differs from protocol 1 in three aspects: *1)* the catalysis of the initial hydrolysis reaction with an equal volume of buffer and not by adding acid; *2)* the substitution of sonication with a more gentle stirring by Vortex; 3) the presence of 25% of glycerol as additive. These differences have been suggested by the authors (Khan et al., 2000) to lead to different rate of the hydrolysis step. More in detail, a solution containing 125 µl of TMOS and 125 µl of Tris 50 mM, $CaCl_2$ 20 mM, 25% glycerol (v/v) at the desired pH (6.5, 7.5 or 7.8) was gently stirred for 30 seconds. Then, 70 µl of hemocyanin, at the desired concentration, was immediately added.

Independently from the protocol used, after the gelification process, which required from 5 to 15 minutes, sol-gel matrices were covered with buffer and aged at 4°C overnight. The matrices gelified into the Teflon cell, with a thickness of ~2mm, were abundantly rinsed with buffer before use to eliminate the non-encapsulated hemocyanin that could remain adsorbed to their surface.

The encapsulation of deoxygenated hemocyanin involved conversion of oxy-hemocyanin to the deoxy-form under nitrogen atmosphere before encapsulation followed by encapsulation under anaerobic conditions in a glove-box.

2.4 Ligand equilibrium studies of encapsulated hemocyanin

2.4.1 Reaction between cyanide and hemocyanin

The reaction between KCN and hemocyanin was performed both for protein in solution and embedded into the matrix in buffer 50mM Tris, 20mM CaCl2, 25% glycerol, pH 7.8, at 20°C. A quartz cuvette with a lightpath of 1 cm was used. To a 3ml solution containing 5 mg/ml of hemocyanin, an aliquot of a freshly prepared KCN solution was added to yield a final ligand concentration of 5mM. After the addition of KCN, the quartz cuvette was rapidly mixed and the absorbance at 338nm was recorded every 30 seconds for 60 minutes in the spectrophotometer. The experiments were performed three times for each condition (*n*=3). An exponential equation $y=y_0+A\cdot e^{R_0\cdot x}$ was used to fit the data, where R_0 represents the rate of the reaction.

2.4.2 Oxygen binding measurements

Oxygen binding curves of *Carcinus aestuarii* hemocyanin, both in solution and embedded into the silica matrix were performed through an home-made gas-mixing system, based on *1)* a gas proportioner meter (P-meter multi-channel meter, *Aalborg*), *2)* oxygen and nitrogen cylinders, *3)* a quartz cuvette and *4)*a spectrophotometer. The gas proportioner meter blends the input fluxes of oxygen and nitrogen, and send the gas mixture to the quartz cuvette, which is placed into a thermostatted cuvette holder of the spectrophotometer. Prior to enter into the cuvette, the gas mixture was brought to water saturation. All the components are linked through gas-impermeable tubes and needles. A schematic picture of the apparatus used during oxygen binding measurements is shown in **Fig. 2.2**.

The oxygen content of the output gas redirected to the cuvette is strongly dependent on the flow tubes assembled in the gas proportioner meter. Indeed each one is characterized by specific maximum and minimum flux value. To obtain an adequate range of oxygen content, the optimal solution was the use of a 042-07-GL tube for oxygen and a 012-10-SA for nitrogen. The calibration data are reported in **Table 2.1.** The highest pO_2 value that can be obtained with these flow tubes is 144.01torr (5.60 ml/min of O_2 and 21.6ml/min of N_2), while the lowest is

3.20torr (0.60 ml/min of O_2 and 104 ml/min of N_2). Lower pO_2 are potentially possible by increasing the N_2 flux, but we have shown that fluxes higher than 104 ml/min are too strong for a quartz-cuvette measuring system.

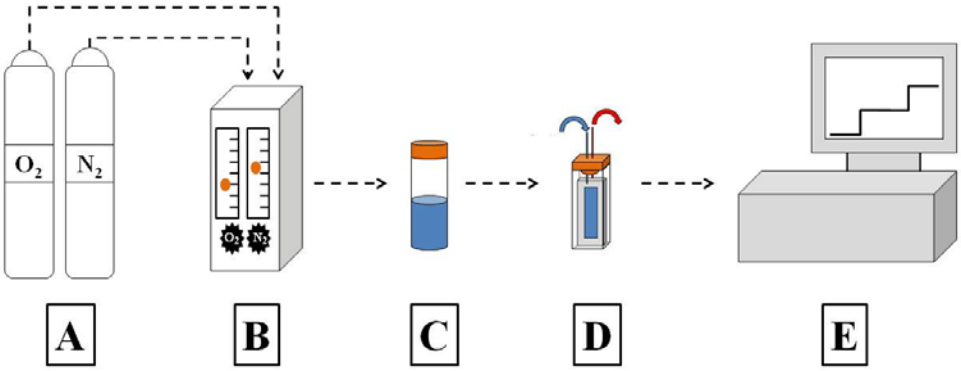

FIGURE 2.2. Home-made gas-mixing system. **A:** oxygen and nitrogen cylinders; **B:** gas proportioner meter; **C:** *humidifier chamber;* **D:** quartz cuvette**; E:** spectrophotometer.

Tube number	**042-07-GL**	**012-10-SA**
Scale reading (mm)	**Oxygen flow (ml/min)**	**Nitrogen flow (ml/min)**
65	5.60	312
60	5.05	279
55	4.52	247
50	4.05	216
45	3.60	183
40	3.18	155
35	2.77	128
30	2.40	104
25	2.00	81.5
20	1.68	67.5
15	1.31	45.8
10	0.96	33.2
5	0.60	21.6

TABLE 2.1. Flowmeter calibration data for 042-07-GL and 012-10-SA tubes. Scale reading (mm) at center of float is indicated.

Therefore, changing the fluxes of oxygen and nitrogen we were able to set specific oxygen pressures into the cuvette, with an FS accuracy of +/-5%.

The oxygen binding curves were obtained in 50mM Tris, 20mM $CaCl_2$, 25% glycerol, pH 6.5-7.5-7.8, at 20°C. Also experiments in presence of 40mM L-lactate were performed. The samples were prepared at a hemocyanin concentration of 5 mg/ml, both for protein in solution and embedded into the matrix.

For hemocyanin in solution a quartz cuvette with a volume of 1 ml was used, while for hemocyanin embedded into the sol-gel matrix a larger cuvette of 3 ml is required to permit the insertion of the Teflon cell. As indicated in **Fig. 2.2**, after adding hemocyanin into the cuvette a gas-permeable cap (*in orange*) was used to close the top of the cuvette. In *blue* and *red* are respectively indicated the "gas input needle" and the one required for air-hole.

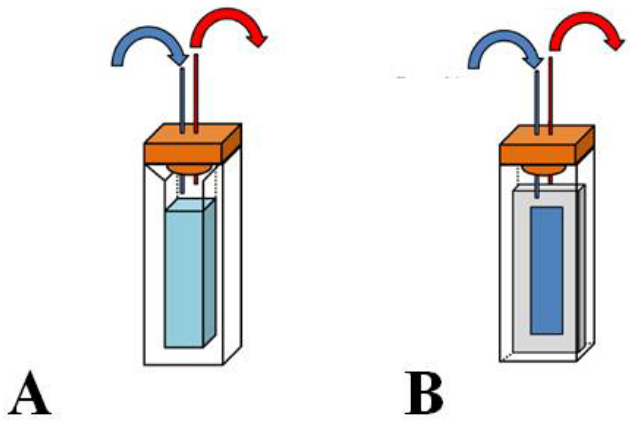

FIGURE 2.2. Quartz cuvettes of 1ml (**A**) and 3 ml (**B**) for oxygen binding measurements of hemocyanin in solution and in sol-gel matrix, respectively. In figure **B** is also represented the inserted Teflon cell with the polymerized silica gel. In orange are represented the gas-permeable caps. The gas mixed by the gas proportioner (*blue arrow*) enter into the cuvette through a needle, here indicated as a thin blue line. The red line represents the needle for air-hole (*red arrow*).

The degree of oxygenation of hemocyanin was followed by measuring through the spectrophotometer the variation of the absorbance at 338nm, corrected for the absorbance at 500nm. All the measurements started from the fully deoxygenated hemocyanin.

For the solution measurements, either the deoxygenation and oxygenation of hemocyanin were carried out by gently shaking the cuvette for some minutes (up

to 15 minutes), until the equilibrium between hemocyanin and the setted pO_2 was reached. Working with protein in solution is important to avoid the direct contact of the gas-input needle to the solution containing hemocyanin, because of the gas bubbling through the buffer leads to protein precipitation.

In sol-gel matrix experiments, the entrapped hemocyanin was flushed with N_2 overnight due to the slow deoxygenation process. Then, progressively higher pO_2 were settled. To determine when hemocyanin was in equilibrium with the oxygen pressure pO_2 into the cuvette, the absorbance signals at 338nm and 500nm were measured in continuous. Only when the $Abs_{338\text{-}500nm}$ signal hitted a plateau, the pO_2 was increased **(Fig. 2.3)**. After every oxygen-binding curve, the Teflon mask was removed from the cuvette and the absorbtion spectrum of the buffer was recorded, to check the possible presence of hemocyanin in solution released from the sol-gel. Concentrations <5% were usually detected.

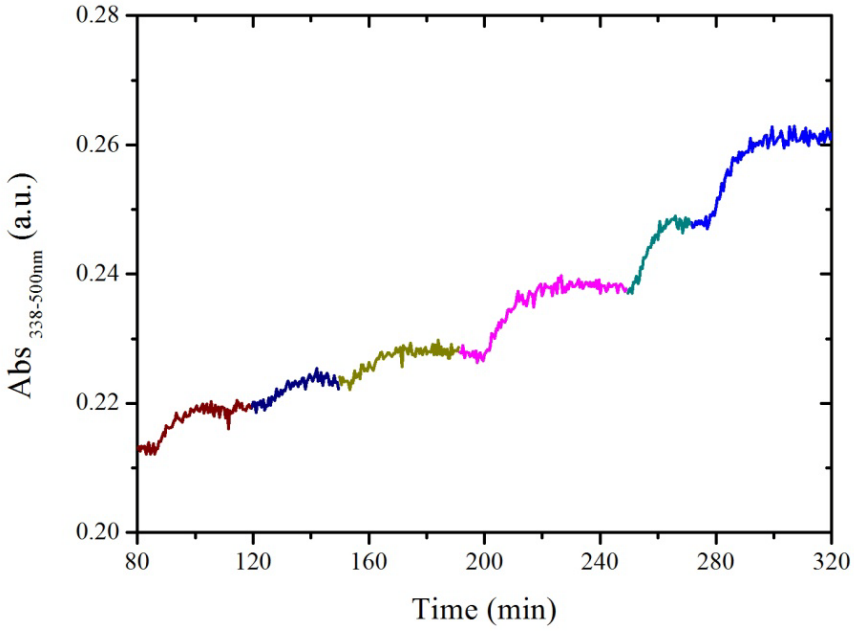

FIGURE 2.3. Absorption signal at 338nm (substracted for the absorbance at 500mn) in function of time at different pO_2 (indicated with different colors).

2.4.3 Data analysis of the oxygen-binding equilibria

From oxygen binding experiments, it is possible to define oxygen binding curves, where the *percent saturation* is plotted against the partial pressure of oxygen pO_2 (torr) (**Fig. 2.4**).

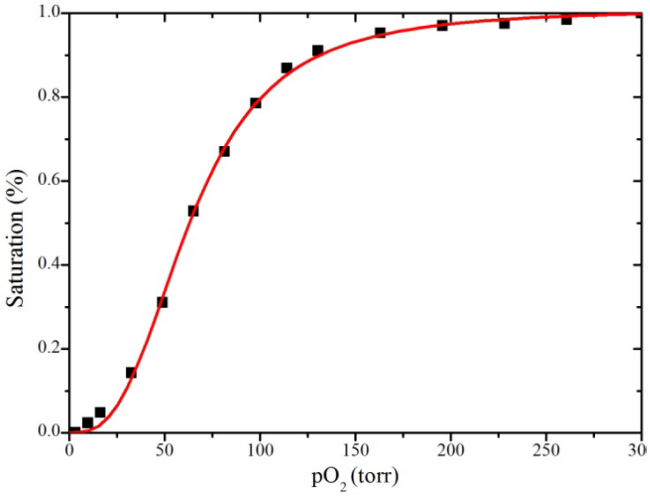

FIGURE 2.4. Representative oxygen binding curve. The black squares correspond to the fractional saturation collected the specific values of pO2. In red, the fit to Hill-equation is shown.

The partial pressure of oxygen pO_2 (torr) was determined according to the flowmeter calibration data reported in **Table 2.1**, while the fractional saturation of hemocyanin Y was calculated from the $Abs_{338\text{-}500nm}$ signal, by applying the following equation (Decker & Sterner, 1990):

$$Y = (A_x - A_0) / (A_\infty - A_0)$$

Equation 2.1

where Y is the fractional saturation, A_x the absorbance value for each pO_2 condition, A_0 the absorbance value of hemocyanin fully deoxygenated and A_∞ for fully oxygenated hemocyanin.

Then, the data were fitted to the Hill-equation (**Fig. 2.4**, in *red*):

$$\frac{Y}{1-Y} = \frac{{pO_2}^n}{p50^n}$$

Equation 2.2

The elaborated oxygen binding-curves were also visually represented using Hill-plots, allowing the determination of the oxygen-binding affinity p_{50} (torr), the cooperativity index *n* both for hemocyanin in solution and embedded into the sol-gel matrix. Hill-plots were obtained by plotting:

$$\log \frac{Y}{1-Y} = n \log pO_2 - n \log p50$$

Equation 2.3

2.4.4 Analysis of oxygen binding data according to the MWC and three-state model.

To calculate the allosteric equilibrium constants of hemocyanin in solution, the oxygen binding curves were fitted in terms of the MWC model (Monod et al., 1965) or of the three-state MWC model (Richey et. al, 1985).

For the MWC model the following binding polynomial was used:

$$P = (1 + K_R\, pO_2)^n + L(1 + K_T\, pO_2)^n$$

Equation 2.4

where

$$c = {}^{K_T}\!/_{K_R} \qquad L = {}^{[T_0]}\!/_{[R_0]}$$

where K_T and K_R are the binding constants of the T- and R-state. $[T_0]$ and $[R_0]$ are the concentrations of unliganded conformers.

The three-state MWC analysis was performed by the following binding polynomial, already used to investigate the oxygen binding behavior of other hemocyanins (Beltramini et al., 2005; Hellmann et al., 2010; Menze et al., 2005):

$$P = (1 + K_R\, pO_2)^n + L_T(1 + K_T\, pO_2)^n + L_S(1 + K_S\, pO_2)^n$$

Equation 2.5

where

$$L_T = {}^{[T_0]}\!/_{[R_0]} \qquad L_S = {}^{[S_0]}\!/_{[R_0]}$$

$[T_0]$, $[S_0]$ and $[R_0]$ are the concentrations of the three conformers without oxygen bound.

Assuming the block of a single conformational state (non-cooperative oxygen binding) at each experimental condition, the equilibrium constants K ($torr^{-1}$) of hemocyanin entrapped into the sol-gel matrix were calculated as $1/p_{50}$.

2.5 Characterization of the hemocyanin conformers

2.5.1 Near-UV Circular Dichroism spectroscopy

Circular dichroism spectra were recorded with a JASCO J-710 dicrograph, in a wavelength range of 240-400 nm (*near-UV*). Samples were prepared in buffer 50mM Tris, 20mM CaCl2, 25% glycerol, pH 7.8 at an hemocyanin concentration of 0.4 mg/ml for protein in solution and 2 mg/ml for sol-gel measurements. The different final concentration is due to the dilution (1:5) of the 2 mm sol-gel matrix in a 10 mm quartz-cells. Each spectrum was obtained as the average of 10 scans to optimize the signal-to-noise ratio and was corrected for background using the buffer solution and the empty matrix. The CD data were represented in terms of molar ellipticity [θ] (deg x cm^2/dmol), using the molecular weight of the monomer (75kDa) (Nickerson et al., 1971). The software *Spectra Manager 1.52.02 (JASCO)* was used to analyzed all CD spectra.

2.5.2 Fluorescence Emission Spectroscopy

The fluorescence emission spectra were recorded with a Perkin Elmer LS 50B spectrofluorimeter equipped with a thermostatic cell holder (T=20°C). The samples were prepared at a low hemocyanin concentration (~0.08 mg/ml) to minimize the inner filter effect (Lakowicz, 1986) and measured in buffer 50mM Tris, 20mM CaCl2, 25% glycerol, pH 7.8. For sol-gel measurements, the Teflon cell was inserted into a fluorescence quartz cuvette, rotated by 45° with respect to the incident light beam and the detector. The samples were excited at 278 nm or 295nm and emission was detected in the range 300-450 nm. Background intensities of the buffer and the empty sol-gel matrix were always subtracted from the samples. All the spectra were normalized by the maximum intensity.

2.5.3 X-ray Absorption Spectroscopy (XAS)

Cu K-edge X-ray absorption spectra of hemocyanin embedded into sol-gels were collected on beamlines BM29 at the ESRF of Grenoble (France), using flat Si(111) crystal monochromator. X-ray edge data were recorded in the energy range 8.8 - 9.528 KeV, with an acquisition time of 5 seconds per scan point. The sol-gel matrices, prepared at pH 7.8 and at a hemocyanin concentration of

5mg/ml, were gelified into Teflon cell and inserted into the sample holder described in **Chapter 2.2.** Then, the optical windows were closed with kapton films and filled with the buffer at pH 7.8. X-ray edge spectra were normalized by fitting a function to pre- and post-edge regions of the spectrum.

2.5.4 Small-Angle X-ray Scattering (SAXS) measurements

SAXS measurements have been performed at room temperature at the Elettra Synchrotron Radiation facility (Trieste, Italy). The wavelength of the incident X-ray beam was 1.54 Å (at E = 8keV) and the explored Q-range extended from 0.019 to 0.46 $Å^{-1}$, where $Q = 4\pi \sin\theta/\lambda$ and 2θ is the scattering angle. The *Mar300 Image Plate* sample-detector distance was set to 1.78 m. Undoped sol-gel samples were measured into quartz capillaries (diameter 1 and 1.5mm, wall thickness 0.01), mounted on an aluminum sample holder with a circular cutout. The recorded 2D scattering patterns (1200x1200 pixels) were converted using the *Fit2D* program. Data reduction, involving flux, exposure time and sample transmission normalization, was performed using in-house programs. SAXS spectra of silica matrix at different experimental conditions (**Table 2.2**) were collected.

Sample	Glycerol (%)	pH	Aging (days)
1	0	6.5	2
2	0	6.5	6
3	0	7.5	2
4	0	7.5	6
5	0	7.8	2
6	0	7.8	6
7	25	6.5	2
8	25	6.5	6
9	25	7.5	2
10	25	7.5	6
11	25	7.8	2
12	25	7.8	6

TABLE 2.2. Experimental conditions of the collected undoped sol-gel matrix spectra.

2.5.4.1 SAXS data analysis

SAXS spectra were analyzed, in collaboration with Prof. Francesco Spinozzi and Dr. Maria Grazie Ortore of the Marche Polytechnic University, using the *Genfit* program, though the application of a mass fractal model defined by Teixeira (1988). This model describes the sol-gel matrix in terms of a porous network formed by the aggregation of spherical silica particles of radius R_0. In particular the ordering of the spherical primary particles within the cluster can be described by the following interparticle structure factor S(Q):

$$S(Q) = 1 + \frac{\sin[(d-1)\tan^{-1}(Q\xi)]}{(QR_0)^d} \frac{d\Gamma(d-1)}{[1+1/(Q^2\xi^2)]^{(d-1)/2}}$$

Equation 2.4

where $Q = 4\pi \sin\theta/\lambda$, d is the fractal dimension, R_0 is the radius of the spherical particle and ξ is the cutoff distance of the fractal correlation, which can be interpreted as the pore size in the gels (Lelong et al., 2007).

2.5.5 Small-Angle Neutron Scattering (SANS) measurements

For SANS measurements, sol-gels with and without entrapped hemocyanin (5mg/ml) were prepared at pH 7.8 in H_20 (**Chapter 2.3**) and polymerized into 1- and 2-mm pathlength quartz cuvettes with two open ends (**Fig. 2.5**). The cuvettes were obtained by cutting both the ends of 45mm cuvettes with a diamond saw and then divided in two parts with a central cut. Once the gel is formed inside, the cuvettes were incubated in *rinse solutions* containing different amount of D_20 and H_20 for 24h to ensure a correct hydrogen–deuterium exchange. The *rinse solutions* at the selected degrees of deuteration (X_D) were prepared diluting a *mother solution* at pH 7.4 with glycerol and different amount of D_20/ H_20. A pH of 7.4 was considered taking into account the relationship pD = pH meter reading

Fig. 2.5. Image of the quartz cuvette with two open ends.

+ 0.4 for samples prepared in D_20 (Srere et al., 1961). In **Table 2.3** and **Table 2.4** are reported the composition of the *mother solution* and the *rinser solutions*.

Concentration (Unit)	H_2O*	D_2O	Tris	HCl (37%)	$CaCl_2$	Na-Lactate **
M	0.540	53.874	0.162	0.157	0.065	0.130
g/l	9.722	1078.962	19.625	5.710	7.192	14.53
w/w	0.009	0.962	0.018	0.005	0.006	0.013
mol/mol	0.010	0.983	0.003	0.003	0.001	0.002
v/v	0.010	0.973	0.010	0.003	0.005	0.008

TABLE 2.3. *Mother solution* composition. * H_2O derived from the 35% w/w HCl.
** Samples were prepared both in presence and absence of sodium lactate.

X_D	V total (µl)	V glycerol pure (µl)	V *mother solution* (µl)	V D_2O pure (µl)	V H_2O pure (µl)
0.60	9000	2487	2989	1582.4	2007.0
0.70	9000	2487	2989	2330.7	1258.7
0.72	9000	2487	2989	2480.4	1109.0
0.80	9000	2487	2989	3079.0	510.4
0.86	9000	2487	2989	3527.9	61.5

TABLE 2.4. *Rinse solutions* composition at different degrees of deuteration (X_D).

Small-Angle Neutron Scattering (SANS) measurements have been carried out at ILL neutron radiation facility (Grenoble, France), on the beamlines D11 and D22. Undoped sol-gel samples were recorded at D11 for scattering vectors $0.009<Q<0.175$ Å^{-1}. Hemocyanin entrapped sol-gel spectra were collected at D22 in the Q-range 0.012-0.2 Å^{-1}. The data reduction was performed using the same in-house programs for SAX analysis.

2.5.5.1 SANS data analysis

The neutron scattering curves of entrapped hemocyanin were analyzed, in collaboration with Prof. Francesco Spinozzi and Dr. Maria Grazie Ortore of the Marche Polytechnic University, by the QUAFIT method (Spinozzi & Beltramini, 2012), using the SAXS resolved structure of *C. aestuarii* hemocyanin to determine the coordinates and the orientation of the single subunits forming the

hexamer (Micetic et al., 2010). Each SANS spectra was analyzed by the program twenty times through a Montecarlo approach, resulting in twenty independent fits. The deviation between the model and the experimental data is defined by the chi-squared χ^2. The fitted parameters are represented by the scaling factor k, the flat background B, which takes into account incoherent scattering effects (Putman et al., 2007; Stuhrmann, 2004), the rotational angles α, β and γ of one hexamer with respect to the other one, the interhexameric distance *d* and the relative mass density of hydration water *p*.

2.6 Statistical analysis

2.6.1 Comparing group means

Before the comparison of the means, the *Levene's test* were performed to assess the equality of variances in the different samples. If the homogeneity of variance assumption was satisfied, the comparison of the means were performed through *t-test* or *one-way ANOVA*, depending on the number of groups compared. In all the other cases, non-parametric tests were used: the test of *Mann-Whitney* for the comparison of two groups and the *ANOVA of Kruskal-Wallis* when the groups were more than two.

The statistical analysis of the results have been performed using the *Statistica* software.

2.6.2 Factorial design

The 2^3 factorial design that we have used to analyzed the structural parameters of the SANS measurements is well described by Box et al., 1978. In this statistical analysis the *main effect* of three factors, here defined as **A**, **B** and **C**, and the effects of their interactions (*two- and three factor interaction effects*) on a defined parameter are investigated. For each factor two levels (version) have been defined: a_1 and a_2 for factor **A**, b_1 and b_2 for factor **B** and c_1 and c_2 for factor **C**. As shown in **Table 2.5**, the two levels are conveniently coded by minus and plus signs.

	+	-

A	a_1	a_2
B	b_1	b_2
C	c_1	c_2

TABLE 2.5. + and – levels of the three factors **A**, **B** and **C**.

Run	A	B	C	$\bar{y}$
1	-	-	-	$\bar{y}_1$
2	-	-	+	$\bar{y}_2$
3	-	+	-	$\bar{y}_3$
4	-	+	+	$\bar{y}_4$
5	+	-	-	$\bar{y}_5$
6	+	-	+	$\bar{y}_6$
7	+	+	-	$\bar{y}_7$
8	+	+	+	$\bar{y}_8$

TABLE 2.6. Design matrix of the 2^3 factorial design

The means of the replicas $\bar{y}_n$ obtained at the experimental conditions defined by the combinations of three + and – signs were used for the data elaboration (**Table 2.6**). For the calculation of the *main effects* of a single factor two approaches can be used. The first one consists in the calculation of the differences between the $\bar{y}_n$ obtained by changing the levels of the investigated factor from – to +, at each condition of the other two factors. In this case the *main effect* is defined as the mean of four differences. An example for the calculation of the *main effect* of **A** is reported in **Table 2.7**.

The second approach is easier than the previous. Indeed the main effect for each of the variables is calculated as the difference between two averages:

$$main\ effect = \bar{y}_+ - \bar{y}_-$$

where $\bar{y}_+$ is the average response for the plus level of the investigated factor and $\bar{y}_-$ for the minus one. Therefore, in this case the *main effect* of factor **A** is obtained as here described:

$$effect \text{ of } \mathbf{A} = \frac{\bar{y}_5 + \bar{y}_6 + \bar{y}_7 + \bar{y}_8}{4} - \frac{\bar{y}_1 + \bar{y}_2 + \bar{y}_3 + \bar{y}_4}{4}$$

	Condition at which the comparison is made	
Individual measures of the effect of changing factor A from - to +	**B**	**C**
$A_1 = \bar{y}_{5-} \bar{y}_1$	-	-
$A_2 = \bar{y}_{6-} \bar{y}_2$	-	+
$A_3 = \bar{y}_{7-} \bar{y}_3$	+	-
$A_4 = \bar{y}_{8-} \bar{y}_4$	+	+
$A\ effect = \frac{A_1 + A_2 + A_2 + A_3}{4}$		

TABLE 2.7. Calculation of the main effect of factor **A** as mean of four differences (A_1, A_2, A_3 and A_4).

A measure of the *two-factor interactions* is supplied by the half of the difference between the mean effects of the first factor calculated at the + and - level of the second factor. Therefore, four of the eight $\bar{y}_n$ are included in one average and half in the other. If we consider the **A** x **B** *interaction*, the measure of the effect will be:

Levels of B	**Average A effect**
+	$A_+ = \frac{A_4 + A_3}{2}$
-	$A_- = \frac{A_1 + A_2}{2}$
	$\boldsymbol{A\ x\ B\ interaction} = \frac{A_+ - A_-}{\mathbf{2}}$

TABLE 2.8. Calculation of the **A** x **B** *interaction effect.*

For the interpretation of the *two-factor interaction effects*, *two-way tables* are usually considered (**Table 2.9**).

+	A_3		A_4
A			
-	A_1		A_2
	-	**B**	+

TABLE 2.9. Two-way table for the interpretation of the **A** x **B** *interaction***.**

The *three-factor interaction effect* is calculated as the half of the difference between the two-factor effects calculated at the + and – sign of the third factor (**Table 2.10**).

Levels of C	**Average *A x B* effect**
+	$A\ x\ B_+ = \frac{A_4 - A_3}{2}$
-	$A\ x\ B_- = \frac{A_1 - A_2}{2}$
$\boldsymbol{A\ x\ B\ x\ C\ interaction} = \frac{\boldsymbol{A\ x\ B_+ - A\ x\ B_-}}{\boldsymbol{2}}$	

TABLE 2.10. Calculation of the *three-factor interaction* effect.

To determine if the *main* and *interaction effects* are statistically significant, the *standard error* of the effects must be calculated. If $\bar{y}_n$ are the means of the n_i replicas collected at the different experimental conditions, it is possible to estimate the variance of all the runs as:

$$S^2 = \frac{v_1 S_1^2 + v_2 S_2^2 + \cdots + v_g S_g^2}{v_1 + v_2 + \cdots + v_g}$$

where S_n^2 is the variance calculated for each $\bar{y}_n$ and $v_i = n_i - 1$ the degrees of freedom. Then, the variance of the effect can be calculated as:

$$\mathrm{V(effect)} = \frac{4}{N} S^2$$

wher N is the number of all the replicas ($\sum n_i$). The standard error of the effects is represented by the $\sqrt{\mathrm{V(effect)}}$, and the ratio between the value of the calculated effect and this standard error yield to the *t*-value. A table of values from Student's t-distribution was used to found the *p-value* of each effect.

3. Results

3.1 Characterization of sol-gel matrix

3.1.1 Porosity

Small-Angle X-ray Scattering (SAXS) approach has been exploited to characterize the structural properties of undoped sol-gel matrix resulting from the different conditions of preparation. In particular we wanted to evaluate the effects on the microstructure of the matrix of three factors: pH (6.5, 7.5 and 7.8), percent glycerol in the bulk (0 and 25%), and aging time after gelification (2 and 6 days). The experimental SAXS curves (log I(Q) vs Q), shown in **Fig. 3.1**, evidenced a monotonous decrease of the scattering intensity over the Q-range investigated (0.019 -0.460 $Å^{-1}$). To extract the information relevant to characterize the morphology of the matrix, the mass fractal model defined by Teixeira (1988) has been applied. This model describes the vitrous matrix in terms of spherical silica particles with radius R_0 that aggregate into larger clusters forming a porous network. According to the mass fractal model, the network resulting by the arrangement of the particles is also defined by the fractal dimension *d* and the cutoff distance ξ of the fractal correlation, which is interpreted as the pore size in the gels (Lelong et al., 2007). The parameters of all the experiments are summarized in **Table 3.1**. From these results it appears that that both the fractal dimension D_f and the cutoff distance ξ are not affected by changes of the three factors, while the radius R_0 decreases in presence of 25% glycerol. To better investigate the potential effect of the three factors data are represented using a box-plot approach, in which the contribution of each factor is considered independently from the other two (**Fig. 3.2**).

Glycerol (%)	pH	Aging (days)	D_f	R_0 (Å)	R_0 dispersion (%)	ξ (Å)
0	*6.5*	*2*	2.32	11.94	30%	89.59
0	*6.5*	*6*	2.35	11.50	20%	76.23
0	*7.5*	*2*	2.45	6.82	36%	89.77
0	*7.5*	*6*	2.86	8.84	25%	83.31
0	*7.8*	*2*	2.78	10.36	21%	80.54
0	*7.8*	*6*	2.04	10.67	32%	123.52
25%	*6.5*	*2*	2.93	6.27	22%	96.77
25%	*6.5*	*6*	2.36	8.31	20%	380.05
25%	*7.5*	*2*	2.61	5.00	21%	69.29
25%	*7.5*	*6*	2.22	5.00	22%	69.44
25%	*7.8*	*2*	1.93	5.09	41%	327.87
25%	*7.8*	*6*	2.83	8.05	25%	146.02

TABLE 3.1. Characteristics of silica sol-gel matrix at different conditions (% of glycerol, pH and aging) calculated from SAXS spectra. D_f is the fractal dimension; R_0 the radius of the spherical particles; R_0 dispersion (%) is the dispersion of the radius expressed in percentage; ξ is the cutoff distance.

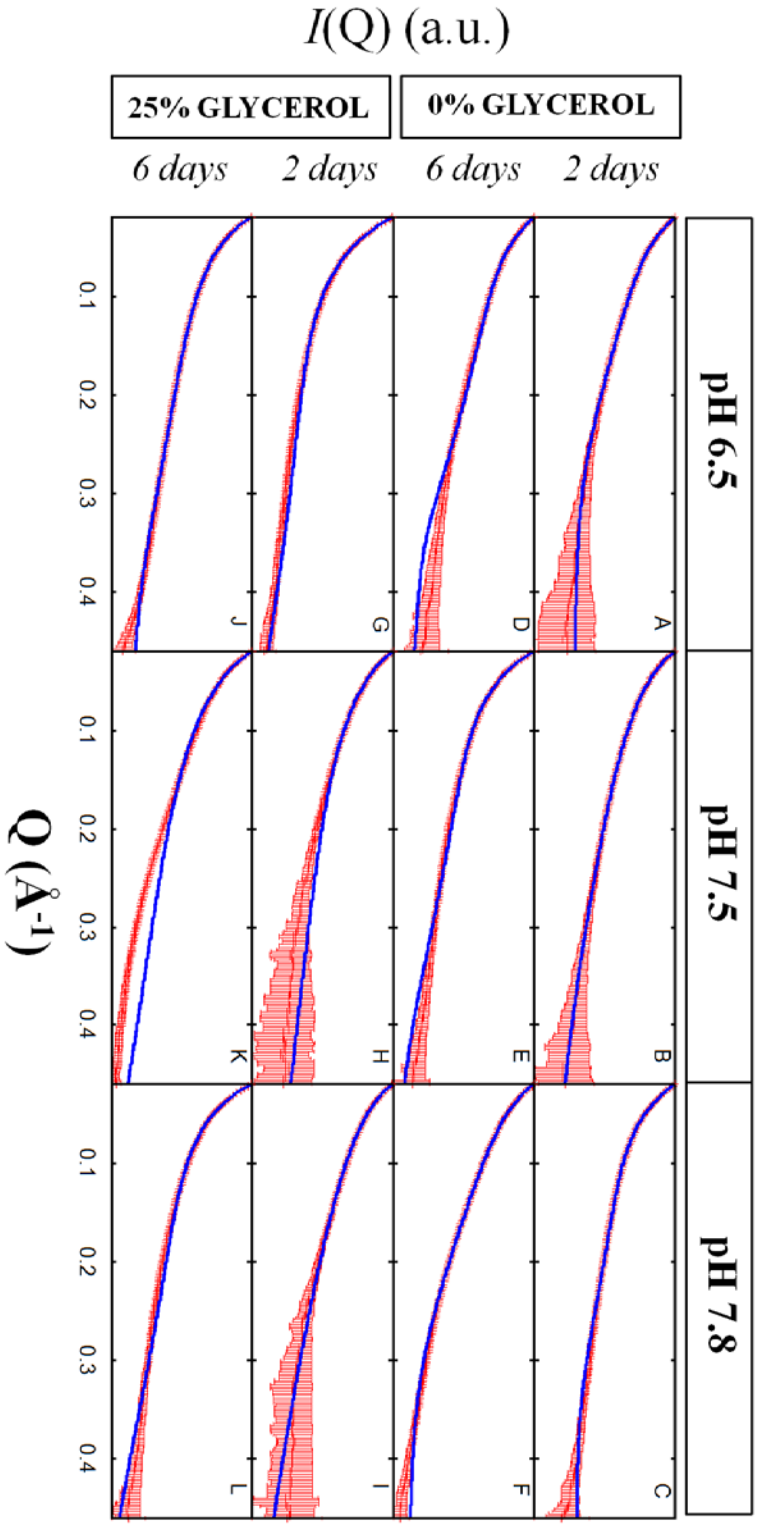

FIGURE 3.1. Semilogarithmic SAXS patterns curves (in *red*) of undoped sol-gel matrix prepared at different pH and % glycerol conditions and at different aging time. Fitting curves (in *blue*) are obtained with the fractal model of Teixeira.

Again, the box-plots confirm the effect of glycerol on the radius R_0, with a significantly decrease of the average value from 10.02±1.90Å in absence of glycerol to 6.29±1.54Å in presence of 25% glycerol (**Fig. 3.2**). On the contrary pH and aging do not affect this parameter.

More complicated is the analysis of the cutoff distance ξ due to the high variability of the results. In fact, the presence of two very high values (380.5Å and 327.87Å), identified as outliers, make difficult to estimate the effects of the three factors. The average value of ξ is 136.04±104.78Å, considering all the values, and 93.29±24.58Å without outliers. Finally, no factors effects are shown for the D_f. The average value has been calculated to be 2.46±0.29.

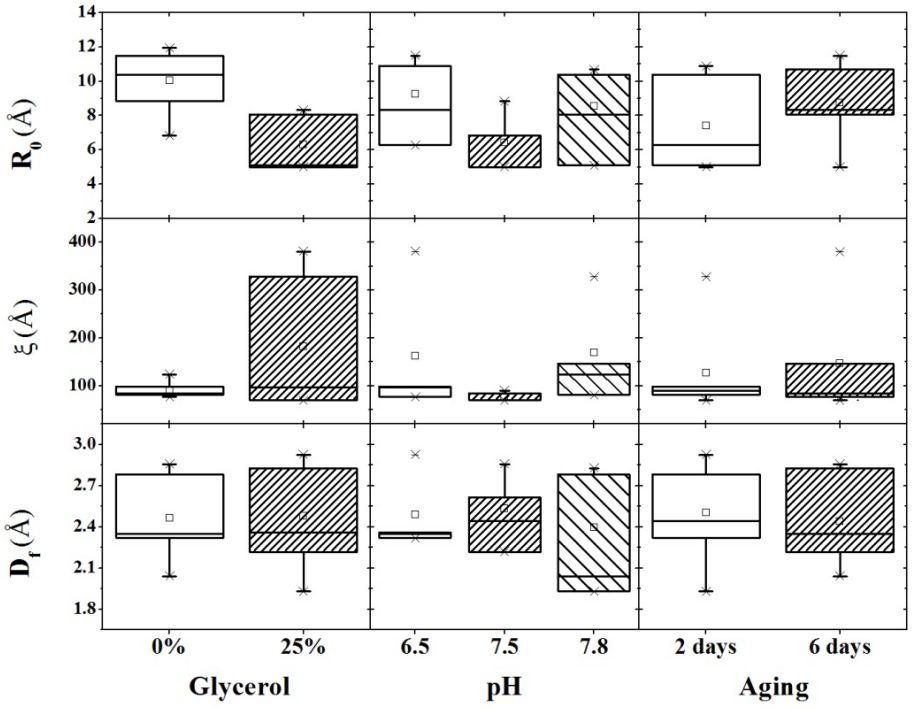

FIGURE 3.2. Box-plot representation of the radius of the spherical particles R_0, the correlation length ξ and the fractal dimension D_f of the silica matrix in presence/absence of 25% glycerol (*first column*), at pH 6.5, 7.5 and 7.8 (*second column*) and after 2 and 6 days of aging (*third column*).

3.1.2 Optical properties

The sol-gel preparation protocol does not affect only the microstructure of the silica matrix, but also modify its optical properties (West et al., 1996). Indeed, the

scattering from the silica particles forming the gel network can affect the transmission of the light, with an effect strongly dependent on the porosity of the matrix (Hench and West, 1990).

Thus, the optical properties of the sol-gel matrices, UV-visible, CD and fluorescence emission, were characterized using undoped sol-gel matrix. We firstly compared the UV spectra of sol-gel matrices prepared with a modified version of the protocol reported by Khan et al. (2000) (in our case "protocol A" with the "classic" protocol reported by Shibayama and Saigo (1995) (in our case "protocol B"). the UV-visible spectra In **Figure 3.3** are reported. For each protocol two spectra of sol-gel matrix prepared under identical conditions are shown, in order to evaluate the reproducibility of the data. The sol-gel matrices prepared following the two protocols are not characterized by flat UV spectra due to the contribution of light-scattering, and exhibit an absorption peak around 210 nm. However protocol B allows to obtain sol-gel matrix characterized by lower absorption signals at all the wavelengths. The small variability in spectral line shape of the duplicate experiments can be attributed to slight differences in the thickness of the silica gels.

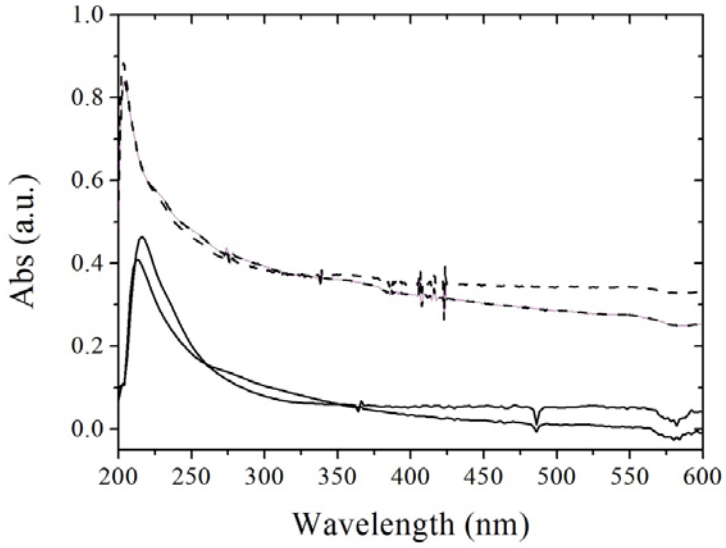

FIGURE 3.3. UV-visible absorption spectra of sol-gel matrix prepared following protocol B (*solid line***)** and protocol A (*dashed lines*). Spectra relative to two preparations for each condition are represented

Considering the better UV/visible optical properties of sol-gel matrix obtained by protocol B, and the high degree of locking in of the conformational structures of

embedded protein reported in previous studies (Samuni et al., 2003; Khan et al., 2000), we decided to adopt this protocol for all the further investigations.

Then, undoped silica gels were analyzed collecting near-UV CD spectra (**Figure 3.4**) and fluorescence emission spectra (**Figure 3.5**). While near-UV CD spectra (*solid lines*) are flat, fluorescence emission spectra (**Excitation wavelength:** 278 nm on the left; 295 nm on the right) show an higher background of the undoped matrix in comparison with the buffer. This background can be attributed to light scattering.

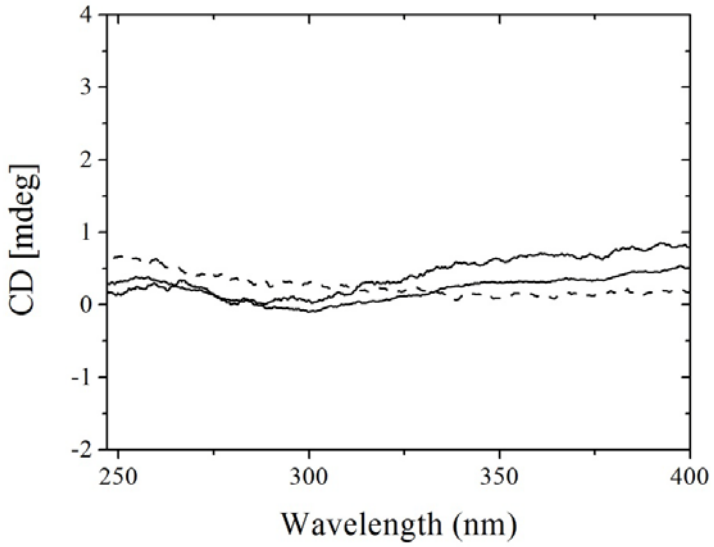

FIGURE 3.4. CD spectra of undoped sol-gel (*solid lines*), buffer (*dashed line*). Two replicas are shown for undoped sol-gel.

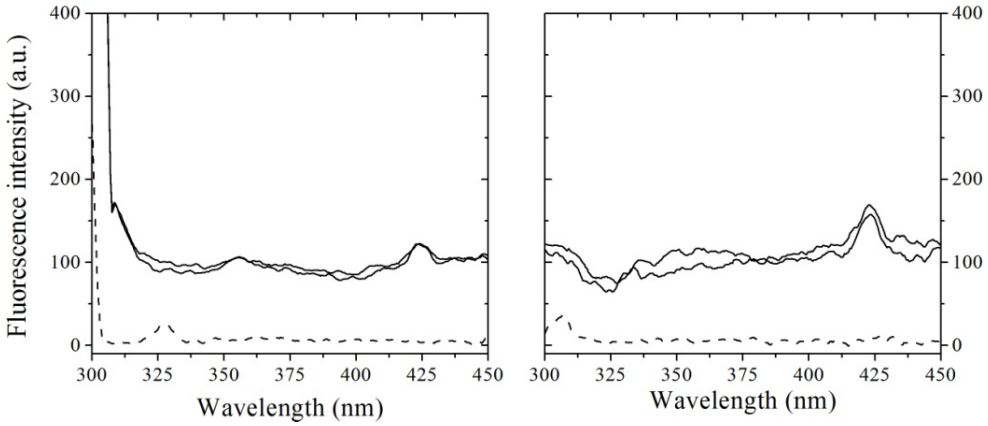

FIGURE 3.5. Fluorescence emission spectra of undoped sol-gel (*solid lines*) and buffer (*dashed line*). Two replicas are shown for undoped sol-gel matrix. **Excitation wavelength**: 295 nm *left panel* ; 278 nm *right panel.*

3.2 Hemocyanin entrapped into sol-gel matrix

Considering that sol-gel encapsulation can modify the chemical and biological properties of the entrapped species (Lin and Brown, 1997), it is very important to check the stability and the functionality of the encapsulated protein, to prove that the matrix does not alter the protein properties.

Therefore a preliminary spectroscopic analysis of hemocyanin entrapped into the matrix was performed; all the spectra were corrected for the background (undoped sol-gel matrix, **Chapter 3.1.2**). As it is shown in **Figure 3.6**, the spectra of hemocyanin in solution and in the sol-gel matrix are almost superimposable, suggesting that the native solution structure of hemocyanin is unaltered by sol-gel encapsulation. More in detail, in UV- and CD-spectra the presence of the characteristic spectroscopic feature at 338 nm (**Figure 3.6A; 3.6C**) indicates that the protein retains its functional oxygenated state in sol-gel and its ability to bind oxygen. Moreover, the emission fluorescence spectra of deoxygenated hemocyanin entrapped into the matrix are not shifted in the maximum peak, in comparison with the protein in solution (**Figure 3.6B**), suggesting that the encapsulation process doesn't alter the Tyr/Trp-structural properties of hemocyanin. The same conclusion can be drawn also from UV CD-spectra showing a superimposable lineshape for hemocyanin in solution or in sol-gel in the aromatic region (**Figure 3.6 C**).

To prove that sol-gel encapsulation doesn't affect the reversibility of the oxy-deoxygenated state of hemocyanin, UV, CD and fluorescence spectra of the same sample in presence (*solid line*) and absence (*dash-dotted line*) of oxygen (**Figure 3.7**) were collected. As expected, on going from oxy- to deoxy-hemocyanin, the 338nm band of UV and CD is abolished due to the presence of the Cu(I)-containing active site. Also the fluorescence emission signal increases as expected from the removal of the quenching effect on trp fluorescence of the active-site bound oxygen (Erker et al., 2004). The near-UV CD spectrum of hemocyanin changes upon removal of oxygen and these specral changes are the same as observed for the protein in solution. These results are important to establish that the matrix doesn't affect the diffusion of oxygen though the matrix to the active site and that the protein in sol-gel binds oxygen as in solution.

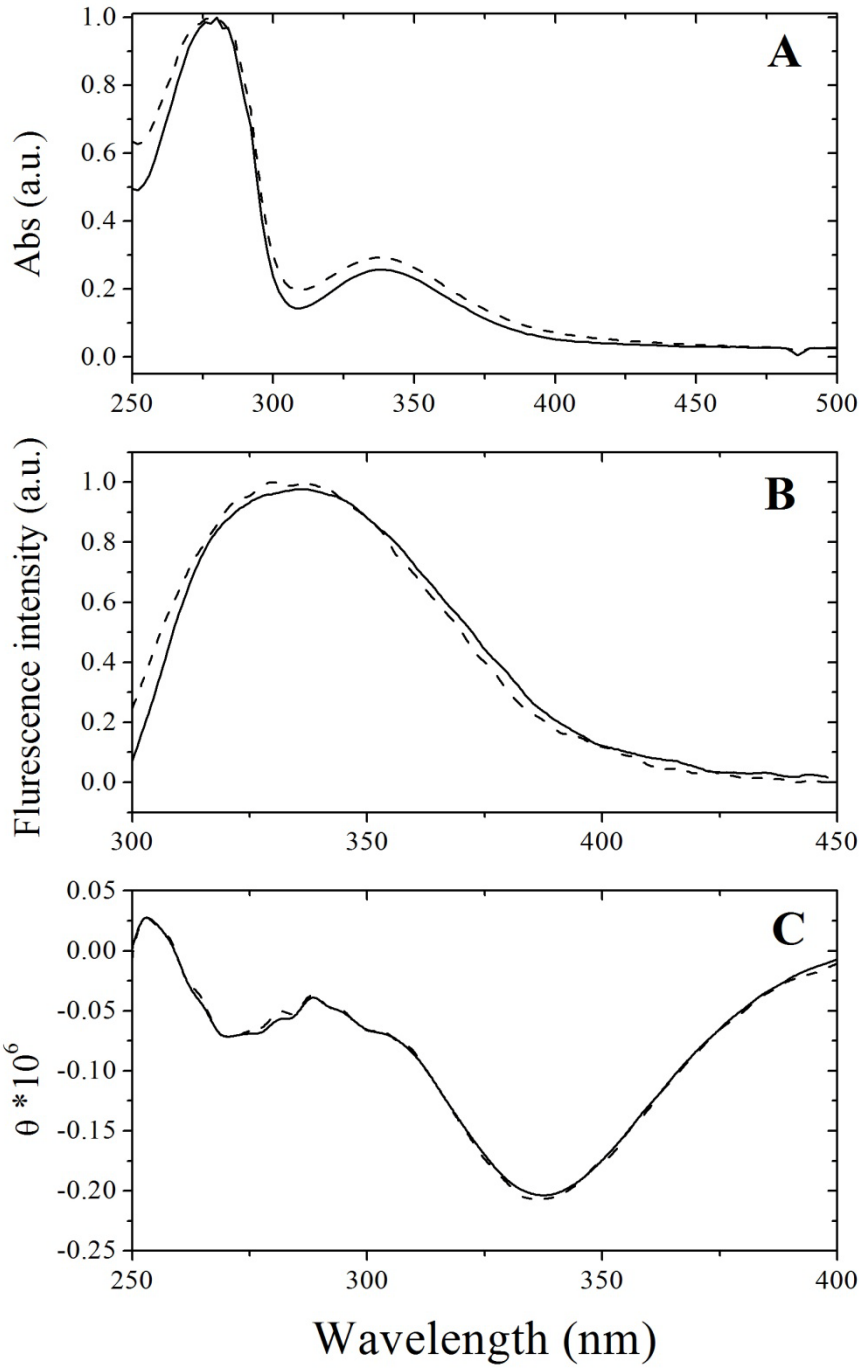

FIGURE 3.6. UV (**A**), fluorescence emission (**B**) and near-UV CD (C) spectra of hemocyanin entrapped into the sol-gel matrix (*solid line*) and in solution (*dashed line*) at pH 7.8.

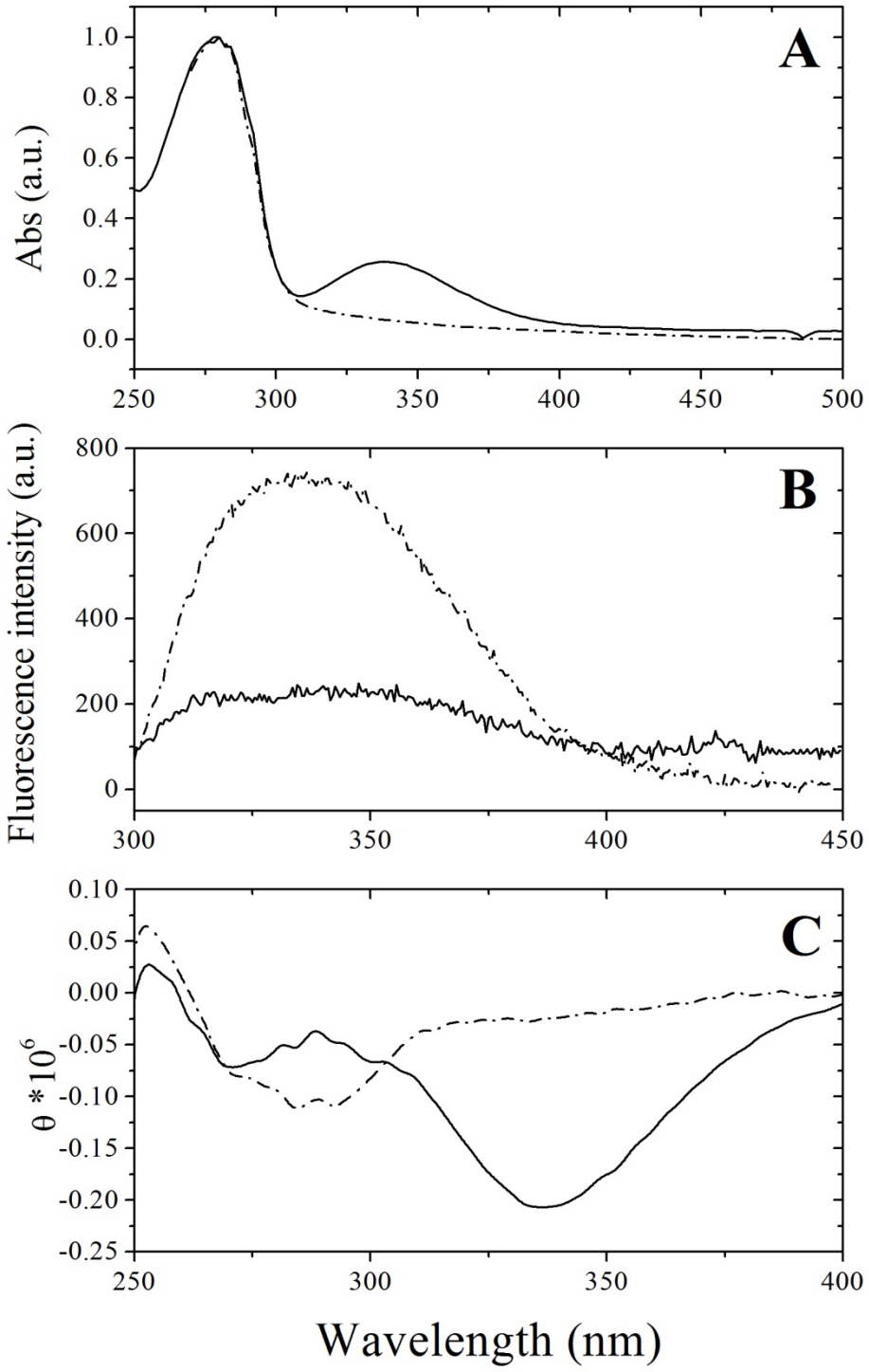

FIGURE 3.7: UV (**A**), fluorescence emission (**B**) and CD (**C**) spectra of oxygenated (*solid line*) and deoxygenated (*dash dotted line*) hemocyanin at pH 7.8.

The optical properties of *Carcinus aestuarii* hemocyanin encapsulated into the sol-gel matrix remain stable as a function of time: in a time span up to 20 days no changes in the optical properties of oxy-hemocyanin are observed (data not shown).

3.3 Oxygen and analytes diffusion through the sol-gel matrix

An important parameter to consider for the study of protein encapsulated into the sol-gel matrix is the diffusion time of the analytes. In particular, the ability of analytes to diffuse within the glass to reach the binding site of the entrapped biomolecules plays an important role in the development of biosensors (Gupta & Chaudhury, 2007). This issue is particular important for the ligand titration studies because the protein has to reach the equilibrium with the added ligand at a given concentration before further ligand additions.

Preliminarly, the time to attain the equilibrium between oxygen added in the bulk and hemocyanin in sol-gel has been estimated following the hemocyanin absorption signal at 338 nm as a function of time at different pO_2 (**Figure 3.8**). As it can be seen in the inset, the time *t* at which the signal reach the equilibrium is around 20 minutes, for our experimental paradigm.

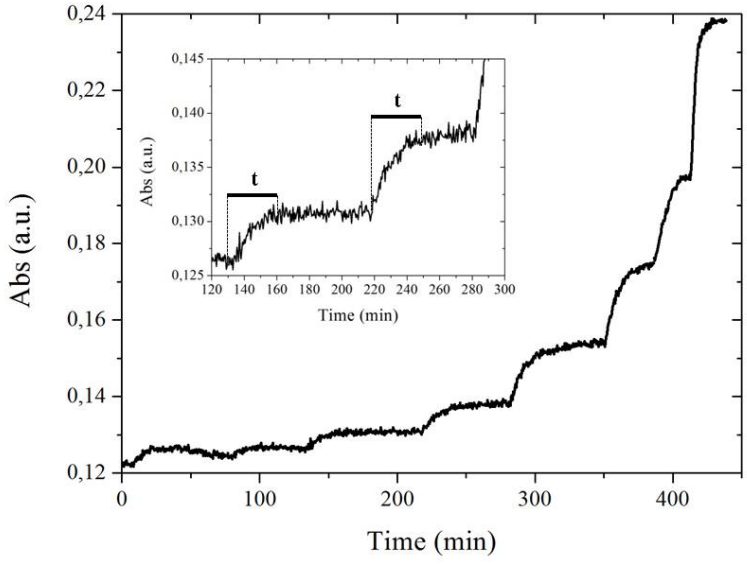

FIGURE 3.8. Absorption signal A_{338} in function of time at different pO_2

An independent evaluation of the diffusion of ligands through the matrix has been carried out using cyanide, as an example of a negatively charged ligand. The kinetics of the reaction between hemocyanin and cyanide was described as a copper between the active site and the external ligand KCN (Beltramini et al. 1984). The reaction occurs step-wise with previous formation of a complex Hc-CN between the copper bound to the protein and the ligand, followed by the decomposition of the complex and the metal displacement. Thus a decrease of the 338 nm band of oxygenated hemocyanin as a function of time is the distinctive feature of its reaction with this ligand.

The comparison between the reaction of hemocyanin in solution (*empty symbols*) and encapsulated hemocyanin (*black symbols*) indicates that the process is strongly affected by the matrix (**Figure 3.9**), due to the time required for cyanide to diffuse though the matrix to the active site of the encapsulated hemocyanin.

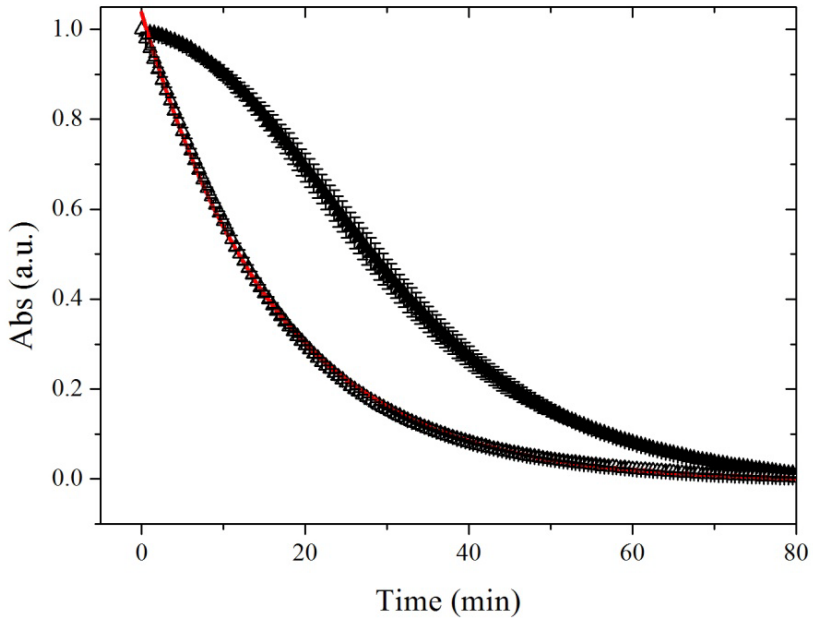

FIGURE 3.9. Comparison between the the cyanide reaction with hemocyanin in solution and in sol-gel matrix. Time dependence of the absorbance at 338 nm of oxygenated hemocyanin (~ 5 mg/ml) in solution (*empty symbols*) or in sol-gel (*black symbols*) in presence of 5mM KCN. Red line indicates the exponential fit for the reaction in solution (R-square 0.999).

As reported in literature (Beltramini et al., 1984), the effect of cyanide on the optical spectrum of hemocyanin in solution can be described by a single

exponential, as it is reported in **Figure 3.9** by empty symbols. On the contrary, in presence of silica matrix a biphasic trend is evident. In the first step the absorption signal decrease slowly due to the diffusion of cyanide through the matrix; we can consider this phase as the "diffusion step" (**Figure 3.10,** *blue arrow*). In the second step cyanide is diffused to the active site of the encapsulated hemocyanin and the reaction can be described by a single exponential, like hemocyanin in solution (**Fig. 3.9**, fit in *red*). The diffusion time *t* was calculated to be around 19 minutes, comparable with the diffusion time previously determined for oxygen.

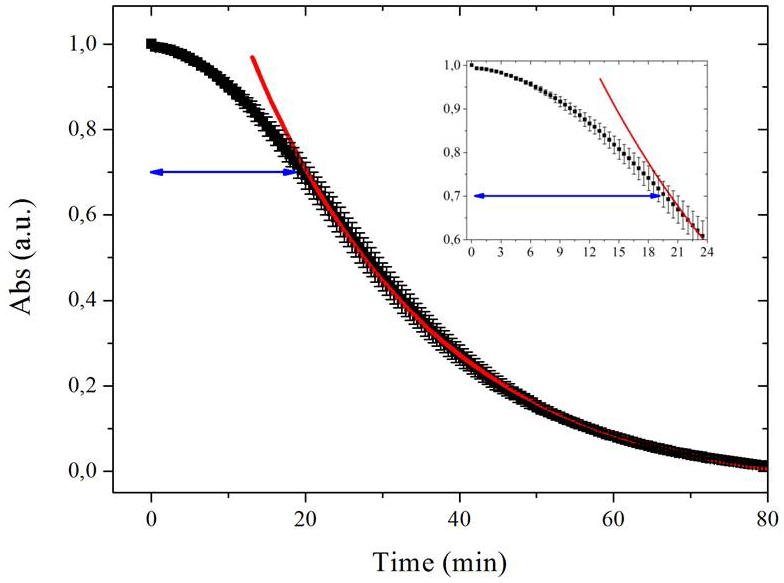

FIGURE 3.10. Time dependence of the absorbance at 338 nm of hemocyanin (~ 5mg/ml) embedded into sol-gel matrix in presence of 5mM KCN. Red line indicates the exponential fit for the reaction (R-square 0.989). Blue arrow indicates the estimated "diffusion time" of cyanide.

The different rates of the reaction, expressed by the slopes of the exponential fit in solution ($-10.20*10^{-4}\pm4.27*10^{-6}$) and in presence of the silica matrix ($-7.01*10^{-4}\pm6.89*10^{-6}$), indicates that the metal displacement of encapsulated hemocyanin requires longer time than hemocyanin in solution. This observation can be explained by the influence of the initial "diffusion step" on the rate of the reaction.

3.4 Glycerol effect on the functional and structural properties of hemocyanin

Since the protocol used for hemocyanin encapsulation involves the presence of glycerol, before the characterization of the hemocyanin entrapped into the sol-gel matrix, we evaluated the effect of glycerol on the properties of the protein in solution. These preliminary analysis are required in order to exclude possible glycerol-induced alterations of hemocyanin. Indeed, it has been demonstrated that glycerol may alter proteins in a number of ways (Farnum and Zukoski,1999); a typical effect is the decrease of the volume of the protein, with a reduction in the size of the core (Priev et al., 1996). An increase in the size of the hydratation layers was also suggested.

Oxygen-binding curves for hemocyanin in solution at pH 7.8 were performed, both in presence and absence of 25% glycerol. As it is shown in **Fig. 3.11**, the two curves show a very similar sigmoidal behavior, suggesting no effects of glycerol on the functional properties of the protein.

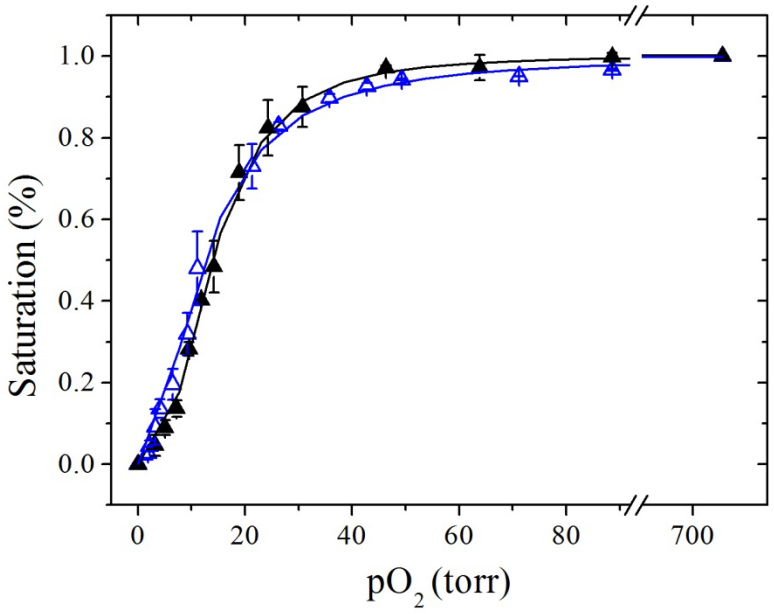

FIGURE 3.11. Oxygen binding curves of hemocyanin in solution at pH 7.8 both in presence and absence of 25% glycerol. Average and standard deviation resulting from 3 replicas.

This result was also confirmed by the comparison of the *p50* and the cooperativity index *n* obtained by the fits of the two curves (**Table 3.2**), with no significant differences (p>0.05) in presence and absence of glycerol.

Glycerol	p50 (torr)	*n*
0%	13.00 ± 1.07	2.22 ± 0.25
25%	13.94 ± 0.69	2.64 ± 0.20

TABLE 3.2. Oxyen binding parameters (mean values ± standard deviation) of hemocyanin in solution at pH 7.8, in presence and absence of glycerol. Average and standard deviation resulting from 3 replicas.

The evaluation of possible structural modifications of hemocyanin was performed through fluorescence and CD spectroscopy. By exploiting these techniques, the decrease of the core size of hemocyanin should result in shifts of the fluorescence emission peaks and/or changes in the shape of the CD spectra in the aromatic region. In this case, it seems that glycerol does not affect the hemocyanin interior; indeed almost superimposable fluorescence and Near-UV CD spectra were obtained (**Fig. 3.12**; **Fig. 3.13**).

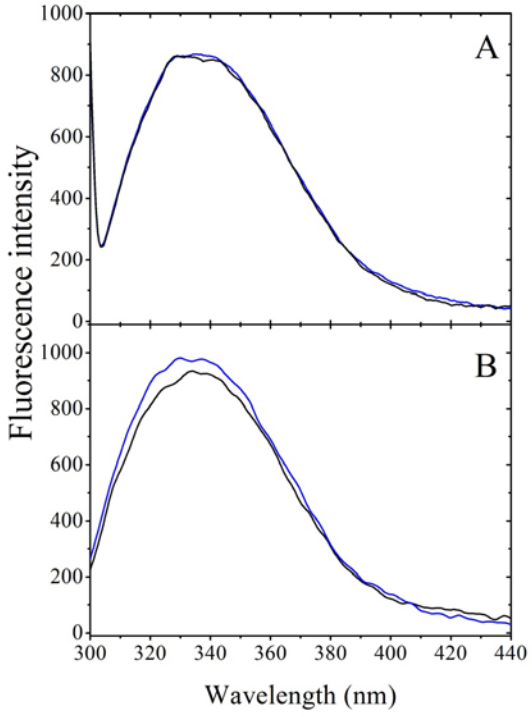

FIGURE 3.12. Emission spectra of deoxygenated hemocyanin in solution in presence (in *blue*) and absence (in *black*) of 25% glycerol at pH 7.8. **Excitation wavelength**: 295 nm (**A**) and 278 nm (**B**).

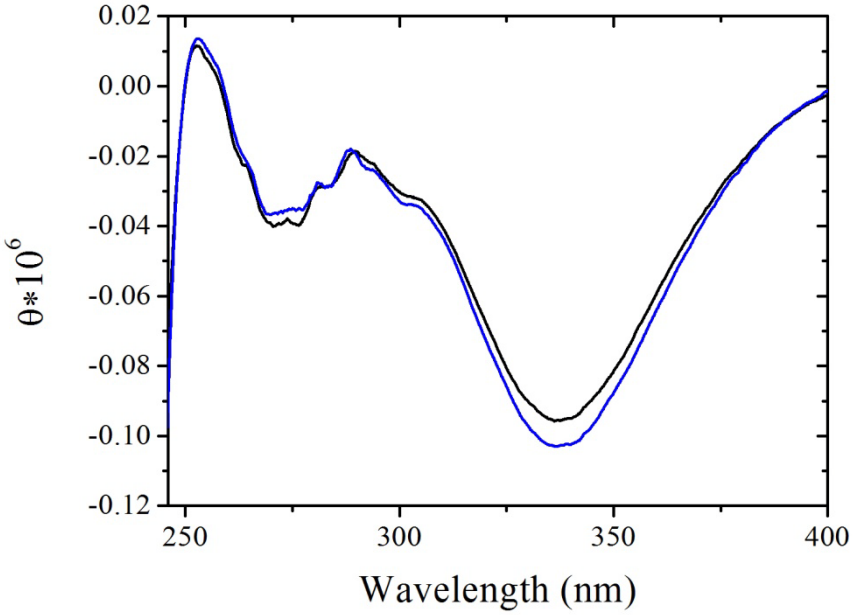

FIGURE 3.13. Near-UV CD spectra of deoxygenated hemocyanin in solution in presence (in *blue)* and absence (in *black*) of 25% glycerol at pH 7.8.

3.5 Encapsulation of hemocyanin in a specific conformational state

To determine if the protocol of polymerization of the sol-gel is a suitable way to trap hemocyanin in a single conformational state, we compared the oxygen-binding curves of the protein in solution and entrapped into the sol-gel matrix at pH 6.5 (**Figure 3.14**), 7.5 (**Figure 3.16**) and 7.8 (**Figure 3.18**). As expected for cooperative proteins, the oxygen binding curve of hemocyanin in solution can be described by a sigmoidal function, in which the Hill coefficient *n* provides a way to quantify the magnitude of the cooperativity process. The embedding of hemocyanin into the sol-gel matrix, instead, avoids the transition between the different conformational states resulting in a hyperbolic oxygen binding behavior. The binding curves were analyzed also according to the Hill-plots (**Figures 3.15, 3.17, 3.19**), providing a faster way to evaluate the effect of embeddeding hemocyanin into the sol-gel matrix.. The results are reported in **Table 3.3**.

Hemocyanin entrapped into the matrix at pH 6.5 (**Figure 3.14**), both in presence and absence of oxygen, displays non-cooperative oxygen binding behavior compared to the protein in solution (n=2.48±0.17); indeed the cooperativity index n for the protein entrapped in presence of oxygen is 0.90±0.06, not significantly

higher than *n*=1 (p>0.05) and 0.82 for the pretein entrapped in absence of oxygen. Also the oxygen-binding affinities p50 are different from the p50 of the protein in solution: 43.92±2.20 torr (p<0.05) and 736.42 torr for hemocyanin into the sol-gel, prepared in presence and absence of oxygen, versus 74.80±2.37 torr for the protein in solution. Following the classical notation of MWC model, hemocyanin has the properties of the T- or R-conformer when entrapped in the deoxygenated or oxygenated state, respectively.

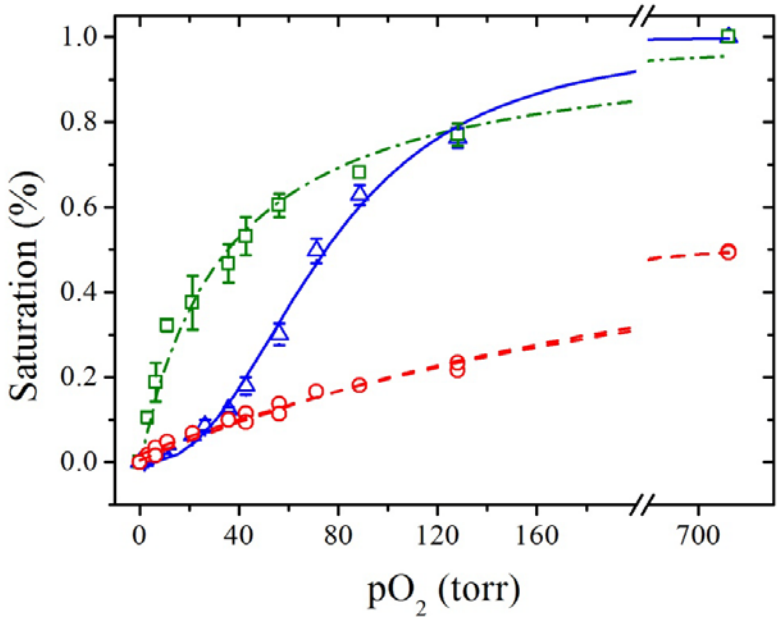

FIGURE 3.14. Oxygen binding curves of hemocyanin in solution (*in blue*), entrapped in absence (*in red*) and in presence (*in green*) of oxygen at pH 6.5. Solid, dash-dotted and dashed lines represent respectively the best fits of the points for the hemocyanin in solution, entrapped in presence and absence of oxygen. Average and standard deviation resulting from 3 replicas for R-state and protein in solution. 2 replicas for the T-state are shown.

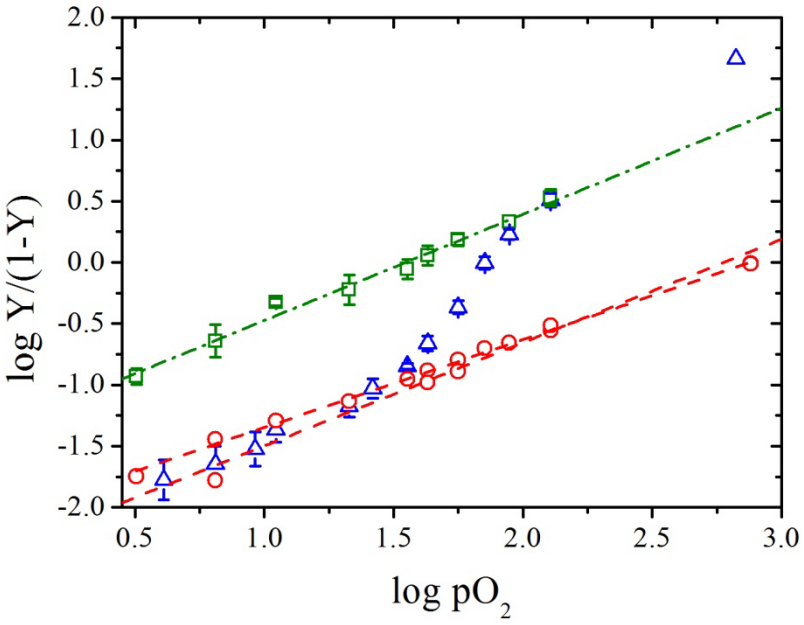

FIGURE 3.15. Hill-plot of hemocyanin in solution (*in blue*), entrapped in absence (*in red*) and in presence (*in green*) of oxygen at pH 6.5. Dash-dotted and dashed lines represent the best linear fits of the points for the hemocyanin entrapped in presence and absence of oxygen, respectively. Average and standard deviation resulting from 3 replicas for R-state and protein in solution. 2 replicas for the T-state are shown.

The overall oxygen binding behavior of entrapped hemocyanin at pH 7.5 is more complicated than the one observed at pH 6.5. Also at this pH value, hemocyanin embedded into the matrix in presence of oxygen shows non-cooperative oxygen binding behavior, as demonstrated by the cooperativity index n=1.03, very close to 1. On the contrary hemocyanin entrapped in absence of oxygen is characterized by an index n=1.48 higher than 1, although lower than that of the protein in solution (n=3.28). The p50 have been calculated as 13.64 torr for the oxy-entrapped hemocyanin and 33.77 torr for the deoxy-entrapped hemocyanin, both different from the oxygen affinity (22.45 torr) of the protein in solution. Moreover, at this pH an higher variability of the measures was observed.

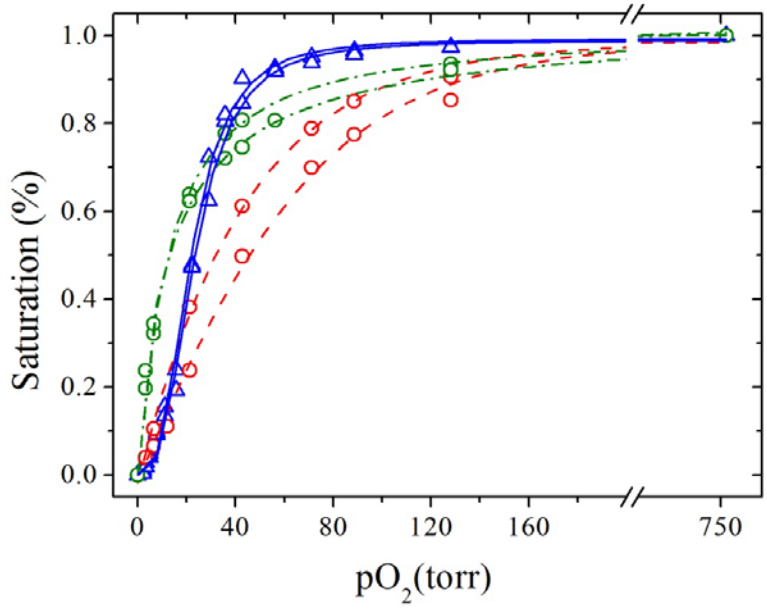

FIGURE 3.16. Oxygen binding curves of hemocyanin in solution (*in blue*), entrapped in absence (*in red*) and in presence (*in green*) of oxygen at pH 7.5. Solid, dash-dotted and dotted lines represent respectively the best fits of the points for the hemocyanin in solution, entrapped in presence and absence of oxygen. 2 replicas for all the experimental conditions are shown.

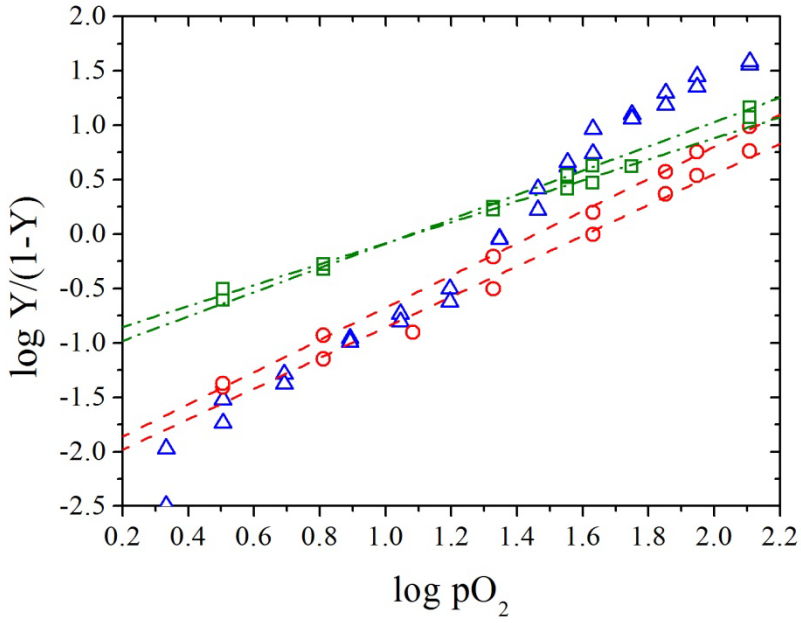

FIGURE 3.17. Hill-plot of hemocyanin in solution (*in blue*), entrapped in absence (*in red*) and in presence (*in green*) of oxygen at pH 7.5. Dash-dotted and dashed lines represent the best linear fits of the points for the hemocyanin entrapped in presence and absence of oxygen, respectively. 2 replicas for all the experimental conditions are shown.

Finally, at pH 7.8 the cooperativity index *n* of both the oxygenated (1.36±0.09) and deoxygenated conformers (1.27±0.02**)** are significantly higher than 1 ($p<0.05$), but significantly lower than the *n* value of hemocyanin in solution at the same pH (2.22±0.25) ($p<0.05$). The oxygen-binding affinity p50 of hemocyanin entrapped in presence of oxygen (10.70±1.11 torr) is lower than the p50 of hemocyanin in solution (13.03±1.07 torr), but not significantly different ($p>0.05$). On the contrary, hemocyanin entrapped in absence of oxygen shows a significantly higher value of p50 (19.92±1.29 torr) ($p<0.05$).

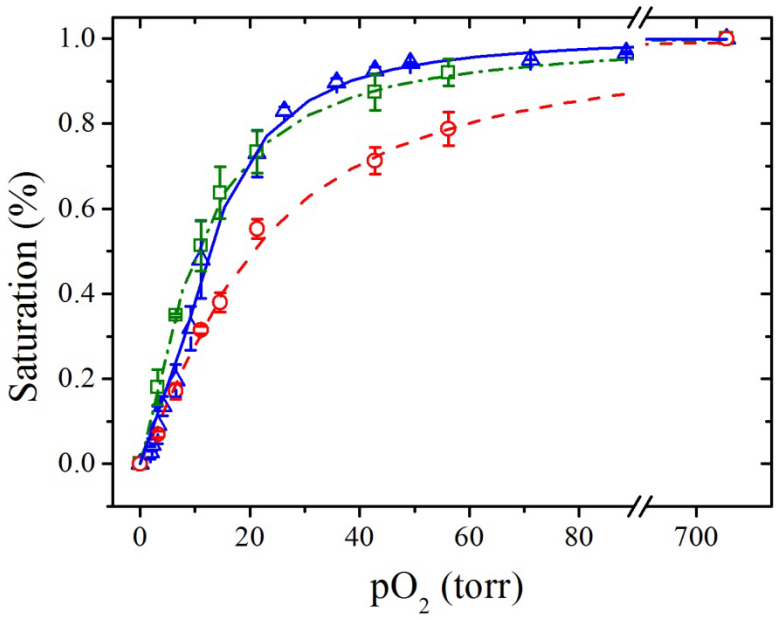

FIGURE 3.18. Oxygen binding curves of hemocyanin in solution (*in blue*), entrapped in absence (*in red*) and in presence (*in green*) of oxygen at pH 7.8. Solid, dotted and dash-dotted lines represent respectively the best fits of the points for the hemocyanin in solution, entrapped in presence and absence of oxygen. Average and standard deviation resulting from 3 replicas.

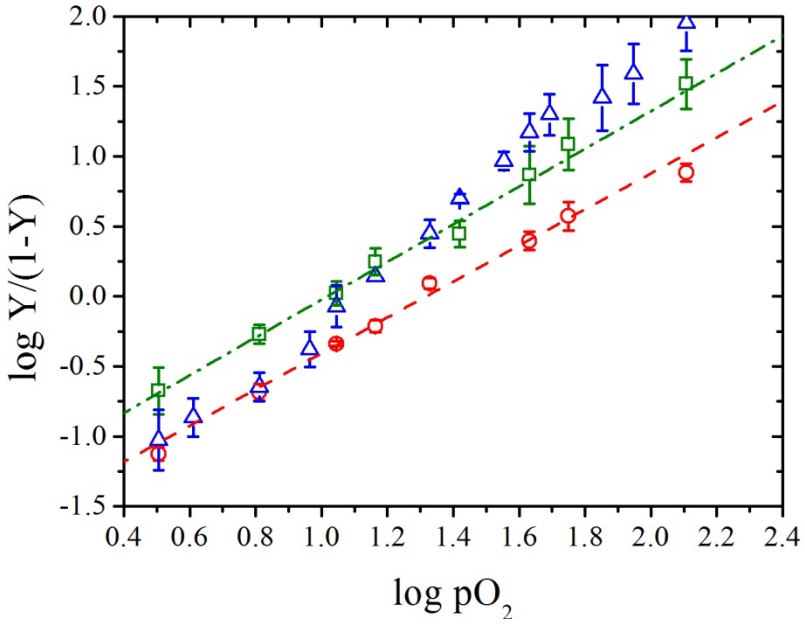

FIGURE 3.19. Hill-plot of hemocyanin in solution (*in blue*), entrapped in absence (*in red*) and in presence (*in green*) of oxygen at pH 7.8. Dotted and dash-dotted lines represent the best linear fits of the points for the hemocyanin entrapped in presence and absence of oxygen, respectively. Average and standard deviation resulting from 3 replicas.

		p50 (torr)	n
pH 6.5	***Solution***	74.80±2.37	2.48±0.17
	R-state	43.92±2.20	0.90±0.06
	T-state	736.42	0.82
pH 7.5	***Solution***	22.45	3.28
	R-state	13.64	1.03
	T-state	33.77	1.48
pH 7.8	***Solution***	13.03±1.07	2.22±0.25
	R-state	10.70±1.11	1.36±0.09
	T-state	19.93±1.30	1.27±0.02

TABLE 3.3. Oxygen binding properties of hemocyanin in solution and embedded into sol-gel matrix in presence (R-state) and absence (T-state) of oxygen. Average and standard deviation resulting from 3 replicas at pH 7.8 for all the conformers and at pH 6.5 for the protein in solution and the R-state. In all the other cases is reported the average of 2 replicas.

These results suggest the entrapment at pH 6.5 and 7.8 of hemocyanin in two different conformational states, that we can consider as the high-oxygen affinity state R and the low-oxygen affinity state T. The suitability of sol-gel process to

"block" hemocyanin in one of the two different states at these pH is also visually confirmed by the Hill plots (**Figure 3.15; Figure 3.19**): sigmoidal curves of hemocyanin in solution are embraced between two asymptotes, corresponding to the R- asymptote and the T- asymptote of the solution curves. Instead no safe conclusion can be drawn at pH 7.5 about the behavior of hemocyanin in sol-gel, due to the non asymptotic Hill-plots obtained (**Figure 3.17**).

3.6 Analysis of the functional properties of hemocyan in solution and into the sol-gel matrix in terms of allosteric models.

The oxygen equilibrium data phenomenologically described in **section 3.5** were analyzed in terms of the different allosteric models described in literature for hemocyanins. At first, we tried to analyzed our data according to the simple two state MWC model, assuming the entrapment of the R- and T-state into the silica matrix. The analysis of equilibrium data for hemocyanin in solution yields the K_R and K_T ($torr^{-1}$) summarized in **Table 3.4**. These values are compared with those obtained with hemocyanin in sol-gel. K_T of hemocyanin into the matrix seems to correspond to the value predicted by MWC model for hemocyanin in solution at pH 6.5, while at pH 7.8 an higher value was evidenced. On the contrary, K_R of the conformer at pH 7.8 is lower than the values of the equilibrium constant of hemocyanin in solution at this pH. At pH 6.5 no differences are evidenced between the K_R predicted and the one obtained by the experimental data (**Table 3.4**).

		K_R ($torr^{-1}$)	K_T ($torr^{-1}$)	Log L_0
pH 6.5	***Solution***	0.032±0.004	0.002±0.000	2.65±0.22
	R-state	0.022±0.000	-	-
	T-state	-	0.0013	-
pH 7.8	***Solution***	0.352±0.106	0.029±0.005	3.84±0.02
	R-state	0.094±0.006	-	-
	T-state	-	0.050±0.002	-

TABLE 3.4. Oxygen binding properties of hemocyanin in solution and embedded into sol-gel matrix. K_R and K_T are calculated according to the MWC model described for hemocyanin in solution. Average and standard error resulting from 3 replicas. The average of 2 replicas is shown for T-state at pH 6.5. The value of the equilibrium constant L was not reported for the hemocyanin entrapped into the silica matrix because we assumed the fully entrapment of distinct conformers.

The discrepancies observed at pH 7.8 suggest a more complicated oxygen binding process than the one described by the MWC model, with more than two conformers involved. Therefore we analyzed the oxygen binding curves through the extension of the two-state MWC model that includes one more conformation, yielding the three-state model. At pH 6.5, the three binding constants obtained by the fit of hemocaynin in solution are K_R=0.166, K_S=0.034 and K_T=0.002 torr^{-1}, with the allosteric equilibrium between the different conformers defined by the log L_S=10.32 and the log L_T=13.06. Interesting, the K_R of hemocyanin entrapped in presence of oxygen (K_R=0.022 torr^{-1})) is very similar to the K_S of the fit (0.034 torr^{-1}), suggesting the block of the S-state but not of the R-state at this pH, as confirmed by the Hill-plot in **Fig. 3.20**. Instead, the predicted T-state seems to corresponds quite well with the plot of the protein entrapped in absence of oxygen (in *red*).

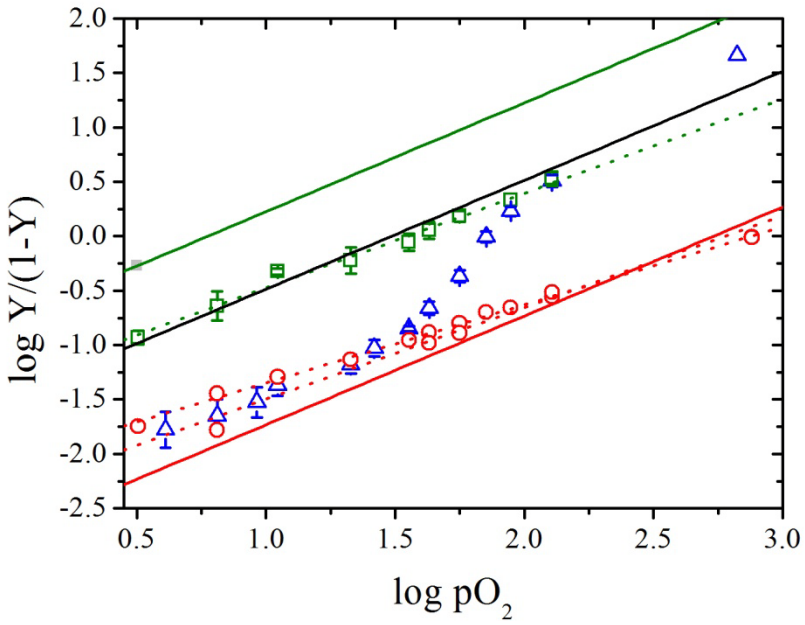

FIGURE 3.20. Hill-plot of the protein in solution (in *blue*) and embedded into the sol-gel matrix in presence (symbols and dotted line in *green*) and absence (symbols and dotted line in *red*) of oxygen at pH 7.8. The solid lines indicates the T- (in *red*), S- (in *black*) and R- (in *green*) states predicted by the three state model. Average and standard deviation resulting from 3 replicas for R-state. 2 replicas for the T-state are shown.

At pH 7.8, the binding constants obtained by the fit are K_R=0.359, K_S=0.065 and K_T=0.010 torr^{-1}, and the allosteric equilibrium constants are log L_S=1.31 and log

L_T=1.61. The lower values of the constants L_S and L_T at pH 7.8 compared to the ones at pH 6.5 indicate a shift of the equilibrium towards higher conformational states, as expected. As represented in the Hill-plot in **Fig. 3.21**, the three-state model allows to better interpret the different equilibrium constants observed for the encapsulated hemocyanin. Indeed, at this pH, sol-gel matrix seems to avoid the allosteric transition between the T- and R-state, but not between the S-state and the R-state (symbols and dotted line in *green)*, and between the T-state and the S-state (symbols and dotted line in *red)*. So, the oxygen binding curves obtained at pH 7.8 could be considered as resulting from the population of states from S to R, when the hemocyanin was entrapped in presence of oxygen, and from T to S, when deoxygenated hemocyanin was embedded into the matrix. The presence of a mix of different conformers explains the slight positive cooperativity of the entrapped hemocyanin observed at pH 7.8 (**Chapter 3.5**).

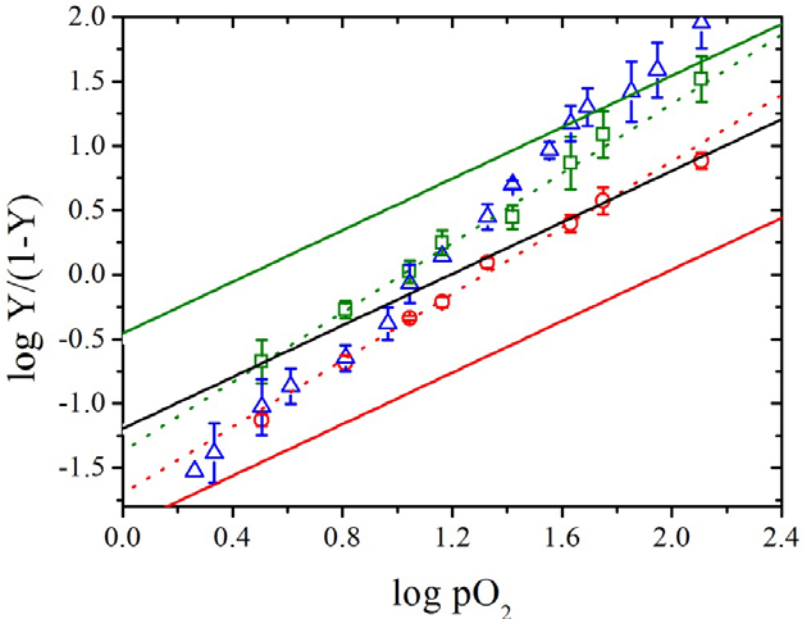

FIGURE 3.21. Hill-plot of the protein in solution (in *blue*) and embedded into the sol-gel matrix in presence (symbols and dotted line in *green*) and absence (symbols and dotted line in *red*) of oxygen at pH 7.8. The solid lines indicates the T- (in *red*), S- (in *black*) and R- (in *green*) states predicted by the three state model. Average and standard deviation resulting from 3 replicas.

Taken together these results show that at pH 7.8 two different conformers can be structurally characterized when hemocyanin is entrapped in the oxygenated form:

the fully oxygenated R-state (**Fig. 3.22**; **B**: *green* arrow) and the fully deoxygenated S-state (**Fig. 3.22**; **B**: *black* arrow). The entrapment of hemocyanin in absence of oxygen instead lead to an oxygenated S-state (**Fig. 3.22**; **B**: *black* arrow) and a deoxygenated T-state (**Fig. 3.22**; **B**: *red* arrow). Instead, at pH 6.5 only the S- and T-conformer, both in presence and absence of oxygen, can be investigated (**Fig. 3.22**; **A**).

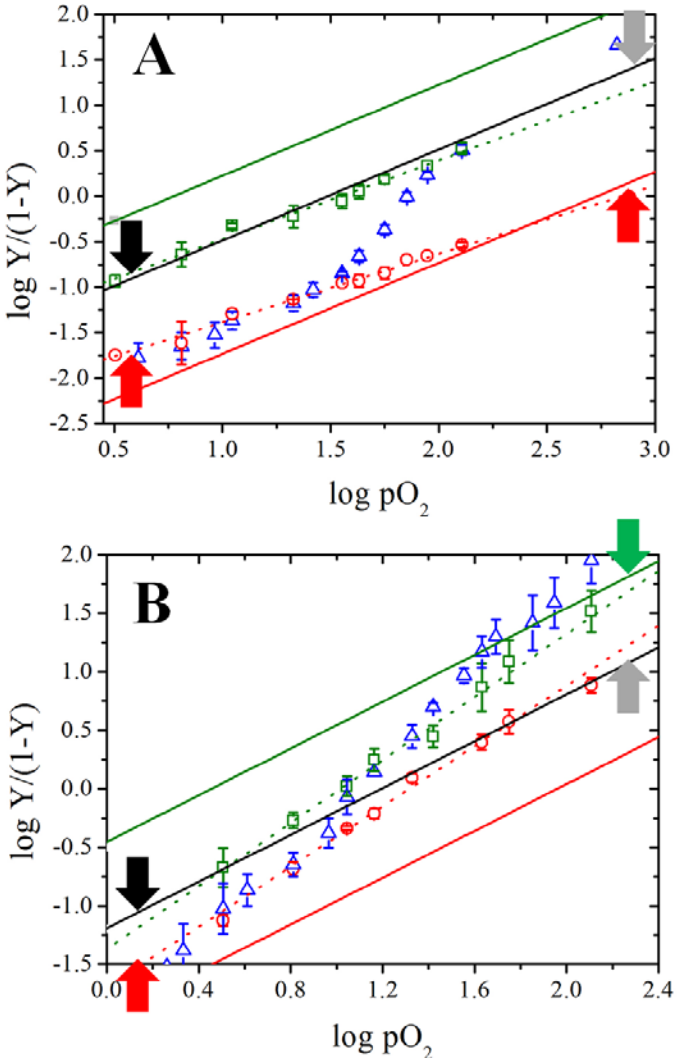

FIGURE 3.22. Legend of the conformers entrapped into the sol-gel matrix, at pH 6.5 (**A**) and 7.8 (**B**). Arrows are used to indicate the entrapped conformers in the oxygenated (higher log pO_2) and deoxygenated form (lower log pO_2). *Green* arrows: R-state; *red* arrows: T-state; *black* and *gray* arrows: S-state.

According to the legend in **Fig. 3.22**, in the next chapters we will indicate the R-state in *red*, the S-state oxygenated and deoxygenated in *gray* and *black*, respectively, and the T-state in *green*.

3.7 Structural characterization of hemocyanin conformers

3.7.1 Near-UV CD and fluorescence emission spectra of hemocyanin entrapped into the silica matrix.

A further validation for the entrapment of hemocyanin in distinct conformers was obtained by CD and fluorescence spectroscopy. Fluorescence emission spectra of hemocyanin in solution at pH 7.8 (in *blue*), entrapped in S-state (in *gray*) and in T-state (in *red*) were collected using either 278 nm (**Fig. 3.24**) and 295 nm (**Fig. 3.23**) excitation. Excitation at 278 nm excites both tryptophan and tyrosine, while excitation at 295 nm or higher selectively excites tryptophan. As it is shown in **Fig. 3.23**, the fluorescence emission spectra of hemocyanin conformers are very similar to the one of protein in solution when hemocyanin is excited at 295 nm.

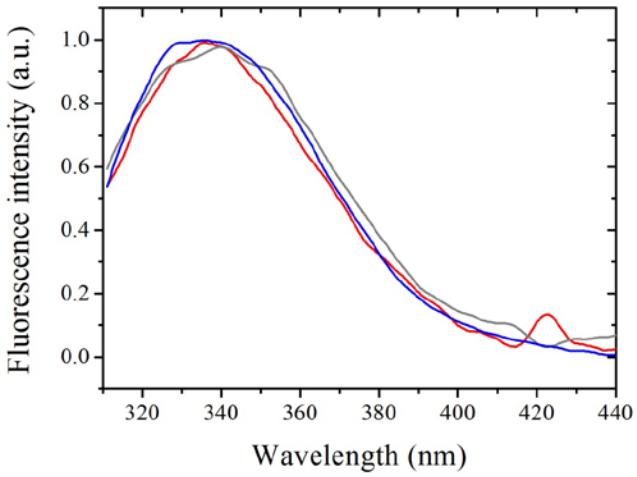

FIGURE 3.23. Emission spectra of deoxygenated hemocyanin in solution at pH 7.8 (in *blue*), entrapped in S-state (in *gray*) and T-state (in *red*). **Excitation wavelength:** 295 nm

Upon an excitation at 278 nm, the lineshape of spectra show some distinct differences (**Fig. 3.24**). While hemocyanin in solution and entrapped in T-state have an emission maximum near 340 nm, the entrapment of hemocyanin in S-state shifts the maximum peak of emission to 320 nm. Considering also the results shown in **Fig. 3.23**, this shift in the emission maximum can be attributed to different exposure of tyrosine (but not tryptophan) residues to the solvent (Favilla

2002, Hubler 1998, Ricchelli 1980), due to the different tertiary structures of the two conformers.

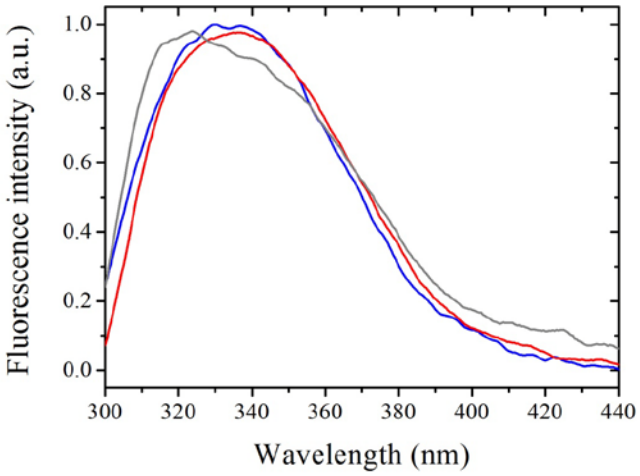

FIGURE 3.24. Emission spectra of deoxygenated hemocyanin in solution at pH 7.8 (in *blue*), entrapped in S-state (in *gray*) and in T-state (in *red*). **Excitation wavelength:** 278 nm.

Near-UV/visible CD spectra of oxy-hemocyanin conformers are shown in **Figures 3.25** and **3.26**. The negative ellipticity centered at 345 nm corresponds to the O_2^{2-}-to- Cu(II) LMCT transition of oxygenated hemocyanin, similar to the protein in solution. The CD intensity in this spectral region indicates that the ellipticity of the peroxide complex of oxygenated hemocyain is the same for both the protein in solution and in sol-gel. Furthermore no differences are evident between the conformers that have been entrapped under oxygenated or deoxygenated conditions. In contrast, the CD lineshape in the aromatic region reveals differences between the protein in sol-gel and in solution. In particular, in the presence of oxygen, the spectra of hemocyanin in solution and entrapped in R-state are almost indistinguishable, while the entrapped S-state shows significantly lower CD intensity in the 260-280 nm range where tyrosine residues contribute to the spectrum (**Figure 3.25**). The CD spectra of deoxygenated hemocyanin are shown in **Figure 3.26**. The deoxy-hemocyanin spectra are expected to lack the negative band at 345 nm due to the removal of peroxide, yet the residual negative ellipticity at this wavelength indicates that the sample still contains ~10% of oxygenated hemocyanin. Under these conditions no safe conclusion can be taken

of the spectral features in the near-UV due to the interference of the 345 nm residual band that has a different intensity in the various preparations (**Figure 23**).

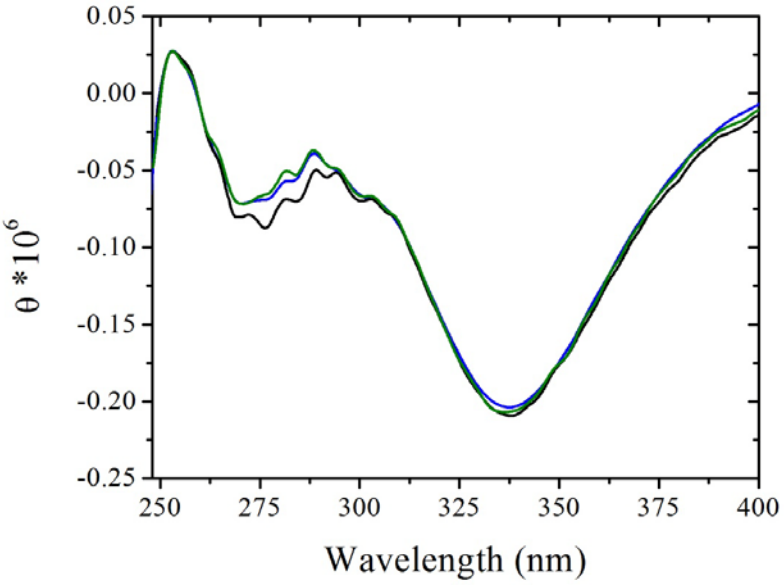

FIGURE 3.25. Near-UV/visible CD spectra of oxygenated hemocyanin in solution (in *blue*), entrapped in R-state (in *green*) and in S-state (in *black*) at pH 7.8.

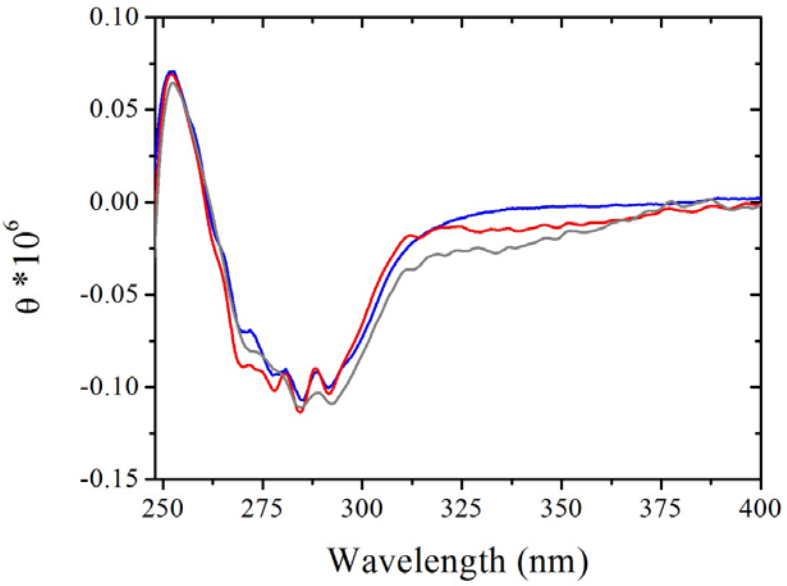

FIGURE 3.26. Near-UV/visible CD spectra of deoxygenated hemocyanin in solution (in *blue*), entrapped in S-state (in *gray*) and in T-state (in *red*) at pH 7.8.

3.7.2 Small-Angle Neutron Scattering (SANS) investigation

To validate the "three state model" applied to describe the oxygen binding curves at pH 7.8, Small-Angle Neutron Scattering (SANS) measurements have been carried out at ILL neutron radiation facility to characterize the structure of the conformers, both in the oxy- and deoxygenated state. SANS was used to this aim due to its potential in dissecting the structure of biological systems with multiple components (Neylon, 2008). The possibility to separate the scattering signatures of the protein and the sol-gel using deuterium labeling and phase-constrast variation has been already demonstrated (Lou et al., 2009).

Our first aim was to find the optimum amount of D_2O and (H_2O) for the preparation of the samples, in order to remove the contribution of the silica matrix to the experimental scattering pattern. According to atomic scattering lengths, molecular volumes and exchangeable hydrogens of all the species and also considering the volume contraction that follows the polymerisation of the tetramethyl orthosilicate (TMOS), we had found the theoretical value of the deuteration grade (X_D=0.73) to achieve a perfect match between the scattering length density of the gel (in *orange*) and the one of the hydrating solution (in *blue*) (**Fig. 3.27**).

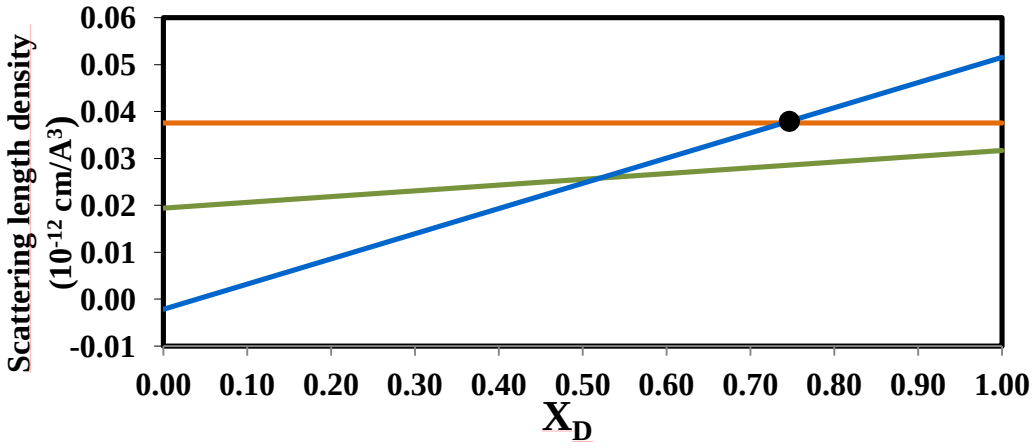

FIGURE 3.27. Scattering length density (SLD) of buffer (*in blue*), sol-gel matrix (*in orange*) and hemocyanin (*in blue*). The theoretical value of X_D at which silica matrix is perfectly matched is 0.73 (*black circle*).

The optimum X_D value was also experimentally determined through the measurements of sol-gel matrices without trapped hemocyanin at four different

X_D: 0.6, 0.70, 0.80 and 0.86. Initially, samples were prepared directly at the specific X_D, but D_2O seemed to affect the gelification process of the matrix. Therefore, we decided to prepare samples from H_2O and, once the sol-gel polymerized, dialyzed them against the solutions at the four X_D. To permit the diffusion of the mother solution through the matrix, the gels were polymerized into quartz cuvette (1 mm and 2mm thickness) with both ends open. SANS profiles exhibited by these gels are shown in **Fig. 3.28 (A-B)**.

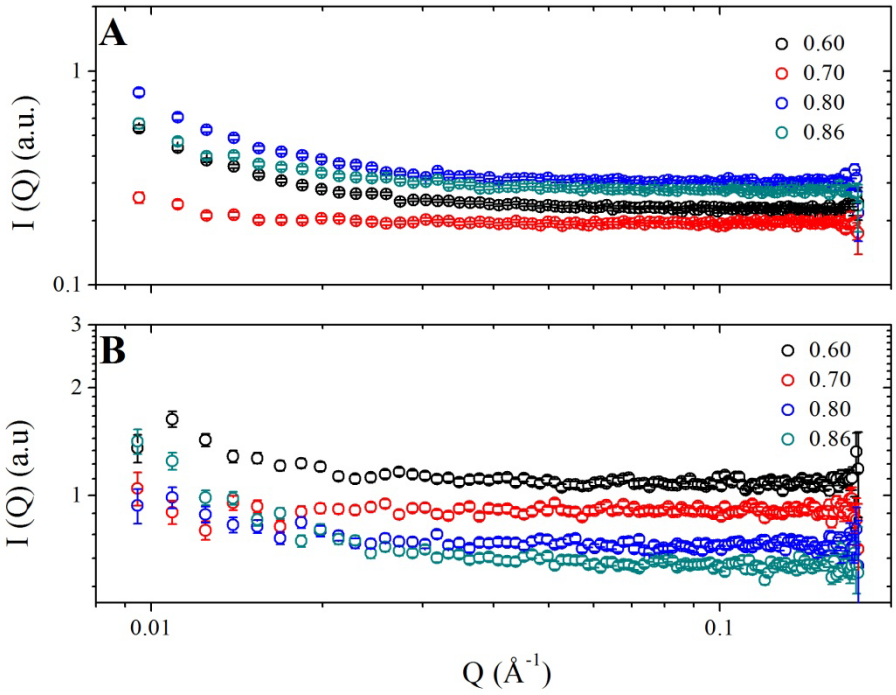

FIGURE 3.28. Semilogarithmic SANS spectra of undoped sol-gel matrix at different X_D. In panel **A** are reported the spectra of sol-gel matrices prepared in cuvette of 1 mm thickness. In panel **B** are reported the spectra of sol-gel matrices prepared in cuvette of 2 mm thickness.

The optimum X_D was calculated by plotting the square root of the scattering cross sections extrapolated at Q=0 (I(0)) for each SANS spectra. An expected linear trend as a function of X_D was observed (**Fig. 3.29**). The value for the sol-gel contrast match point results for X_D= 0.673 using cuvettes of 1 mm thickness and for X_D=0.720 using cuvettes of 2 mm thickness. Best results have been obtained for samples with 2 mm thickness (R^2=0.99), probably because they allow a better exchange between gel and embedding solution.

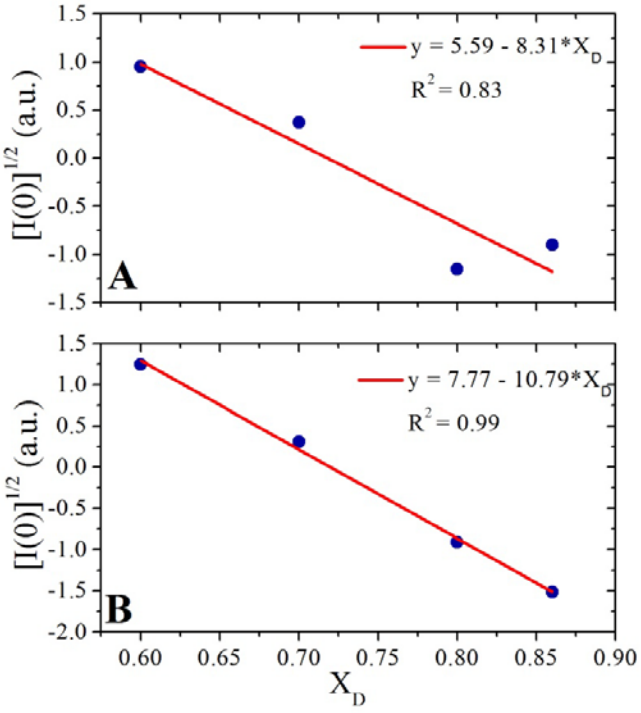

FIGURE 3.29. $[I(0)]^{1/2}$ as a function of X_D (**A**: 1mm thickness; **B**: 2mm thickness). In red is reported the linear fit of the four points.

According to the results obtained for undoped silica matrix, we performed SANS measurements on hemocyanin (~5mg/ml) entrapped into sol-gel matrix at the optimum deuteration grade of 0.720, using cuvettes of 2 mm thickness. SANS spectra were collected for hemocyanin entrapped both in presence and absence of oxygen, and in oxygenated and deoxygenated conditions (**Fig. 3.30A**). To simplify the understanding of the different experimental conditions, the four spectra conditions are visually indicated by arrows in the "three state" Hill-plot at pH 7.8, reported in **Fig. 3.30B**. The scattering signals from the different oxy- and deoxygenated conformers are nearly identical at $Q > 0.04$ Å^{-1}, while differ at $Q < 0.04$ Å^{-1}. In this Q region two of the four collected spectra, represented in *black* and *grey*, are characterized by very similar scatter profiles. No similarities were found among the other two spectra (in *red* and *green*). These results confirm the presence of three distinct conformers (R-state, S-state and T-state), in agreement with the functional results. Moreover, at the lowest Q-values there is a negative correlation between the intensity of the scatter signals and the oxygen affinity of

the conformers. Indeed, higher intensities are observed in the conformers characterized by lower oxygen affinities (S- and T-states) compared to the fully oxygenated R-state conformer.

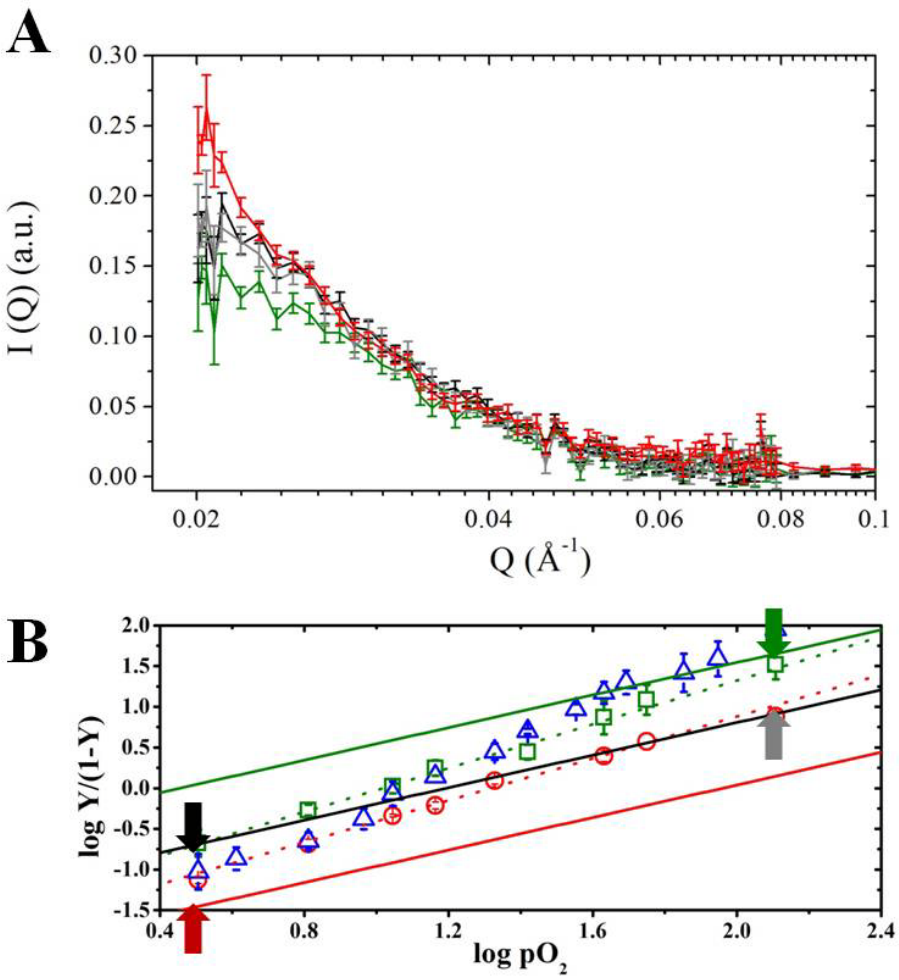

FIGURE 3.30. Semilogarithmic SANS patterns curves of C. *aestuarii* hemocyanin entrapped in presence or absence of oxygen, in oxygenated and deoxygenated conditions (**A**). For sake of clarity, the conditions at which the spectra were collected are indicated by arrows in the "three state" Hill-plot at pH 7.8 (**B**). *Red arrow*: T-state deoxygenated; *black arrow*: S-state deoxygenated; *grey arrow*: S-state oxygenated; *green arrow*: R-state oxygenated.

From the scattering curves, it is possible to deduce the structures of the entrapped conformers in terms of the most probable structure best fitted with SANS data. The four SANS spectra were analyzed by the new QUAFIT method (Spinozzi & Beltramini, 2012), which has been already tested by studying the structure of the molluscan hemocyanin of *Octopus vulgaris* (Spinozzi et al., 2012). The fitting

procedure resulted in 2 x 6-meric hemocyanin structures characterized by different arrangements of the two hexamers, in terms of rotational orientation (α, β, γ) and distance between them (*d*). α, β, γ correspond to the degrees of rotation of one hexamer with respect to the other one along the z-, x- and y-axis respectively. Representative fits and structures of the different conformers obtained by the QUAFIT analysis are shown in **Fig. 3.31**.

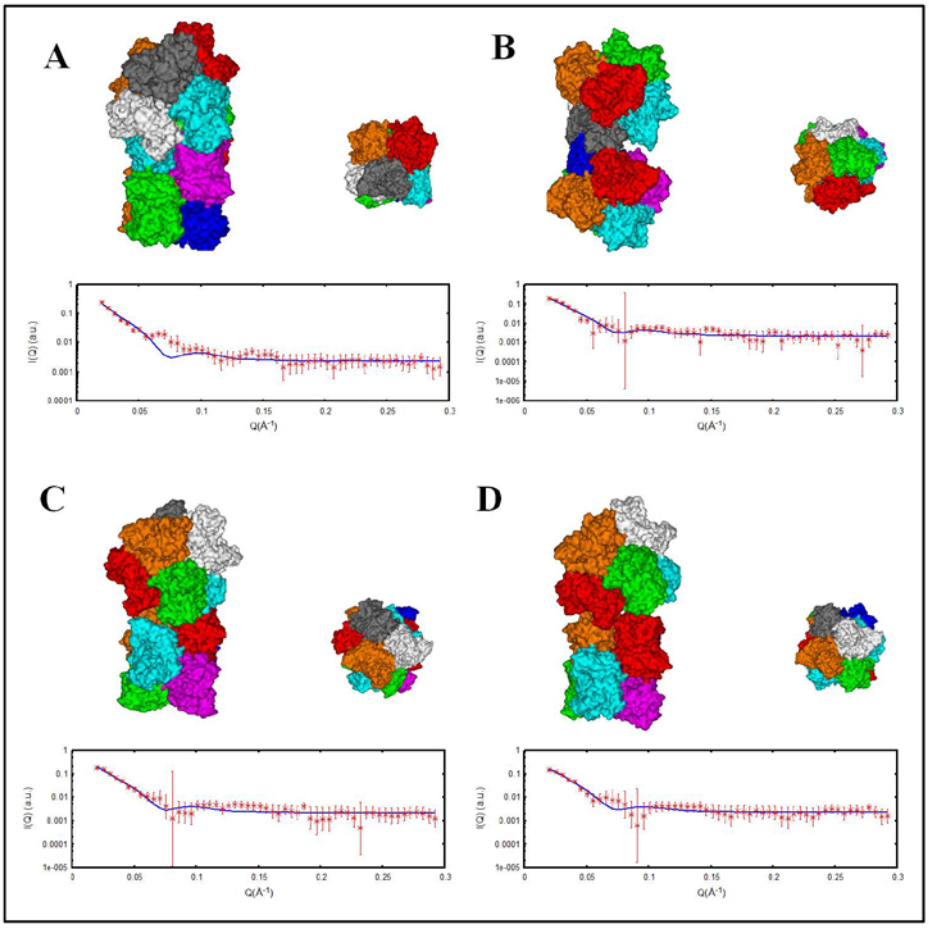

FIGURE 3.31. Representative QUAFIT analysis of the SANS spectra. The fits of the curves and the reconstructed models of the curves of the R-conformer in presence of oxygen (**A:** 17th fit), the S-conformer either in presence (**B:** 4th fit) and absence of oxygen (**C:** 4th fit) and the T-conformer in absence of oxygen (**D:** 6th fit) are indicated.

For a more consistent analysis each spectra was analyzed by repeating twenty times the fitting procedure (through a Montecarlo approach), resulting in twenty independent fits for each condition. The fitted parameters for all the fits are

reported in the **Supplementary materials**. From these sets of data, mean values of the fitted parameters and their standard deviation were calculated (**Table 3.5**).

	χ^2	α	β	γ	d
R-state OXY	0.27±0.04	237±65	114±29	134±70	106±8
S-state DEOXY	0.36±0.06	257±42	97±48	188±88	107±7
S-state OXY	0.44±0.12	270±56	120±40	147±85	109±12
T-state DEOXY	0.69±0.13	267±72	82±29	241±66	118±10

TABLE 3.5. Fitting parameters of the SANS curves of the different conformers. $\chi^2$is the goodness-of-fit value. α, β and γ (mean values after twenty fits ± standard deviation) are the degrees of rotation of one hexamer with respect to the other around the three axis (z, x, y) ; *d* is the interhexameric distance in Angstroms.

The first observation is that the fits of hemocyanin entrapped in absence of oxygen (S-state oxygenated: 0.44±0.12; T-state deoxygenated: 0.69±0.13) are characterized by higher and more variable χ^2 compared to the ones of S-state (0.36±0.06) and R-state oxygenated (0.27±0.04). Considering that χ^2 is a measure for the deviation between the model and the experimental data, we could suggest better fits for R-state oxygenated and S-state oxygenated spectra. However, it is important to take into account that the χ^2 of the fits strongly depend on the intrinsic noise of the experimental data.

To investigate if there are structural differences between the four experimental conditions we performed a 1-way ANOVA analysis, coupled with the Fisher Post-Hoc test, in order to compare the pair wise differences in the fitted parameters values between the different conformers. A Kruskal-Wallis and Mann-Whitney analysis was performed when the assumption of homogeneity of variances was not satisfied. From these analysis no significant differences have been evidenced for α and β, while there are differences in the rotation of the hexamers against each other along the y-axis ($p<0.001$) and in the distance *d* between the two hexamers ($p<0.001$). As summarized in **Table 3.6**, the quaternary structure of the

T-state in absence of oxygen is characterized by significantly higher γ (241±66) and *d* (118±10) compared to all the other conformers. A significantly different rotation along the y-axis of one hexamer with respect to the other one is also evidenced from the comparison between the R-state oxygenated and the S-state deoxygenated.

	R-OXY	S-DEOXY	S-OXY	T-DEOXY
R-OXY		*γ*		*γ-d*
S-DEOXY	*γ*			*γ-d*
S-OXY				*γ-d*
T-DEOXY	*γ-d*	*γ-d*	*γ-d*	

TABLE 3.6. Results from the Fisher Post-Hoc test. Significant differences between the different couples of data are indicated with the name of the fitted parameter.

Therefore, this preliminary analysis of the SANS spectra seems to confirm the three-state model previously described, with no structural differences between the S-state in oxygenated and deoxygenated condition. However the high variability of the fitted parameters *α, β, γ* and *d* makes difficult a fine analysis of the structural differences between the different conformers. A possible strategy to improve these results may be the generation of more model structures, through several runs of the program, selecting only the subset of models for each spectra with χ^2 values not more higher than a defined % (ex. 30%) from the lowest χ^2 reached in the whole simulation. A similar approach has been adopted by Hartmann & Decker (2002) for the structural characterization of the 4 x 6-meric *E. californicum* hemocyanin in solution.

3.7.3 Copper k-edge spectra of R-, S- and T-conformer of hemocyanin in sol-gel matrix

To determine if the changes of the oxygen affinity are due to a different coordination geometry of the active site, we collected X-ray absorption spectra for R-, S- and T-conformers in presence and absence of oxygen. Coordination geometry of copper in the active site of hemocyanin in solution have been already evaluated by X-ray absorption spectroscopy XAS (Hirota et al., 2008), showing

distinct signatures in the X-ray absorption spectra of the oxygenated and the deoxygenated form.

XAS measurements of hemocyanin embedded into the sol-gel matrix display the typical line shape described for hemocyanin in solution (**Fig. 3.32**; **Fig. 3.33**). In particular the difference spectra between deoxy- and oxy-hemocyanin evidence two main absorbance peaks at ~ 8982 eV and ~ 8985 eV, which has been assigned to the 1s → $4p_z$ and 1s → (s+p)* transitions, respectively (Blackburn et al., 1989; Brown et al., 1980). The spectra of hemocyanin trapped in R- and S-states recorded in presence of oxygen did not show significant differences in the XANES region (**Fig. 3.32**). In contrast, in deoxygenated condition the spectra of the T- and S-states are characterized by different intensities of the transitions 1s → $4p_z$ and 1s → (s+p)* (**Fig. 3.33**), that can be correlated to the displacement of Cu(I) from the plane defined by the three His. The lower intensity of the 8982eV band of the conformer T suggests a greater degree of distortion toward pseudotetrahedral geometry than the active site of S-conformer.

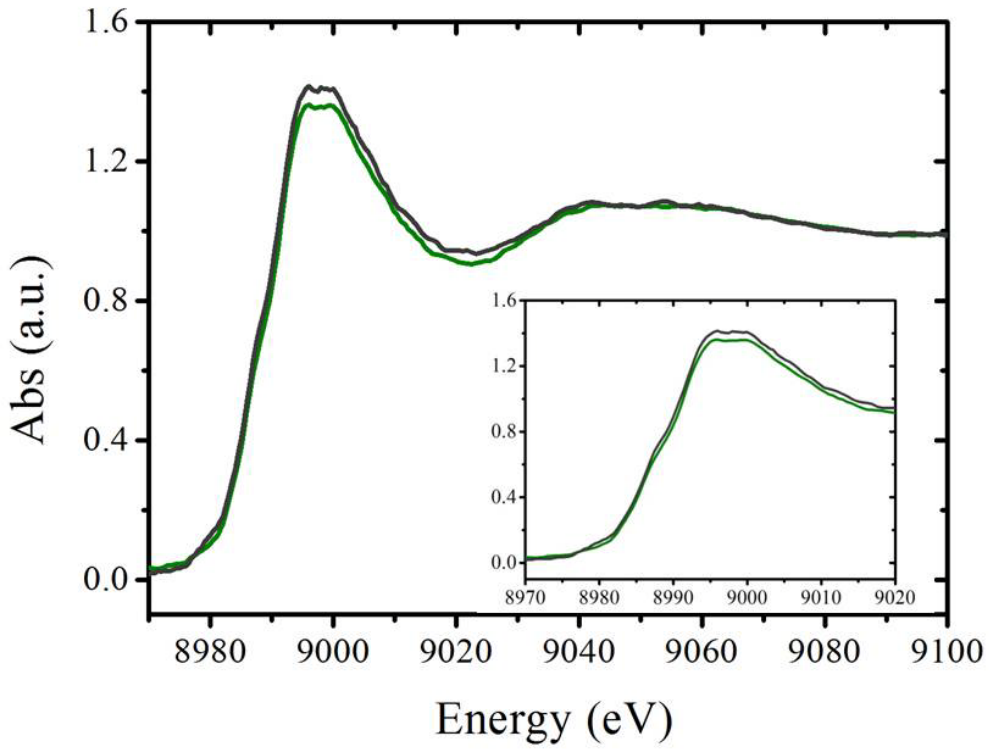

FIGURE 3.32. X-ray absorption spectra of R- (in *green*) and S-conformer (in *gray*) in presence of oxygen at pH 7.8.

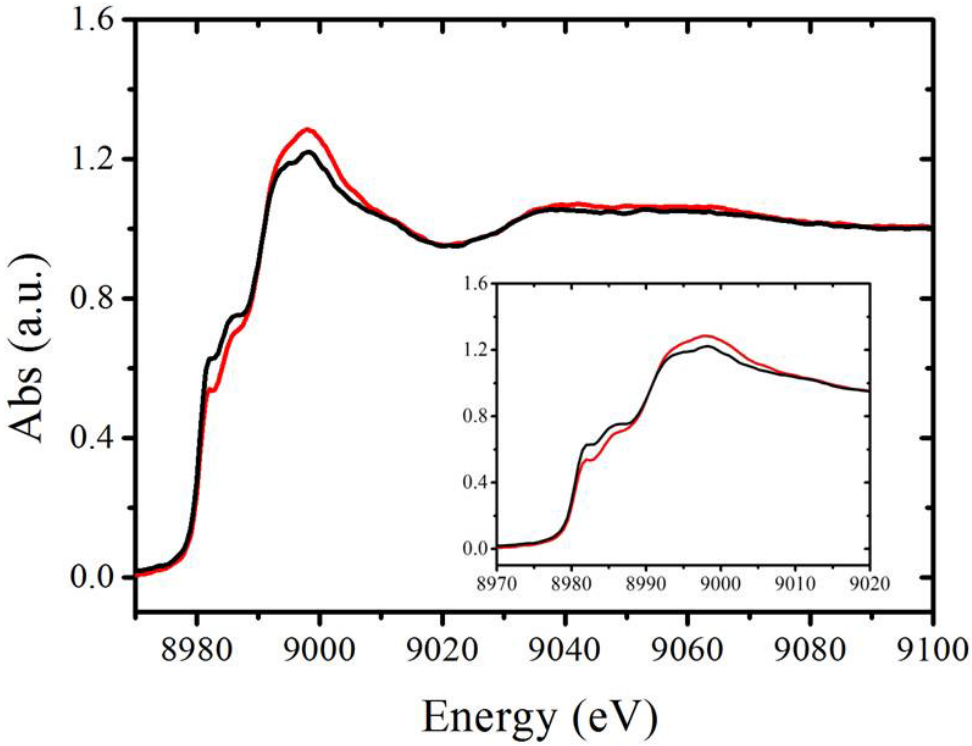

FIGURE 3.33. X-ray absorption spectra of S- (in *black*) and T-conformer (in *red)* in absence of oxygen at pH 7.8.

3.8 Effect of L-lactate

3.8.1 Effects of lactate on the functional properties of the entrapped conformers.

The role of lactate in the oxygen-binding behavior of *C. aestuarii* hemocyanin were determined through oxygen binding curves of hemocyanin in solution and entrapped into the sol-gel matrix, collected in the presence of 40mM lactate (**Fig. 3.34**). **Fig. 3.35A** shows Hill-plot of hemocyanin in solution and embedded into the matrix with and without lactate at pH 6.5. Oxygen binding parameters are reported in **Table 3.7**.

		p50 (torr)	n
0 mM Lactate	***Solution***	74.80±2.37	2.48±0.17
	S-state	43.92±2.20	0.90±0.06
	T-state	736.42	0.82
40 mM Lactate	***Solution***	22.03±2.05	1.34±0.07
	S^L-state	9.37±1.73	0.87±0.06
	T^L-state	22.48±5.89	0.86±0.06

TABLE 3.7. Oxygen binding properties of hemocyanin in solution and embedded into sol-gel matrix, in presence and absence of 40mM Lactate at pH 6.5. Average and standard deviation resulting from 3 replicas. The average of 2 replicas is reported for the T-state in absence of lactate.

	K_R ($torr^{-1}$)	K_S ($torr^{-1}$)	K_T ($torr^{-1}$)
Solution	0.166	0.034	0.002
S-state	-	0.022±0.000	-
T-state	-	-	0.001
S^L-state	-	0.110±0.020	-
T^L-state	-	-	0.046±0.011

TABLE 3.8. Oxygen binding constants of hemocyanin in solution and embedded into sol-gel matrix, in presence and absence of 40mM lactate at pH 6.5. K_R, K_S and K_T are calculated according to the three-state MWC model described for protein in solution. Average and standard error resulting from 3 replicas. The average of 2 replicas is reported for the T-state in absence of lactate.

	Log L_S	**Log L_T**
Solution	10.32	13.06
Solution^L	3.22	-28.16

TABLE 3.9. Allosteric equilibrium constants of hemocyanin in solution obtained by the three-state model, in presence and absence of 40mM lactate at pH 6.5.

At pH 6.5 the cooperativity index *n* of S- and T-conformers in presence of lactate are not significantly higher than 1 ($p>0.05$, **Table 3.7**); these results confirm that sol-gel embedding is suitable to block the two conformers also in the presence of lactate. Furthermore, oxygen affinity of hemocyanin entrapped into the matrix, both in S- and T-state, was increased by the presence of 40mM lactate: p50 shifts from 43.92±2.20 to 9.37±1.73 torr for S-conformer and from 736.42±16.95 to 22.48±5.89 torr for T-conformer. Interesting, the equilibrium constants K_S^L=0.110±0.020 torr^{-1} is closer to the K_R of the hemocyanin in solution without lactate (0.166 torr^{-1}). Thus, we could suppose that the S-conformer in presence of lactate corresponds to the R-state of the protein in solution, with the lactate that forces the allosteric transition from the S- to the R-conformer, confirming the presence of three distinct conformers also at pH 6.5 (**Fig. 3.35B**). The entrapment of the S-state and not of the R-state when the samples were prepared in absence of lactate, could be explained as a constraint effect of the matrix that unfavours the R-state entrapment. Moreover the constant of the T-state in presence of lactate K_T^L(0.046±0.011 torr^{-1}; **Table 3.8**) is very similar to the equilibrium constant K_S of the S-state without lactate (0.022±0.000torr^{-1}; **Table 3.8**). We can not actually demonstrate that R-state without lactate and T-state with lactate represent the same conformational state, but this may be an indication of the mechanism at which the lactate modulate the oxygen affinity of the protein in solution. A fine regulation of the two allosteric equilibriums between the T- and R-states and the S- and R-state could be at the basis of the different oxygen affinity observed at different concentrations of lactate (Weeber et al., 2008).

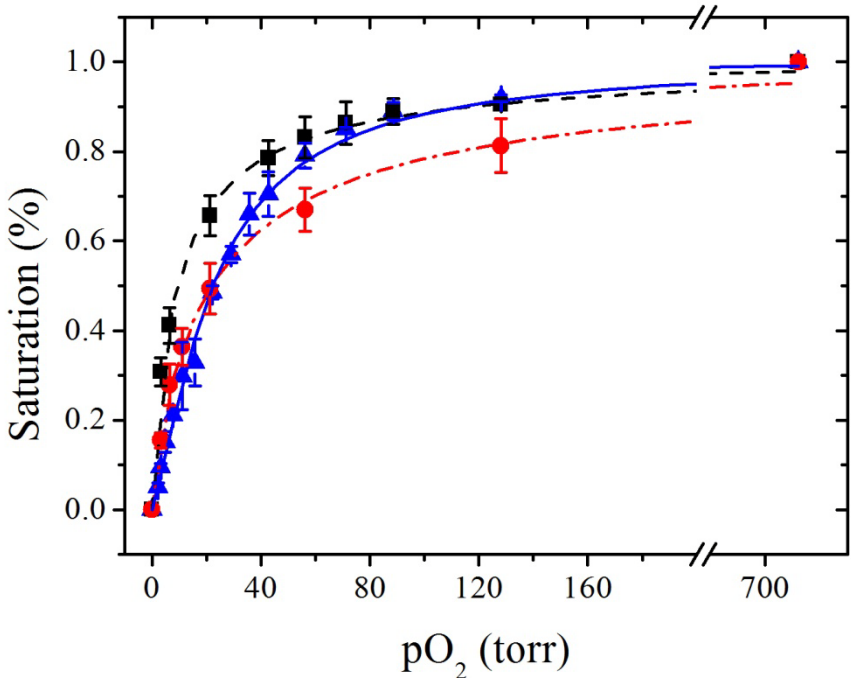

FIGURE 3.34. Oxygen binding curves of hemocyanin in solution (in *blue*), entrapped in T-state (in *red*) and in S-state (in *black*) at pH 6.5 in presence of 40mM lactate. Solid, dotted and dash-dotted lines represent respectively the best fits of the points for the hemocyanin in solution, entrapped in S-state and T-state. Average and standard deviation resulting from 3 replicas.

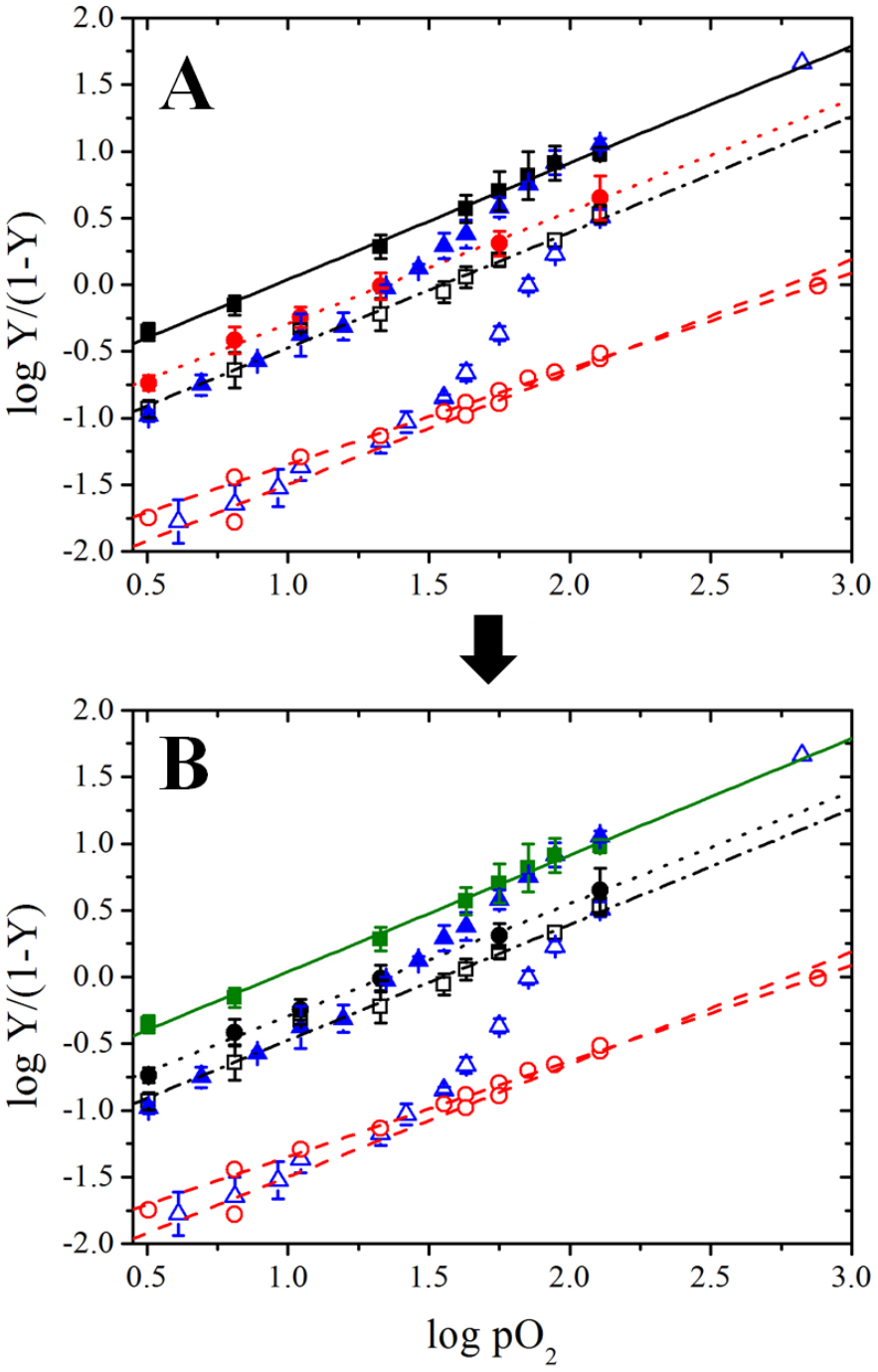

FIGURE 3.35. A. Hill plot of hemocyanin in solution (in *blue*) and embedded into the T- (in *green*) and S-state (in *black*). The measurers were performed both in presence (*solid symbols*) and absence (*empty symbols*) of 40mM lactate. **B.** Alternative representation of the Hill-plot described in **A**. In *red* is indicated the T-state while in *black* and *green* the supposed S- and R-state, respectively. Average and standard deviation resulting from 3 replicas. 2 replicas for the T-state are shown.

The characterization of functional properties of the hemocyanin embedded into the sol-gel matrix in presence of lactate was extended also to pH 7.8. However an high variability was observed, probably because our gas mixing system is not reliable enough to work in the range of the very low oxygen partial pressures that is to be explored when hemocyanin is under very high affinity conditions. A possible perturbing effect of lactate at this pH was also considered. A representative Hill-plot in presence of lactate is shown in **Fig. 3.36**. Despite the quality of the data, lactate seems to translate the lower pO_2 region of the linear fits towards higher values of log Y\(1-Y), without affecting the fully oxygenated region.

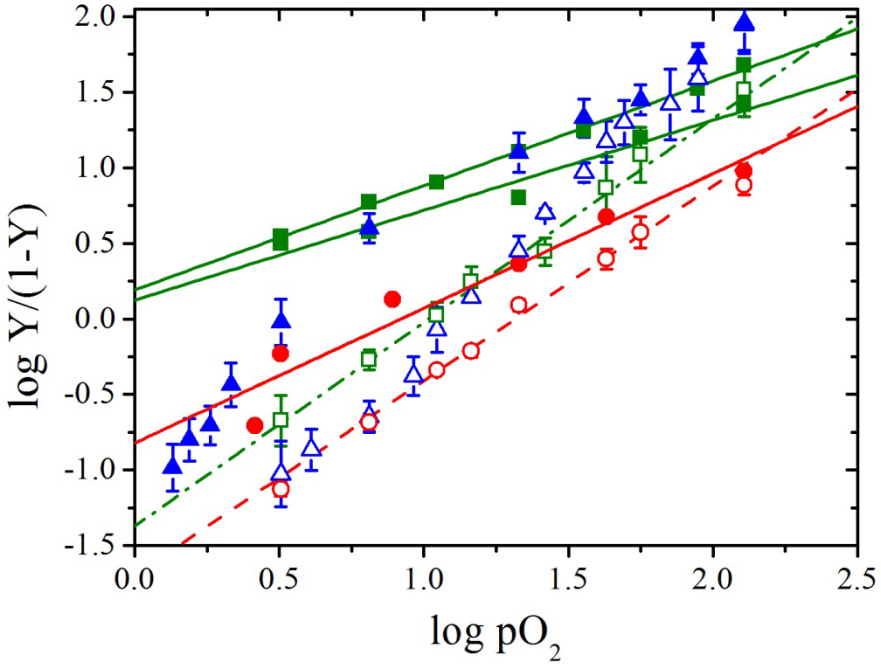

FIGURE 3.36. Hill plot of hemocyanin in solution (in *blue*) and embedded into the matrix in presence (in *green*) and absence of oxygen (in *red*) at pH 7.8. The measurements were performed both in presence (*solid symbols*) and absence (*empty symbols*) of 40mM lactate. 2 replicas for the protein entrapped in presence of oxygen are shown, in order to appreciate the variability of the measures at this experimental condition.

3.8.2 Structural effects induced by the binding of lactate

To determine the structural effect of lactate on the quaternary structure of the different conformers, SANS spectra of R-state in presence of oxygen, S-state both in presence and absence of oxygen and T-state fully deoxygenated were collected in presence of 40mM of lactate. The samples were prepared at the same X_D of the SANS measurements described in **paragraph 3.7.2**. All the measurements were performed at physiological pH 7.8 although the functional properties in presence of lactate were not as well described as at pH 6.5. In **Fig. 3.37** the SANS spectra of the different conformers are reported. S-state deoxygenated in presence of 40mM of lactate shows a scattering profile very different from the other spectra at Q <0.04 $Å^{-1}$. S- and R-state oxygenated spectra are almost superimposable, while small differences between these two conformers and the T-state deoxygenated are evidenced.

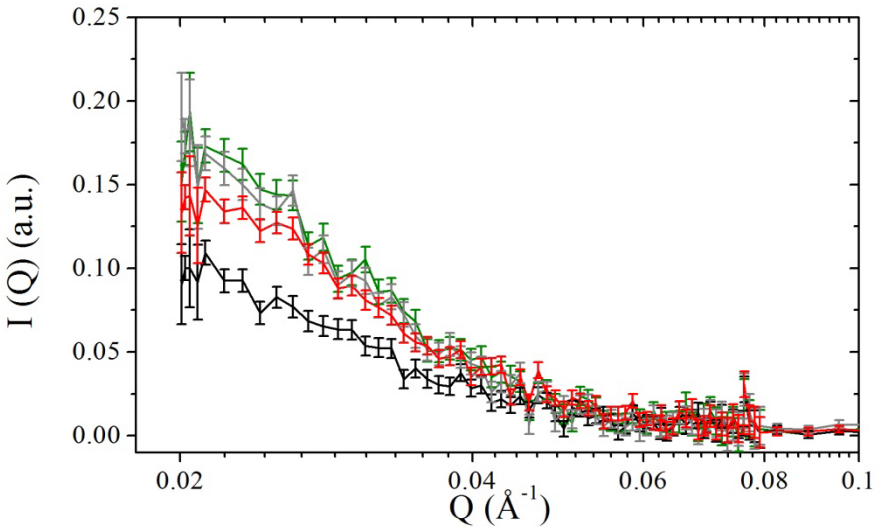

FIGURE 3.37. SANS patterns of different hemocyanin conformers in the presence of 40 mM lactate at pH 7.8. R-conformer in presence of oxygen (in *green*), S-conformer both in presence (in *gray*) and absence (in *black*) of oxygen and T-conformer fully deoxygenated (in *red*).

Representative fits and structures of the conformers in presence of lactate are shown in **Fig. 3.38.** The twenty fits for each SANS curve in presence of lactate are represented in the **Supplementary materials.**

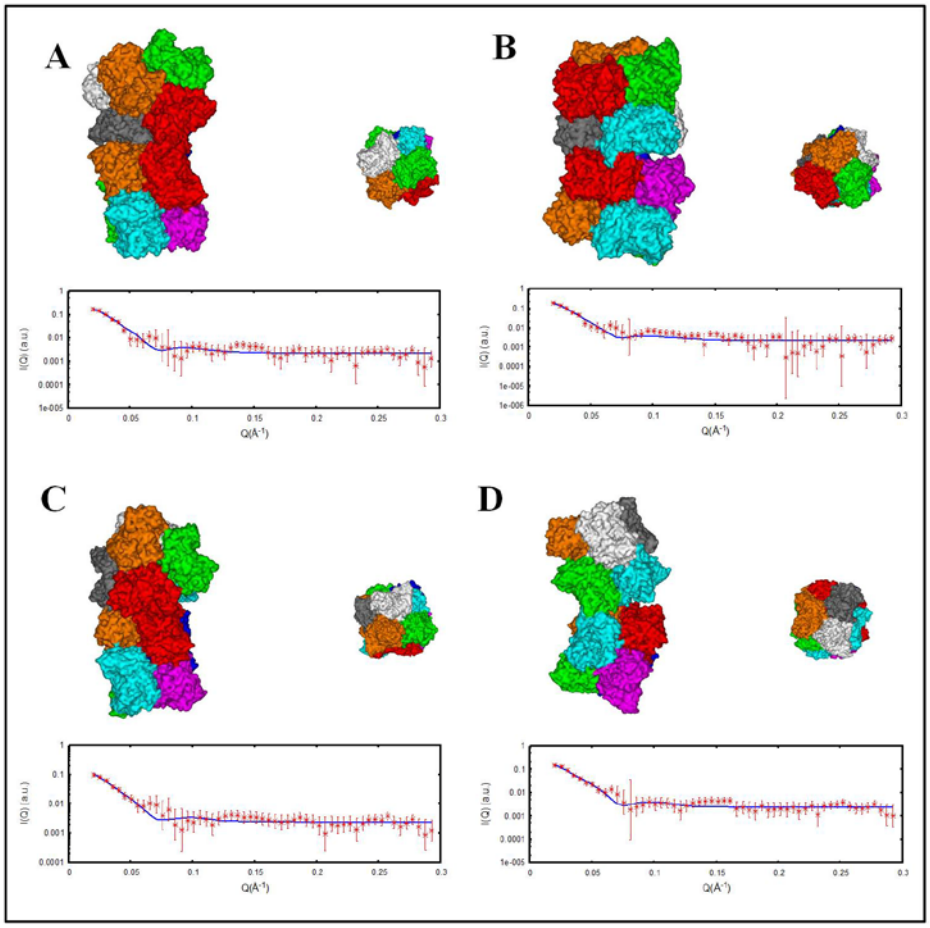

FIGURE 3.38. QUAFIT analysis of the SANS spectra of hemocyanin in presence of 40mM lactate. The fits of the curves and the reconstructed models of the R-conformer in presence of oxygen (**A:** 14th fit), the S-conformer either in presence (**B:** 2nd fit) and absence of oxygen (**C:** 5th fit) and the T-conformer in absence of oxygen (**D:** 2nd fit) are indicated.

In the same way of SANS analysis in absence of lactate (**Chapter 3.7.2**), the means of the fitted parameters (**Table 3.10**) obtained by the QUAFIT program were compared in order to identify structural differences between the conformers in presence of lactate.

	χ^2	α	β	γ	d
R-state OXY L	0.41±0.07	258±75	51±31	250±46	103±8
S-state DEOXY L	0.23±0.01	294±23	97±48	285±50	105±7
S-state OXY L	0.46±0.07	256±53	84±52	172±99	107±9
T-state DEOXY L	0.38±0.04	158±84	88±32	164±61	115±8

TABLE 3.10. Fitting parameters of the SANS curves of the different conformers. $\chi^2$is the goodness-of-fit value. α, β and γ (mean values after twenty fits ± standard deviation) are the degrees of rotation of one hexamer with respect to the other along the three axis (z, x, y); d is the interhexameric distance.

The statistical analysis has evidenced significant differences for all the parameters (α: $p<0.05$; β: $p<0.01$; γ: $p<0.001$; *d:* $p<0.001$), suggesting a different structural effect of lactate on the arrangement of the two hexamers. In particular in presence of lactate the structure of the T-conformer fully deoxygenated is strongly different from all the other conformers, with a significantly higher distance between the two hexamers (d=115±8Å) compared to all the others. Moreover, significantly lower rotational degrees around the *x* (β=88±32) and *y* (γ =164±61) axis have been evidenced from the comparison with the R- and S- states oxygenated. A significantly lower α (158±84) parameter than the S-state deoxygenated (α =294±23) is also evidenced. Contrary to the T-state fully deoxygenated, the other conformers differs only in the rotational angle γ. In **Table 3.11** all the significant differences between the conformers in presence of lactate are summarized.

	R-OXYL	S-DEOXYL	S-OXYL	T-DEOXYL
R-OXYL		$\underline{\gamma}$	$\underline{\gamma}$	$\underline{\beta}$ - $\underline{\gamma}$ - d
S-DEOXYL	$\underline{\gamma}$		$\underline{\gamma}$	$\underline{\alpha}$ - d
S-OXYL	$\underline{\gamma}$	$\underline{\gamma}$		$\underline{\beta}$ - $\underline{\gamma}$ - d
T-DEOXYL	$\underline{\beta}$ - $\underline{\gamma}$ - d	$\underline{\alpha}$ - d	$\underline{\beta}$ - $\underline{\gamma}$ - d	

TABLE 3.11. Results from the Fisher and Mann-Whitney Post-Hoc test. Significant differences between the different couples of data are indicated with the name of the fitted parameter (underlined for Mann-Whitney Post-Hoc test).

Despite the significantly different angles of rotation α, β and γ observed for the conformers in presence of lactate, the key result of this analysis is the significantly lower interhexameric distance of the fully deoxygenated T-conformer as compared with the others conformers. This result has been obtained also with the analysis performed in absence of lactate, suggesting a correlation between the distance *d* and the oxygen affinity of hemocyanin. Considering that the binding of lactate increase the oxygen affinity of hemocyanin, it could be interesting to compare the interhexameric distance of the different conformers in presence and absence of lactate, in order to identify any significant trends. Previous SAXS experiments performed on *C. aestuarii* hemocyanin in solution and in presence of oxygen have already evidenced that the binding of lactate affects the distance of the two hexamers, with differences of ~1 Å (Hirota et al. 2010). However there are not information about the structural effects induced by the binding of lactate on the fully deoxygenated hemocyanin. As shown in **Table 3.12**, all the conformers are characterized by a decrease of the distance *d* of about 2-3Å in presence of lactate, although at the present degree of refinement of SANS data fitting the differences (no lactate *versus* lactate) are not statistically significant ($p>0.05$). Increasing the number of fits may improve the these very small differences as significant.

	Lactate	*d*
R-OXY	0mM	106±8
	40mM	103±8
S-DEOXY	0mM	107±7
	40mM	105±7
S-OXY	0mM	109±12
	40mM	107±9
T-DEOXY	0mM	118±10
	40mM	115±8

TABLE 3.12. Interhexameric distance *d* of the different conformers, both in presence and absence of lactate (mean values ± standard deviation)

3.9 Investigation of a possible structural allosteric mechanism of hemocyanin through a 2^3 factorial design analysis of the structural data.

In **Chapters 3.7.2** and **3.8.2**, we have characterized the structures of the conformers at different experimental conditions (oxygen and lactate concentration). However, the comparison of the results obtained through a separate analysis of the single elements restricts the possibility to detect an overall structural mechanism for oxygen affinity modulation in hemocyanin. For this reason a 2^3 factorial analysis of all the fitted parameters have been performed. In this analysis, the effects of the conformational state, oxygen concentration and presence or not of lactate are evaluated. These three variables are considered as the independent factors of the factorial design, and each one occurs at only two levels (or versions). The advantage of this statistical approach is that it allows to quantify the magnitude of the effects of the single factors (*main effects*), determining also if there are interactions between the factors considered (*two-factor* and *three-factor interaction effects*). For the *oxygenation factor* (O) the two levels are represented by the fully oxygenated and the fully deoxygenated hemocyanin. The *lactate factor* (L) includes the concentrations values of 0mM and 40mM. In the case of the *conformation factor* (C) the functional and structural results indicate the presence of three conformers, but only two levels are required

for the analysis. Therefore we consider as two levels the conformers obtained by the entrapment of hemocyanin in absence of oxygen (a mix of S- and R-conformers) and the ones blocked in presence of oxygen (a mix of S- and T-conformers). This is a simplification of the situation previously described, but at this stage of investigation it can be considered a reasonable compromise. All the levels of the three factors, coded by minus and plus signs, as represented in **Table 3.13**.

FACTORS			
		-	+
Oxygenation	**O**	deoxy	oxy
Lactate	**L**	0 mM	40 mM
Conformation	**C**	low	high

TABLE 3.13. Factors considered in the 2^3 factorial design. The two levels (- and +) for each factor are also indicated

The effects of the three factors have been determined for all the fitted parameters, *α, β, γ* (degrees) and *d* , through four distinct factorial analysis. A display of the levels to be run is given in the design matrix shown in **Table 3.14**. For each parameter the mean of twenty replicas at the experimental conditions defined by the combination of three signs (e.g. - - +) is indicated. From the variances S_i^2 of the different means, the pooled estimated of run variance S^2, the variance V(effect) and the standard error of the effects have been estimated for each fitted parameter (**Table 3.15**). The standard error of the each effect have been considered to check the significance of the calculated effect.

O	**L**	**C**	***α***	$\mathbf{S_i^2}$	***β***	$\mathbf{S_i^2}$	***γ***	$\mathbf{S_i^2}$	***d***	$\mathbf{S_i^2}$
-	-	-	266	5126	87	1028	241	4409	117	96
-	-	+	256	1724	96	2301	188	7667	106	55
-	+	-	225	7133	82	830	157	3671	114	70
-	+	+	293	543	83	1167	285	2495	104	51
+	-	-	269	3163	83	2707	147	8050	109	153
+	-	+	236	4274	50	959	134	4882	105	61
+	+	-	255	2822	119	1592	171	9973	106	82
+	+	+	258	5587	114	817	249	2089	102	71

TABLE 3.14. Design matrix of the 2^3 factorial design for *α, β, γ* (degrees) and *d* (Å). S_i^2 is the variance of the 20 replicas for each condition.

	S^2	V(effect)	st.err
α	3797.02	94.93	9.74
β	1425.73	35.64	5.97
γ	945.67	23.64	4.86
d	80.45	2.01	1.42

TABLE 3.15. S^2, V(effect) and standard error of the effects are reported for each structural parameter.

The results of the factorial designs, summarized in **Fig. 3.39**, show significant effects of the three factors on the structural properties of hemocyanin. The interpretation of these results have been discussed taking into account that the main effect of a factor should be individually interpreted only if there are no interactions with the other factors. Indeed, when an interaction effect is evidenced the two interacting factors should be considered jointly (Box et al., 1978).

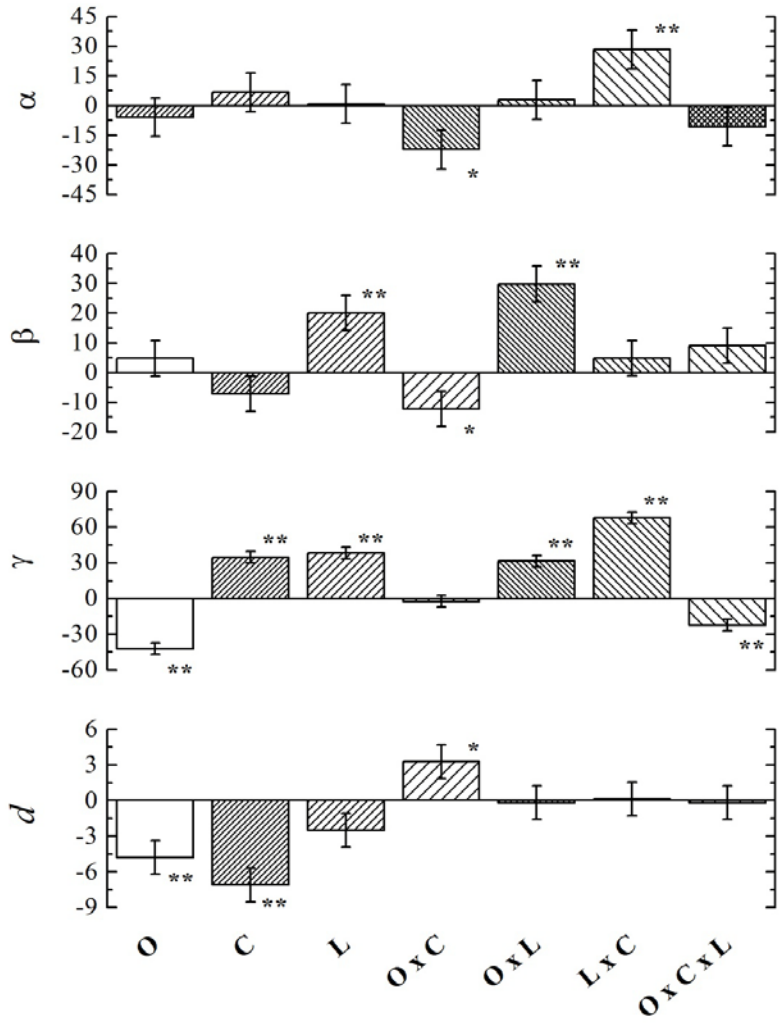

FIGURE 3.39. Main effects (O, C and L), two-factor interaction effects (O x C, O x L and L x C) and three-factor interaction effect (O x C x L) for α, β, γ and d are represented. * $p<0.05$; ** $p<0.001$.

In the case of the rotational angle α two significant interaction effects have been recognized: the L x C interaction ($p<0.05$) and the O x C interaction ($p<0.001$) (**Table 3.16**). These two interactions can best be considered using the two-way table shown in **Fig. 3.40A.** In both the cases, the increase or decrease effect of one of the two interacting factor on the angle α depends on the level of the other one. More in detail a decrease of α is observed when the conformation of the hemocyanin changes from a lower to an higher oxygen affinity state in absence lactate, while in presence of lactate this allosteric transition involves an increase of the rotational angle around the z-axis. The binding of lactate to low or high oxygen affinity conformers causes a decrease or increase of the angle α, respectively. On the contrary, the effects of the interaction between the conformation and the oxygen concentration are perfectly opposite to those previously described.

Effects	**Estimate ± standard error**	**Test t**	**Significance (v_i = 152)**
Main effects			
O	-5.90±9.74	-0.61	-
C	6.72±9.74	0.69	-
L	0.80±9.74	0.08	-
Two-factor interaction			
O x C	-22.29±9.74	-2.28	p<0.05
O x L	2.88±9.74	0.29	-
L x C	28.25±9.74	2.89	p<0.001
Three-factor interaction			
O x C x L	-10.77±9.74	-1.10	-

TABLE 3.16. Calculated effects and standard errors for the 2^3 factorial design of α parameter. t-tests have been performed to determine the significance of the effects.

The analysis of the effects of the three factors on the arrangement of the two hexamers in terms of β angle has evidenced a significant effect of lactate ($p<0.001$) and significant O x C ($p<0.05$) and O x L ($p<0.001$) interactions effects (**Table 3.17**). An increase of the rotational angle β due to the oxygenation of the hemocyanin is observed for both the low and high oxygen affinity states, with an higher effect in the case of the low affinity conformers. Moreover, the transition

toward higher oxygen affinity conformers implied a decrease of β in the case of hemocyanin fully oxygenated, while no significant differences are observed in absence of oxygen. The binding of lactate seems to differently affect this parameter, with an high increase of the angle in the case of fully oxygenated hemocyanin, and a small decrease in presence of deoxygenated condition (**Fig. 3.40B**).

Effects	**Estimate ± standard error**	**Test t**	**Significance (v_i = 152)**
Main effects			
O	4.79±5.97	0.80	-
C	-7.15±5.97	-1.20	-
L	20.06±5.97	3.36	p<0.001
Two-factor interaction			
O x C	-12.24±5.97	-2.05	p<0.05
O x L	29.78±5.97	4.99	p<0.001
L x C	4.87±5.97	0.82	-
Three-factor interaction			
O x C x L	9.08±5.97	1.52	-

TABLE 3.17. Calculated effects and standard errors for the 2^3 factorial design of β parameter. t-tests have been performed to determine the significance of the effects.

The results obtained by the analysis of the angle γ shows strong O x L and L x C interaction effects (p<0.001) (**Table 3.18**). In particular the binding of lactate increases this rotational angle in both the oxygenated and deoxygenated hemocyanin, with a strong effect in the first case. The oxygenation process instead results as a decrease of γ, with larger effect in absence of lactate (**Fig. 3.40C**). An increase of the angle instead seems to be at the basis of the transition from the low to the high oxygen affinity conformers. The effect of the binding of lactate to hemocyanin depends on the conformational state of the protein, with a decrease or an increase of the rotation in the case of the low and high oxygen affinity states, respectively. Also a three-factor interaction has been evidenced (p<0.001). In **Fig. 3.41** a 3D representation of the effects of this interaction is shown. However, an interpretation of this data is really complicated.

Effects	Estimate ± standard error	Test t	Significance (ν_i = 152)
Main effects			
O	-42.29±4.86	-8.70	p<0.001
C	34.71±4.86	7.14	p<0.001
L	38.47±4.86	7.91	p<0.001
Two-factor interaction			
O x C	-2.42±4.86	-0.49	-
O x L	31.61±4.86	6.50	p<0.001
L x C	68.03±4.86	13.99	p<0.001
Three-factor interaction			
O x C x L	-22.41±4.86	-4.61	p<0.001

TABLE 3.18. Calculated effects and standard errors for the 2^3 factorial design of γ parameter. t-tests have been performed to determine the significance of the effects.

Finally, the interhexameric distance *d* depends on the interaction effect between the oxygenation process and the conformation of hemocyanin (p<0.05) (**Table 3.19**). As represented in **Figure. 3.40D**, the distance between the two hexamers decreases during the allosteric transition towards higher oxygen affinity-states, both in presence and absence of oxygen. However, a stronger effect occurs in the case of deoxygenated conformers. A decrease of *d* is also observed after the binding of oxygen, with an high variation in the case of the low-oxygen affinity conformers.

Effects	Estimate ± standard error	Test t	Significance (ν_i = 152)
Main effects			
O	-4.80±1.41	-3.38	p<0.001
C	-7.11±1.41	-5.01	p<0.001
L	-2.52±1.41	-1.774	-
Two-factor interaction			
O x C	3.27±1.41	2.30	p<0.05
O x L	-0.18±1.41	-0.124	-
L x C	0.14±1.41	0.09	-
Three-factor interaction			
O x C x L	-0.19±1.41	-0.132	-

TABLE 3.19. Calculated effects and standard errors for the 2^3 factorial design of *d* parameter. t-tests have been performed to determine the significance of the effects.

The overall results here described must be considered only indicative due to the high variability of the mean values considered in the factorial design elaboration. However, this analysis suggests changes in the rotational arrangement of an hexamer compared to the other one during the allosteric transition from lower to higher oxygen affinity conformers, and after the binding of oxygen and lactate. The different distances between the two hexamers instead are more easy to interpret. Indeed, a decrease of the interhexameric distance is observed after the binding of oxygen and the after the allosteric transition towards higher oxygen affinity states. Considering also the decrease effect of lactate on this parameter (**Chapter 3.8.2**), it is reasonable to consider that smaller distances between the hexamers are correlated to higher oxygen affinities.

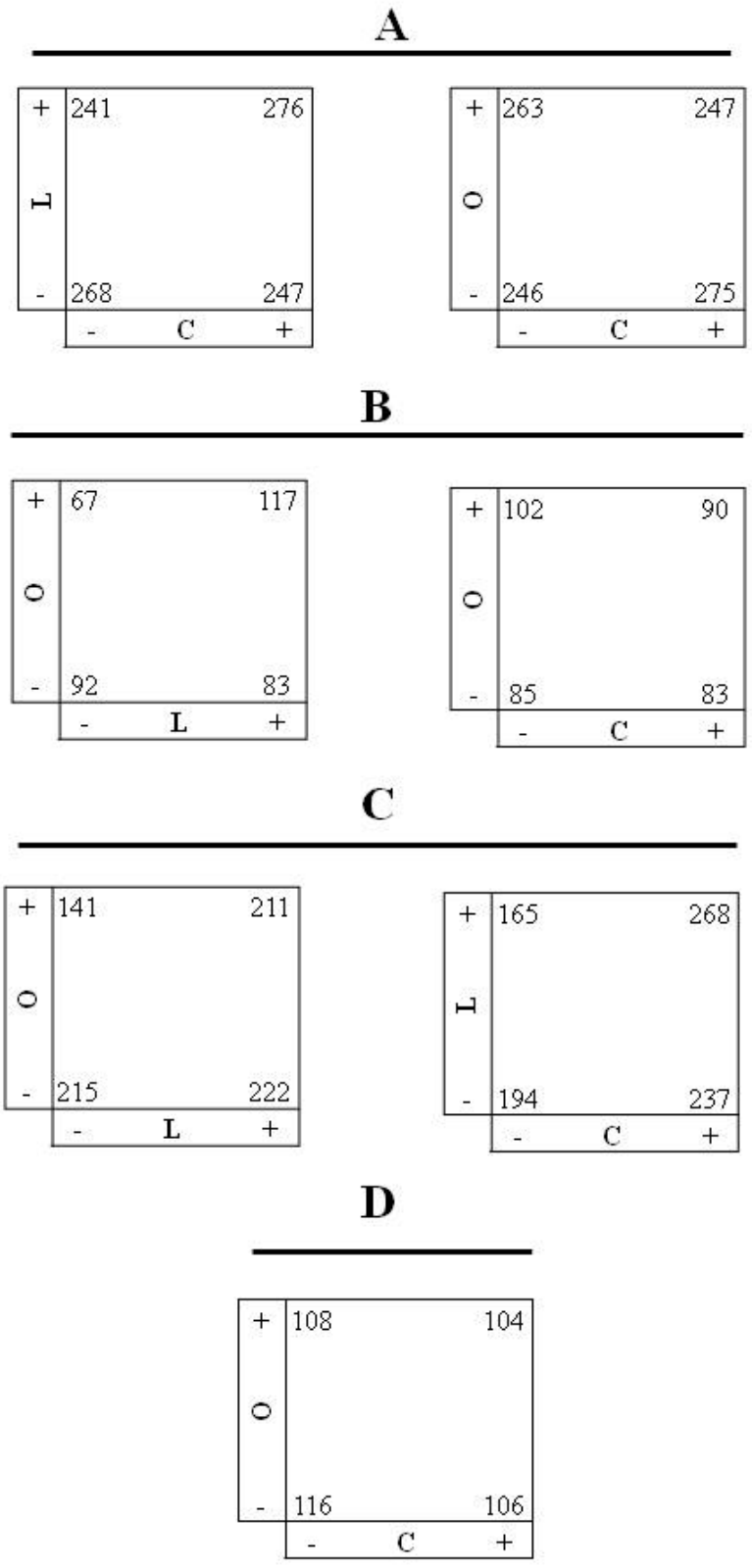

FIGURE 3.40. Two-way tables for the interpretation of the two-factor interactions. **A:** α; **B**: β; **C**: γ; **D**: *d*.

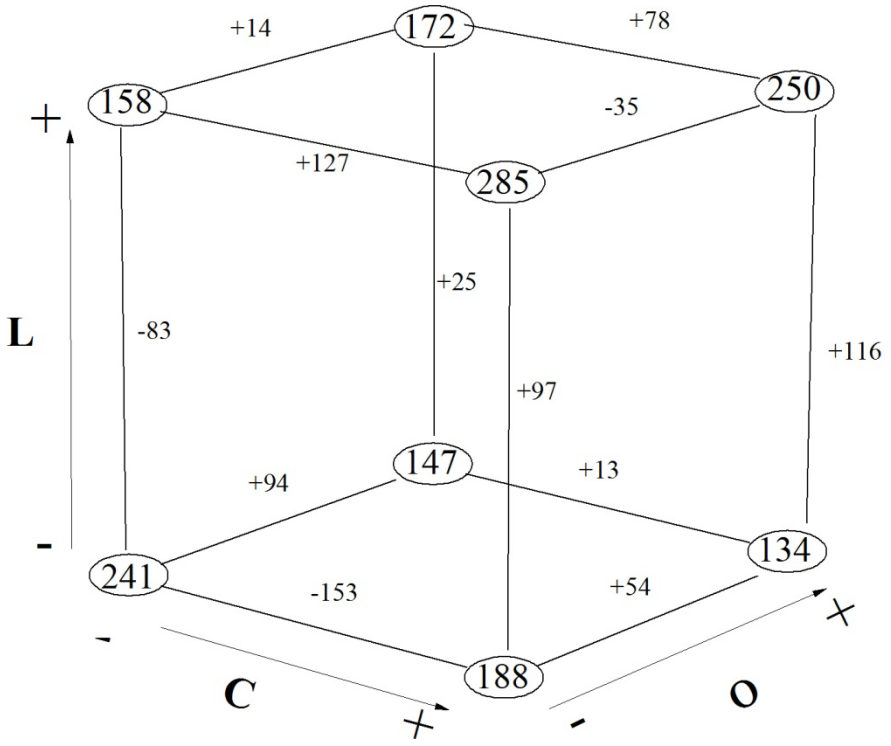

FIGURE 3.41. 3D representation of the significant three-factor interaction obtained by the factorial design of γ.

3.10 Effect of charge-charge interactions within sol-gel matrix on the mobility of the encapsulated hemocyanin

As previously described, under particular experimental conditions the sol-gel matrix seems to be not able to fully immobilize hemocyanin in a single conformational state. We suspect an effect of pH and/or lactate on the electrostatic interaction between hemocyanin and the negatively charged silica gel walls (Wheeler et al., 2004). To test this hypothesis sodium chloride was added in the bulk solution to perturb the electrostatic environment of the silica matrix. Then, the behavior of the entrapped hemocyanin was investigated through the comparison of the oxygen binding curves of R-state conformer at pH 6.5 in presence of 250 mM and 500 mM of NaCl with the curves obtained in absence of NaCl (**Fig. 3.42**)

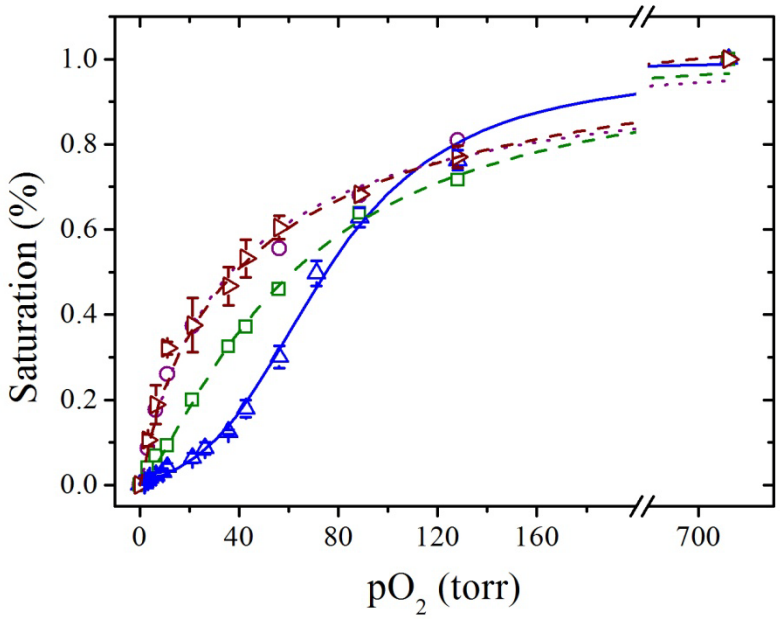

FIGURE 3.42. Oxygen binding curves of hemocyanin in solution (*in blue*) and entrapped in R-state at different NaCl concentration (0mM *in wine*; 250mM *in purple*; 500mM *in green*). The meausures were performed in buffer 50mM Tris, 20mM $CaCl_2$ at pH 7.8. Average and standard deviation resulting form 3 replicas for the hemocyanin in solution and the R-state without NaCl. Single oxygen binding curves for the R-state with 250mM and 500mM of NaCl are shown.

In presence of 250mM of NaCl, the cooperative index n=0.95 remains unchanged compared to the one of the R-state in absence of NaCl (0.90±0.06). However, the increase of the NaCl concentration to 500mM lead to an higher cooperative index (n=1.26). To verify if the effect shown for the entrapped R-conformer was due to direct modification of the properties of hemocyanin rather than modification of the electrostatic interactions with the matrix, oxygen-binding curves of hemocyanin in solution, both in presence and absence of 500mM of NaCl, were performed (**Fig. 3.43**). No significant differences in the cooperative index were evidenced (250mM NaCl: n=2.51; 0mM NaCl: n=2.48) . However a decrease (~10 torr) of the oxygen affinity was observed in presence of NaCl.

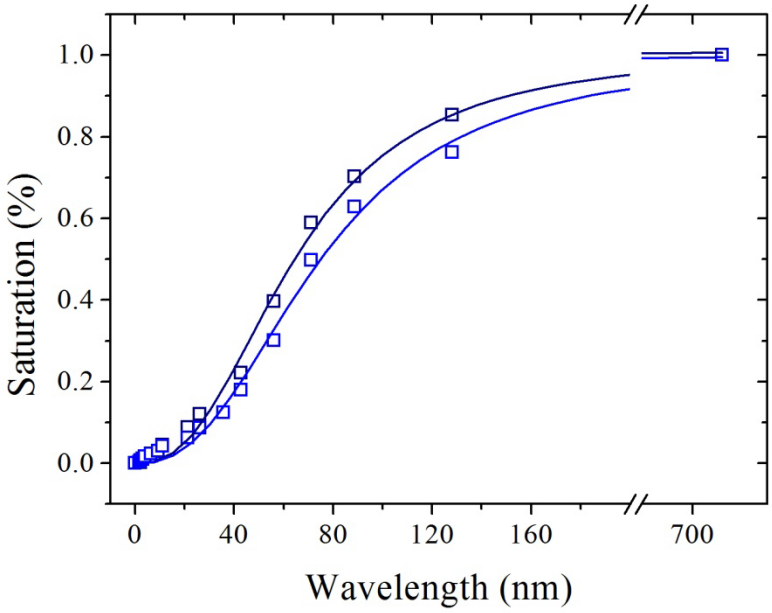

FIGURE 3.43. Oxygen binding curves of hemocyanin in solution in presence (*dark blue*) and absence (*light blue*) of 500mM of NaCl in buffer 50mM Tris, 20mM $CaCl_2$ at pH 7.8.

4. Discussion and conclusions

Most biological processes, like metabolism, catalysis, signal transduction and gene regulation, are finely regulated by allosteric mechanisms (Kalodimos, 2012). In the respiratory pigments these allosteric mechanisms lead to changes of the oxygen affinity in dependence of the environmental oxygen concentration and the binding of heterotropic allosteric effectors.

Phenomenological characterizations of the cooperative oxygen binding have been given by several models, with the classic MWC model (Monod et al., 1965) that can be considered the most famous. Its application in the investigation of the cooperativity of hemoglobin, considered the paradigm of allostery (Eaton et al., 2007), indicates the presence of two distinct conformational states, T- and R-, corresponding to the crystallographic structures of hemoglobin in deoxygenated and oxygenated conditions, respectively (Perutz et al., 1970). However, in the last years it has been demonstrated that the oxygen binding process in hemoglobin is much more complicated than the MWC description (Henry et al., 2002).

In this scenario, we investigated the cooperative oxygen binding process of the arthropod *Carcinus aestuarii* hemocyanin, which represents a more complex case study that allows to describe the basis of the cooperativity process on a broader basis. More in detail, our strategy was to functionally and structurally characterize all the allosteric conformers involved in the oxygen binding process, through the encapsulation of hemocyanin into a sol-gel matrix. It has been already demonstrated that this silica matrix represents a suitable tool for the investigation of allosteric proteins, avoiding the transitions between the different conformational states (Ronda et al., 2007; Samuni et al., 2006).

The project can be summarized in two main parts: the first one comprises all the preliminary analysis performed to find the best conditions for protein encapsulation and to exclude possible structural and functional artifacts due to the encapsulation of hemocyanin into the sol-gel matrix. The second one instead was addressed on the investigation of the cooperativity process of hemocyanin, at a functional and structural level. Also the allosteric effect of lactate was evaluated.

Before to start with the analysis of the entrapped hemocyanin, we focused our attention on the definition of the structural and optical properties of undoped matrix.

To this aim, we collected SAXS spectra of matrices prepared at different pH, in presence or absence of 25% glycerol and at different aging time, in order to detect microstructural changes that could give us some indication about the best conditions for protein encapsulation. Considering that the hemocyanin investigated in this work is a dodecamer made up of two hexamers of ~90 Å, the best condition would be represented by a matrix with pores size of ~200 Å. The SAXS data elaborated according to the fractal model defined by Teixeira (1988) didn't evidence differences in the pores size at the different conditions, with a mean value of ~93Å, much lower than the pores size expected. However, it has been demonstrated that the presence of protein during the gelification process strongly affects the properties of the sol-gel matrix, with a 2-fold increase of the pores size (Lou et al., 2009). The other two parameters obtained by the fractal analysis are the radius of the spherical silica particles that form the porous network and the fractal dimension. The radius of the particles seems to decrease in presence of glycerol, while the increase of the fractal dimension in function of the aging time described by Nair et al. (1996) was not confirmed in this work.

The lower dimensions of the silica particles in presence of 25% of glycerol are correlated to the better UV/visible absorption spectra of the sol-gel matrix prepared at this condition, compared to the one prepared in absence of glycerol. Indeed, as reported by Rabinovich (1994), the optical properties of the sol-gel matrix depends on the size of the colloidal particles that aggregate forming the gel. The transparence of the matrix was also confirmed by the CD and fluorescence emission spectra, even if in the latter case the spectra were slightly affected by light scattering.

Once defined that the protocol with glycerol provided optimal optical properties, we investigated the possible perturbing effects of the matrix on the encapsulated hemocyanin. Two distinct potential perturbing effects should be considered in this analysis: the effect of the matrix on the embedded hemocyanin and the one of glycerol. For the first one, both the physical constraint and the negative charge of the pores can produce slight alterations in the structure of the entrapped protein, affecting its functional properties (Lan et al., 1999). Instead, glycerol could decrease the volume and compressibility of the protein interior (Priev et al., 1996). From the comparison of the spectroscopic spectra of hemocyanin in

solution and entrapped into the matrix, the structural properties and the reversibility of the oxygen binding are not modified by protein encapsulation. Moreover, the CD and fluorescence investigation of the aromatic region of the protein in solution suggests that the presence of glycerol does not affect the interior of hemocyanin. Also the functional properties of hemocyanin are not changed by glycerol, as shown by the very similar oxygen binding behavior of hemocyanin in presence and absence of glycerol. However, an overall effect on the quaternary structure of hemocyanin can't be excluded.

At this point, excluded almost all the possible alterations of hemocyanin due to the encapsulation into the matrix, we focused our attention on the definition of a structural model for allostery in hemocyanin. To this aim, three analytical steps were followed: 1) the characterization of the functional properties of the entrapped hemocyanin; 2) the application of a model to describe the experimental data; 3) the validation of the model through structural data.

Therefore, we characterized the functional properties of hemocyanin entrapped into the matrix, both in presence and absence of oxygen, at three different pH (6.5, 7.5 and 7.8). We expected to block the R- and T-states at all the three pH. However, although the oxygen affinity of the hemocyanin entrapped into the matrix in presence and absence of oxygen was, as expected, higher and lower, respectively, compared to the protein in solution, a different ability of the matrix to avoid the allosteric transitions was evidenced as a function of pH. Indeed, the MWC assumption of a non-cooperative oxygen binding behavior of the pure R- and T-conformer was respected only at pH 6.5 for hemocyanin entrapped in presence and absence of oxygen, and at pH 7.5 for the hemocyanin entrapped in the oxygenated form. A slight cooperativity instead was observed at pH 7.8, both for the entrapped deoxy- and oxy- hemocyanin, and at pH 7.5 for the hemocyanin entrapped in deoxygenated condition. This means that at higher pH some conformational transitions were allowed.

Considering that the SAXS results didn't evidence pores size differences at the three pH, we suggest that the slight cooperative oxygen behavior observed was due to changes in the electrostatic interactions between the hemocyanin and the negatively charged walls of the pores matrix. The electrostatic influence of sol-gel matrix on the rotational mobility of entrapped molecules has been reported by

Wheeler et al. (2004), and our preliminary oxygen binding experiments performed in presence of sodium chloride, which perturbs the electrostatic environment, seem to confirm this hypothesis.

On the basis of the Hill-plot analysis of the oxygen binding curves obtained at three pH, a phenomenological description of the oxygen binding process at pH 6.5 and 7.8 was obtained by the application of allosteric models. We didn't include in this analysis the results obtained at pH 7.5 because the Hill-plots were not in agreement with the criteria of an asymptotic behavior of entrapped conformers. In literature the oxygen binding process of hemocyanins is generally described by extensions of the classic MWC model (Decker & Sterner, 1990; Helmann et al., 2010). However, without structural information, is very difficult to evaluate what model better describe the experimental observations. In these terms, the sol-gel data could represent an useful support in the definition of the model that better represent the real cooperative process. Therefore, taking into account both the data obtained in solution and the ones with hemocyanin entrapped into the matrix, a three-state MWC model was proposed. An extension of the classic two-state MWC model, with the addition of a third conformational state (S-state) was required to justify the lower K_R of the protein entrapped into the sol-gel matrix at both the pH, compared to the constant values predicted by the model. Moreover, from a qualitative comparison of the Hill-plots of the embedded hemocyanin (in presence and absence of oxygen) with the ones predicted by the three-state model it results that at pH 7.8 the matrix avoids the allosteric transition between the T- and R-state, but not between the S- and R-state, and between the T- and S-state, explaining the slight cooperative oxygen binding observed. Instead, the entrapped hemocyanin in presence and absence of oxygen at pH 6.5 seems to lead to an S- and a T-state, respectively. However, also at this pH the Hill-plots of the entrapped hemocyanin were not fully superimposable with those predicted by the model. Therefore, the application of the three-state model would be required also for the analysis of the entrapped hemocyanin, in order to evaluate if these data represents pure S- and T-state or, more probably, low percentages of other conformers were present.

To validate the three-state model, Small-Angle Neutrons Scattering (SANS) technique was applied to investigate structurally the differences between the

various conformers. We also tried to collect Small-Angel X-rays scattering (SAXS) spectra of hemocyanin entrapped into the matrix (data not shown), but the elimination of the scattering contribution of the matrix was more complicated than excepted. For this reason, although the resolution in SANS is lower than in SAXS, we performed SANS measurements of the different conformers, with the advantage that we could separate the scattering signatures of the entrapped protein and the sol-gel (Lou et al., 2009). We collected SANS spectra at pH 7.8 because it is a physiological pH and allowed to characterize the three distinct conformers, while the investigation at pH 6.5 would be limited only at the T- and S-state. The SANS pattern curves confirm the presence of three distinct conformers, with structural differences in terms of rotational arrangement of one hexamer compared to the other one and different distances between the two hexamers. Clearly, as demonstrated by the high variability of the fitted parameters obtained by the Quafit analysis (Spinozzi et al., 2012; Spinozzi & Beltramini, 2012), a fine reconstruction of the quaternary structures of the conformers, both in presence and absence of oxygen, would require further analysis. However, the interhexameric distance of the R-conformer in presence of oxygen (d =106±8Å) corresponds to the one calculated by Micetic et al. (2010) through the SAXS analysis of the oxygenated *C. aestuarii* hemocyanin in solution. Therefore, we have an indication that the experimental approach that we adopted is correct.

Until now, we have discussed about the correlation between the functional properties and the quaternary structures of the different conformers. However information about the coordination geometry of the active sites are required. To this aim, X-ray Absorption Spectroscopy (XAS) measurements of the conformers blocked at pH 7.8, both in presence and absence of oxygen were collected. The comparison between the spectra of higher and lower oxygen affinity conformers evidenced differences only for the measures performed in absence of oxygen. This means that the modulation of the oxygen affinity occurs through changes of active site geometry when the conformers are in the deoxygenated form while the oxygenated forms of all conformers converge to the same complex structure. Interestingly, the intensity of the band at 8982eV, which is correlated to displacement of the Cu(I) from the plane defined by the three His (Blackburn et al., 1989; Brown et al., 1980), was lower for the T-conformer compared to the S-

conformer. Therefore a greater degree of distortion toward pseudotetrahedral geometry was suggested in the case of the T-state, while a more likely trigonal planar geometry would represent the active site of the S-state. Even if the sol-gel matrix didn't allow us to characterize also the coordination geometry of the R-state deoxygenated, these results evidenced that the cooperativity process is due to changes of the deoxygenated active site, with higher oxygen affinity in the case of conformers characterized by a trigonal planar geometry. Hirota et al. (2008) showed that at the basis of the Bohr effect the same changes of the coordination geometry of the active site are involved, with higher oxygen affinity in the case of a trigonal planar geometry (high pH) and lower in the case of pseudotetrahedral geometry (low pH) (Hirota et al 2008). In this frame, we can put forward the hypothesys that the structural mechanisms responsible for both the cooperativity and the Bohr effect are the same at the active site level.

More complicated is the determination of the mechanisms that link the different quaternary structures of the conformers to the changes in the coordination geometry of the active sites. Although more hemocyanin structures resolved at a crystallographic resolution would be necessary to clarify this point, some indications are given by the differences in the aromatic region observed in the CD and fluorescence emission spectra of the three conformers. In particular, the shift in the fluorescence emission maximum upon excitation at 278 nm, but not at 295 nm, suggests different exposure of Tyr residues (but not Trp residues) to the solvent in X conformer as compared to Y conformer. On the basis of the sequence data on arthropod hemocyanins currently available and the crystal structure of *P. interruptus* hemocyanin it is suggested a possible mechanism to describe how the quaternary conformational changes are linked to the different coordination geometry of the active site during the oxygen binding process. Briefly, we suggest that at the intersubunits contact region of the trimer Tyr 339 and His 302 of each subunits are involved in hydrogen bonds that affect the structure of the active sites (**Fig. 4.1**). The residues involved in this interactions are all conserved within almost all the arthropod hemocyanin sequences (**Supplementary materials**). The model here proposed is based on the observation that the subunit *c* homoexamer of *P. interruptus*, with a mutation of the His344, does not bind oxygen in a

cooperative way, compared to the homoexamer of subunit *a* (Johnson et al., 1987).

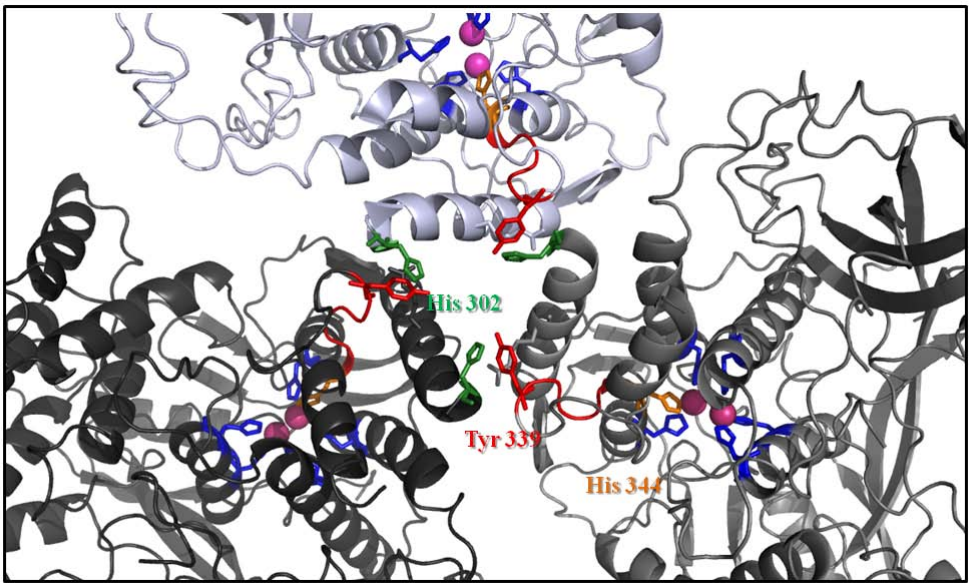

FIGURE 4.1. Hypothetical model for the molecular basis of the cooperative oxygen binding process based on the crystallographic structure of *P. interruptus* (1HYC.pdb) . The interaction of the Try339 and the His302 of each subunit, in the intersubunit contact region (in *light gray*, *dark gray* and *black*), affect the displacement of the His344 resulting in changes of the coordination geometry of the active site. *Pymol* software was used to illustrate the structure.

Finally, we wanted to verify if the sol-gel approach used for the definition of the cooperativity process in hemocyanin could be useful also for the determination of the allosteric effect of lactate. Either the S- and T- conformers at pH 6.5 shown higher oxygen affinity in presence of lactate, with a K_S^L similar to the K_R predicted by the three-state model, and a K_T^L very close to the predicted K_S. Therefore, these functional results indicate an allosteric equilibrium shift of the T-state towards the S-state, and from the S-state to the R-state in the presence of lactate. Even if at this pH no information can be obtained for the R-state in presence of lactate, a modulation of the allosteric equilibrium between the T/S- and S/R-conformers, as a function of the lactate concentration, could be at the basis of the changes in oxygen affinity. Weber et al. (2008) have demonstrated that lactate increases the oxygen affinity of *Carcinus aestaurii* hemocyanin in solution by preferentially increasing the equilibrium constant K_T, without

significantly affecting that of the R-state (K_R). An indication of the allosteric equilibrium modification from lower to higher oxygen affinity conformers, without changes of the K_R, was obtained at pH 7.8. At this pH, when the hemocyanin was entrapped in presence of oxygen and lactate, it seems to be mainly represented by R-conformers, and by S-conformers, when deoxygenated hemocyanin was entrapped. However, at this experimental condition more analysis should be performed, due to the low quality of the data. The comparison of the structure of the R- and S- conformers at pH 6.5 both in presence and absence of lactate could validate the hypothesis here described. SANS measures at this pH will be performed.

SANS spectra instead was collected at pH 7.8, in order to compare the results with the structures obtained in absence of lactate. Structural effects have been already evidenced on the 2x6-meric hemocyanins of *C. aestuarii* (Hirota et al., 2010) and *Homarus americanus* (Hartmann et al., 2001), with an increase or decrease of the interhexameric distance in function of the lactate concentration. Our results confirm that lactate induces a decrease of the interhexameric distance in all the conformers investigated. Again, it could be interesting to assess if these structural changes are due to shifts towards higher oxygen affinity conformers or if an independent allosteric mechanism is involved. The results of the factorial analysis evidenced different arrangement of the two hexamers as a function of the oxygenation state and the conformational state. A definition of a trend in terms or rotational arrangement of an hexamer compared to the other one actually is really complicated, and requires to increase the number of independent fitting procedures by QUAFIT in order to improve the statistics. However, we can correlate the oxygen affinity of the hemocyanin with the distances between the two hexamers. Indeed, significantly smaller interhexameric distances were observed either after the allosteric transition towards higher oxygen affinity conformational states, and after the binding of oxygen.

In conclusion, this work has shown that the oxygen binding process of *C. aesturaii* hemocyanin is adequately described by the three-state MWC model, with the T-, S- and R- states characterized by different coordination geometry in the deoxygenated form. From our functional results instead it seems that the increase of the oxygen affinity induced by lactate is due to shift of the allosteric

equilibrium towards the higher oxygen affinity conformers that in our case is represented by R-state. A schematic view of the whole process is reported in **Fig. 4.2**. In a physiological point of view, the presence of three distinct conformers increase the functional plasticity of the hemocyanin in response to different environmental conditions.

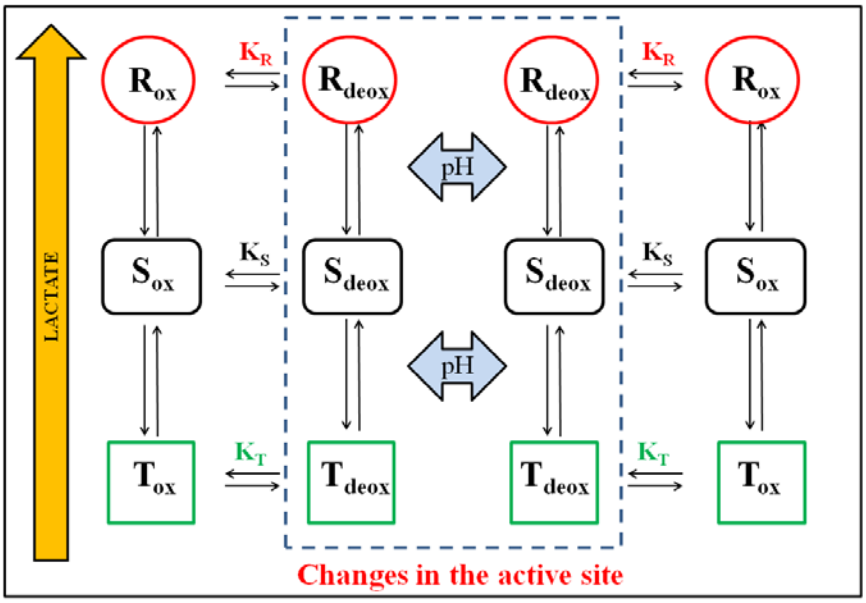

FIGURE 4.2. Schematic view of the cooperativity process of *C. aestuarii* hamocynain.

Moreover, this work has demonstrated that sol-gel matrix provides a suitable approach for the investigation of structure–function relationships of proteins. However, the entrapment of the protein into the matrix should be performed at different experimental conditions, due to the different ability of the matrix to fully avoid the allosteric transitions. Indeed, in our case the matrix was not able to fully entrap the hemocaynin at higher pH (7.5 and 7.8), while at pH 6.5 a constraint effect limited the entrapment of the R-state.

References

Avnir, D., Braun, S., Lev, O., Ottolenghi, M. (1994). Enzymes and other proteins entrapped in sol-gel materials. *Chemistry of Materials* **6**: 1605-1614.

Baldwin, M.J., Root, D.E., Pate, J.E., Fujisawa, K., Kitajima, N., Solomon, E.I. (1992). Spectroscopic studies of side-on peroxide-bridged binuclear copper (II) model complexes of relevance to oxyhemocyanin and oxytyrosinase. *Journal of the American Chemical Society* **114**: 10421-10431.

Beltramini, M., Ricchelli, F., Salvato, B. (1984). The kinetics of the reaction of Octopus vulgaris hemocyanin with cyanide. Its significance for the structure of the 11S subunit of molluscan hemocyanin. *Inorganica Chimica Acta* **92**: 209-217.

Beltramini, M., Bubacco, L., Salvato, B., Casella, L., Gullotti, M., Garofani, S. (1992). The aromatic circular dichroism spectrum as a probe for conformational changes in the active site environment of hemocyanins. *Biochimica et Biophysica Acta* **1120**: 24-32.

Beltramini, M., Colangelo, N., Giomi, F., Bubacco, Di Muro, P., Hellmann, N., Jaenicke, E., Decker, H. (2005). Quaternary structure and functional properties of *Penaeus monodon* hemocyanin. *FEBS Journal* **272**: 2060-2075.

Besanger, T.R., Chen, Y., Deisingh, A.K., Hodgson, R., Jin, W., Mayer, S., Brook, M.A., Brennan, J.D. (2003). Screening of inhibitors using enzymes entrapped in sol-gel derived materials. *Analytical Chemistry* **75**: 2382-2391

Bhatia, R.B., Brinker, J. (2000). Aqueous sol-gel process for protein encapsulation. *Chemistry of Materials* **12**: 2434-2441.

Blackburn, N.J., Strange, R.W., Reedijk, J., Volbeda, A., Farooq, A., Kenneth, D.K., Zubieta, J. (1989). X-ray absorption edge spectroscopy of copper(I) complexes. Coordination geometry of copper(I) in the reduced forms of copper proteins and their derivatives with carbon monoxide. *Inorganic chemistry* **28**: 1349-1357.

Booth, C.E., McMahon, B.R., Pinder, A.W. (1982). Oxygen uptake and the potentiating effects of increased hemolymph lactate on oxygen transport during excercice in the blue crab *Callinctes sapidus*. *Journal of Comparative Physiology* **148**: 111–121.

Box, G.E.O, Hunter, W.G. (1978). Statistic for experimenters. *Wiley*.

Brennan, J.D., Benjamin, D., Dibattista, E., Gulcev, M.D. (2003). Using sugar and amino acid additives to stabilize enzymes within sol–gel derived silica. *Chemistry of Materials* **15**: 737–745.

Bridges, C.R. (2001). Modulation of hemocyanin oxygen affinity: properties and physiological implications in a changing world. *Journal of Experimental Biology* **204**: 1021-1032.

Brown, J.M., Powers, L., Kincaid, B., Larrabee, J.A., Spiro, T.G. (1980). Structural studies of the hemocyanin active site. 1. Extended x-ray absorption fine structure (EXAFS) analysis. *Journal of the American Chemical Society* **102**: 4210-4216.

Bruno, S., Bonaccio, M., Bettati, S., Rivetti, C., Viappiani, C., Abbruzzetti, S., Mozzarelli, A. (2001). High and low oxygen affinity conformations of T-state hemoglobin. *Protein Science* **10**: 2401-2407.

Cerveau, G., Corriu, R.J.P., Framery, E. (1999). Sol-gel process: temperature effect on textural properties of a monophasic hybrid material. *Chemical Communications* **20**: 2081-2082.

Chang, G., Tatsu, Y., Goto, T., Imaishi, H., Morigaki, K. (2010). Glucose concentration determination based on silica sol-gel encapsulated glucose oxidase optical biosensor arrays. *Talanta* **83**: 61-65.

Changeoux, J.P. (1961). The feedback control mechanisms of biosynthetic L-threonine deaminase by L-isoleucine. *Cold Spring Harbor Symposia on Quantitative Biology* **26**: 313-318

Cong, Y., Zhang, Q., Woolford, D., Schweikardt, T., Khant, H., Dougherty, M., Ludtke, S., Chiu, W., Decker, H. (2009). Structural mechanism of SDS-induced enzyme activity of scorpion hemocyanin revealed by electron cryomicroscopy. *Structure* **17**: 749-758.

Coradin, T., Boissiere, M., Livage, J. (2006). Sol-gel chemistry in medical science. *Current Medical Chemistry* **13**: 99-108.

Cresimbeni, M.C., Nola, V., Clop, P.D., Marin, G.N., Perillo, M.A. (2010). Activity modulation and reusability of β-D-galactosidase confined in sol-gel derived porous silicate glass. *Colloids and Surfaces. B: Biointerferenced* **76**: 387-396.

Cui, Q., Karplus, M., (2007). Allostery and cooperativity revisited. *Protein Science* **17**: 1295-1307.

Dainese, E., Di Muro, P., Beltramini, M., Salvato, B., Decker, H. (1998). Subunits composition and allsoteric control in *Carcinus aestuarii* hemocyanin. *European Journal of Biochemistry* **256**: 350-359.

Decker, H., Connelly, P.R., Robert, C.H., Gill, S.J. (1988). Nested allosteric interaction in tarantula hemocyanin revealed through the binding ox oxygen and carbon monoxide. *Biochemistry* **27**: 6901-6908.

Decker, H., Sterner, R. (1990). Nested allostery of arthropodan hemocyanin (*Eurypelma californicum* and *Homarus americanus*). The role of protons. *Journal of Molecular Biology* **211**: 281-283.
Decker, H., Hellmann, N., Jaenicke, E., Lieb, B., Meissner, U., Markl, J. (2007). Minireview: recent progress in hemocyanin research. *Integrative and Comparative Biology* **4**: 631-644.

Decker, H., van Holde, K.E. (2011). Oxygen and the evolution of life. *Springer*.

Dickerson, R.E., Geis, I. (1983). Hemoglobin: structure, function and evolution. *Benjamin/Cummings*.

Di Muro, P., Beltramini, M., Nikolov, P., Petkova, I., Salvato, B., Ricchelli, F. (2002). Fluorescence spectroscopy of the tryptophan microenvironment in *Carcinus aestuarii* hemocyanin. *Zeitschrift fur Naturforschung C* **57**: 1084-1091.

Eaton, W.A., Henry, E.R., Hofrichter, J., Mozzarelli, A. (1999). Is cooperative oxygen binding by hemoglobin really understood?. *Nature Structural Biology* **6:** 351-358.

Eaton, W.A., Henry, E.R., Hofrichter, J., Mozzarelli, A., Bettati, S., Viappiani, C., Mozzarelli, A. (2007). Evolutions of allosteric models for hemoglobin. *Life* **59**: 586-599.

Ellerby, L.M., Nishida, C.R., Yamanaka, S.A., Dunn, B., Valentine, J.S., Zink, J.I. (1992). Encapsulation of proteins in transparent porous silicate glasses prepared by the sol-gel method. *Science* **28**: 1113-1115.

Erker, W., Schoen, A., Baschè, T., Decker, H. (2004). Fluorescence labels as sensors for oxygen binding of arthropod hemocyanins. *Biochemical and Biophysical Research Communications* **324**: 893-900.

Erker, W., Beister, U., Decker, H. (2005). Cooperative transition in the conformation of 24-mer tarantula hemocyanin upon oxygen binding. *Journal of Biological Chemistry* **280**: 12391-12396.

Farnum, M., Zukoski, C. (1999). Effect of glycerol on the interactions and solubility of bovine pancreatic trypsin inhibitor. *Biophysical journal* **76**: 2716-2726.

Favilla, R., Goldoni, M., Di Muro, P., Salvato, B., Beltramini, M. (2002). Guanidinium chloride induced unfolding of a hemocyanin subunit from *Carcinus aestuarii* apo form. *Biochimica et Biophysica Acta* **1597**: 42:50.

Ferrel, J.E. (2009). Q&A: cooperativity. *Journal of Biology* **8**: 53.

Flora, K.K., Brennan, J.D. (2001). Effect of matrix aging on the behavior of human serum albumin entrapped in a tetraethyl orthosilicate-derived glass. *Chemistry of Materials* **13**: 4170–4179.

Fuentes, L., Oyola, J., Fernandez, M., Quinones, E. (2004). Conformational changes in azurim from *Pseudomona aeruginosa* induced through chemical and physical protocols. *Biophysical journal* **87**: 1873-1880.

Gaykema, W.P.J., Volbeda, A., Hol, W.G.J. (1986). Structure determination of *Panulirus interruptus* hemocyanin at 3.2 Å resolution. *Journal of Molecular Biology* **187**: 255-275.

Gill, I., Ballesteros, A. (1998). Encapsulation of biologicals within silicate, siloxane and hybrid Sol–gel polymers: an efficient and generic approach. *Journal of the American Chemical Society* **10**: 8587–8598.

Gilliland, J.W., Yokoyama, K., Yip, W.T. (2005). Comparative study of guest charge-charge interactions within silica sol-gel. *Journal of Physical Chemistry B* **24**: 4816-4823.

Gomes, S.P., Odlozilíková, M., Almeida, M.G., Araújo, A.N., Couto, Cristina, M.C.M., Conceição, B.S.M., Montenegro, M. (2007). Application of lactate amperometric sol-gel biosensor to sequential injection determination of L-lactate. *Journal of Pharmaceutical and Biomedical Analysis* **43**: 1376-1381.

Graham, R.A., Mangum, C.P. Terwillinger, R.C., Terwillinger, N.B. (1983). The effect of organic acids on oxygen binding of hemocyanin from the crab *Cancer magister*. *Comparative Biochemistry and Physiology* **74**: 353-375.

Gupta, R., Chaudhury, N.K. (2007). Entrapment of biomolecules in sol-gel matrix for applications in biosensors: problems and future prospects. *Biosensors and Bioelectronics* **22**: 2387–2399.

Hartmann, H., Lohkamp, B., Hellmann, N., Decker, H. (2001). The allosteric effector L-lactate induces a conformational change of 2x6-meric lobster hemocyanin in the oxy state as revealed by small angle X-ray scattering. *Journal of Biological Chemistry* **276**: 19954-19958.

Hartmann, H., Decker, H. (2002). All hierarchical levels are involved in conformational transitions of the 4x6-meric tarantula hemocyanin upon oxygenation. *Biochimica et Biophysica Acta* **1601**: 132-137.

Haynie, D.T. (2008). Biological thermodynamics. *Cambridge.*

Hazes, B., Magnus, K.A., Bonaventura, C., Bonaventura, J., Dauter, Z., Kalk, K.H., Hol, W.G. (1993). Crystal structure of deoxygenated *Limulus polyphemus* subunit II hemocyanin at 2.18 A resolution: clues for a mechanism for allosteric regulation. *Protein science* **2**: 597-619.

Helmann, N., Paoli, M., Giomi, F., Beltramini, M. (2010). Unusual oxygen behavior of a 24-meric crustacean hemocyanin. *Archives of Biochemistry and Biophysics* **495**: 112-121.

Hench, L.L., West, J.K. (1990). The sol-gel process. *Chemical reviews* **90**: 33-72.

Henry, E.R., Bettati, S., Hofrichter, J., Eaton, W. (2002). A tertiary two-state allosteric model for hemoglobin. *Biophysical Chemistry* **98**: 149-164.

Herskovits, T. T. (1988). Recent aspects of the subunit organization and dissociation of hemocyanins. *Comparative Biochemistry and Physiology* **91**:597-611.

Hill, A.V. (1910). The combination of haemoglobin with oxygen and with carbon monoxide. *Journal of Physiology* **40**: 4-7.

Hirota, S., Kawahara, T., Beltramini, M., Di Muro, P., Magliozzo, R.S., Peisach, J., Powers, L.S., Tanaka, N., Nagao, S., Bubacco, L. (2008). Molecular basis of the bohr effect in arthropod hemocyanin. *Journal of Biological Chemistry* **283**: 31941-31948.

Hirota, S., Tanaka, N., Micetic, I., Di Muro, P., Nagao, S., Kitagishi, H., Kano, K., Magliozzo, R.S., Peisach, J., Beltramini, M., Bubacco, L. (2010). Structural basis of the lactate dependent allosteric regulation of oxygen binding in arthropod hemocyanin. *Journal of Biological Chemistry* **285**: 19338-19345.

Hubler, R., Fertl, B., Hellmann, N., Decker, H. (1998). On the stability of the 24-meric hemocyanin from *Eurypelma californicum*. *Biochimica et Biophysica Acta* **1383**: 327-339.

Johnson, B. A., Bonaventura, C., Bonaventura, J. (1984). Allosteric modulation of *Callinectes sapidus* hemocyanin by binding of L-lactate. *Biochemistry* **23**: 872–878.

Johnson, B. A., Bonaventura, J., Bonaventura, C. (1987). Determination of L-lactate binding stoichiometry and differences in allosteric interactions of structurally distinct homohexamers from *Panulirus interruptus* hemocyanin. *Biochimica et Biophysica Acta* **916**: 376–380.

Johnson, B.A., Bonaventura, C., Bonaventura, J. (1988). Allostery in *Callinectes sapidus* hemocyanin: cooperative oxygen binding and interactions with L-lactate, calcium, and protons. *Biochemistry* **27**: 1995-2001.

Kalodimos, C.G. (2012). Protein function and allostery: a dynamic relationship. *Annals of the New York Academy of Sciences* **1260**: 81-86.

Khan, I., Shannon, C.F., Dantsker, D., Friedman, A.J., Perez-Gonzales-de-Apodaca, J., Friedman, J.M. (2000). Sol-gel trapping of functional intermediates of hemoglobin: geminate and bimolecular recombination studies. *Biochemistry* **39**: 16099-16109.

Klemperer, W.G., Ramamurthi, S.D. (1988). Molecular growth pathways in silica sol-gel polymerization. *MRS Proceedings* **121:** PROC-121-1.

Koshland, D.E., Nemethy, G., and Filmer, D. (1966). Comparison of experimental binding data and theoretical models in proteins containing subunits. *Biochemistry* **5:** 365-385.

Kraus, S.C., Czolk, R., Reichert, J., Ache, H.J. (1993). Optimization of the sol-gel process for the development of optochemical sensors. *Sensors and Actuators B: Chemical* **15**: 199-202.

Kunarti, E.S., Moran, G.M. (2008). Entrapment of avidin in sol-gel derived silica glasses. *Jouranl of Physical Science* **19**: 31-44.

Kusche, K., Hembach, A., Hagner-Holler, S., Gebauer, W., Burmester, T. (2003). Complete subunit sequences, structure and evolution of the 6 x 6-mer hemocyanin from the common house centipede, *Scutigera coleoptrata*. *European Journal of Biochemistry* **325**: 99-109.

Lakowicz, J.R., Laczko, G., Gryczynski, I., Cherek, H. (1986). Measurement of subnanosecond anisotropy decays of protein fluorescence using frequency-domain fluorometry. *Journal of Biological Chemistry* **261**: 2240-2245.

Lan, E.H., Dave, B.C., Fukuto, J.M., Dunn, B., Zink, J.I., Valentine, J.S. (1999). Synthesis of sol-gel encapsulated heme proteins with chemical sensing properties. *Journal of Materials Chemistry* **9**: 45-53.

Lelong, G., Price, D.L., Grady, J.W., Saboungi, M.L. (2007). Dynamics of trehalose molecules in confined solutions. *Journal of Chemical Physics* **127**: 065102.

Lepeshkevich, S.V., Parkhats, M.V., Stepuro, I.I., Dzhagarov, B.M. (2009). Molecular oxygen binding with α and β subunits within the R quaternary state of human hemoglobin in solutions and porous sol–gel matrices. *Biochimica et Biophysica Acta* **1794**: 1823-1830.

Lin, J., Brown, C.W. (1997). Sil.gel glass as a matrix for chemical and biochemical sensing. *Trend in Analytical Chemistry* **16**: 200-211.

Lou, G., Zhang, Q., Castillo, A.R.D.C., Urban, V., O'Neil, H. (2009). Characterization of sol-gel encapsulated proteins using small-angle neutron scattering. *ACS Applied Materials & Interfaces* **10**: 2262-2268.

Magnus, K.A., Ton-That, H. (1991). The crystal structure of the oxygenated form of subunit II of *Limulus polyphemus* hemocyanin. *Journal of inorganic Biochemistry* **43**: 167.

Magnus, K.A., Hazes, B., Ton-That, H., Bonaventura, C., Bonaventura, J., Hol, W.G.J. (1994). Crystallographic analysis of oxygenated and deoxygenated states of arthropod hemocyanin shows unusual differences. *Proteins* **19**: 302-309.

Makino, N. (1986). Analysis of oxygen binding to *Panulirus japonicus* hemocyanin. The effect of divalent cations on the allosteric transition. *European Journal of Biochemistry* **154**: 49-55.

Mangum, C. P. (1983a). On the distribution of lactate sensitivity haemocyanins. *Marine Biology Letters* **4**:139-149.
Markl, J., 1986. Evolution and function of structurally diverse subunits in the respiratory protein hemocyanin from arthropods. *Biological Bulletin* **171**, 90–115.

Markl, J., Moeller, A., Martin, A.G., Rheinbay, J., Gebauer, W., Depoix, F. (2009). 10-A cryoEM structure and molecular model of the Myriapod (*Scutigera*) 6x6mer hemocyanin: understanding a giant oxygen transport protein. *Journal of Molecular Biology* **392**: 362-380.

Martin, A.G., Depoix, F., Stohr, M., Meissner, U., Hagner-Holler, S., Hammouti, K., Burmester, T., Heyd, J., Wriggers, W., Markl, J. (2007). *Limulus polyphemus* hemocyanin: 10 Å cryo-EM structure, sequence analysis, molecular modelling and rigid-body fitting reveal the interfaces between the eight hexamers. *Journal of Molecular Biology* **366**: 1332-1350.

McDonagh, C., Sheridan, F., Butler, T., MacCraith, B.D. (1996). Characterization of sol-gel derived silica films. *Journal of Non-Crystalline Solids* **194**: 72-77.

Meissner, U., Stohr, M., Kusche, K., Burmester, T., Stark, H., Harris, J.R., Orlava, E.V., Markl, J. (2003). Quaternary structure of the European spiny lobster (*Palinurus elephans*). 1x6-mer hemocyanin from cryoEM and amino acid sequence data. *Journal of Molecular Biology* **325**: 99-109.

Menze, M.A., Hellmann, N., Decker, H., Grieshaber, M.K. (2005). Allosteric models for multimeric proteins: oxygen-linked effector binding in hemocyanin. *Biocehmistry* **44**: 10328-10338.

Metz, M., Solomon, E.I. (2001). Dioxygen binding to deoxyhemocyanin: electronic structure and mechanism of the spin-forbidden two-electron reduction of O_2. *Journal of the American Chemical Society* **123**: 4938-4950.

Micetic, I., Losasso, C., Di Muro, P., Tognon, G., Benedetti, P., Beltramini, M. (2010). Solution structures of 2x6-meric and 4x6-meric hemocyanins of crustaceans *Carcinus aestuarii, Squilla mantis* and *Upogebia pusilla. Journal of Structural Biology* **171**: 1-10.

Minton, A.P., Imai, K. (1974). The three-state model: a minimal allosteric description of homotropic and heterotropoc effects in the binding of ligands to hemoglobin. *Proceedings of the National Academy of Sciences* **71**: 1418-1421.

Monod, J., Jacob, F. (1961). General conclusion: telenomic mechanisms in cellular metabolism, growth, and differentiation. *Cold Spring Harbor Symposia on Quantitative Biology* **26**: 389-401.

Monod, J., Wyman, J., Changeux, J. P. (1965). On the nature of allosteric transitions: a plausible model. *Journal of Molecular Biology* **12**: 88-118.

Morris, S. (1990). Organic ions as modulators of respiratory pigment function during stress. *Physiological Zool*ogy **63**, 253–287.

Mozzarelli, A., Rivetti, C., Rossi, G.L., Henry, E.R, Eaton, W.A. (1991). Crystals of haemoglobin with the T quaternary structure bind oxygen noncooperatively with no Bohr effect. *Nature* **351**: 416-419.

Nair, B.N., Elferink, W.J., Keizer, K., Verweij, H. (1996). Sol-gel synthesis and characterization of microporous silica membranes I: SAXS study on the growth of polymeric structures. *Journal of colloidal and interface science* **178**: 565-570.

Neuteboom, B., Jekel, P.A., Beintema, J.J., 1992. Primary structure of hemocyanin subunit c from *Panulirus interruptus*. *European Journal of Biochemistry* **206**: 243–249.

Neylon, C. (2008). Small angle neutron and X-ray scattering in structural biology: recent examples from the literature. *European Biophysics Journal* **37**: 531-541.

Nickerson, K.W., van Holde, K.E. (1971). A comparison of molluscan and arthropod hemocyanin—I. Circular dichroism and absorption spectra. *Comparative Biochemistry and Physiology. Part B: Comparative Biochemistry* **39**: 855-872.

Oujji, N.B., Bakas, I., Istamboulié, G., Ait-Ichou, I., Ait-Addi, E., Rouillon, R., Noguer, T. (2012). Sol–gel immobilization of acetylcholinesterase for the determination of organophosphate pesticides in olive oil with biosensors. *Food control* **30**: 657-661.

Pauling, L. (1935). The oxygen equilibrium of hemoglobin and its structural interpretation. *Proceedings of the National Academy of Sciences* **21**: 186-191.

Peracchi, A., Mozzarelli, A. (2011). Exploring and exploiting allostery: models, evolution , and drug targeting. *Biochimica et Biophysica Acta* **1814**: 922-933.

Perutz, M.F. (1970). Stereochemistry of cooperative effects in hemoglobin. *Nature* **228**: 726-739.

Priev, A., Almagor, A., Yedgar, S., Gavish, B. (1996). Glycerol decreases the volume and compressibility of protein interior. *Biochemistry* **35**: 2061-2066.

Putman, C.D., Hammel, M., Hura, G.L., Tainer, J.A. (2007). X-ray solution scattering (SAXS) combined with crystallographic and computation: defining accurate macromolecular structures, conformations and assemblies in solution. *Quarterly Reviews of Biophysics* **40**: 191.285.

Rabinovich, E.M. (1994). Sol-gel processing - General principles. *Springer*.

Ricchelli, F., Salvato, B., Filippi, B., Jori, G. (1980). Conformational changes of *Carcinus maenas* hemocyanin induced by urea. *Archives of Biochemistry and Biophysics* **202**: 277-288.

Ricchelli, F., Jori, G., Tallandini, L., Zatta, P., Beltramini, M., Salvato, B. (1984). The role of copper and quaternary structure on the conformational properties of *Octopus vulgaris* hemocyanin. *Archives of Biochemistry and Biophysics* **235**: 461-469.

Ricchelli, F., Beltramini, M., Flamigni, L., Salvato, B. (1987). Emission quenching mechanisms in *Octopus vulgaris* hemocyanin: steady-state and time-resolved fluorescence studies. *Biochemistry* **26**: 6933-6939.

Richey, B., Decker, H., Gill, S.J. (1985). Binding of oxygen and carbon monoxide to arthropod hemocyanin: an allosteric analysis. *Biochemistry* **24**; 109-117.

Robert, C.H., Decker, H., Richey, B., Gill, S.J., Wyman, J. (1987). Nesting: hierarchies of allosteric interactions. *Proceedings of the National Academy of Sciences* **84**: 1891-1895.

Ronda, L., Faggiano S., Bettati, S., Hellmann, N., Decker, H., Weidenbach, T., Mozzarelli, A. (2007). Hemocyanin from *E. californicum* encapsulated in silica gels: oxygen binding and conformational states. *Gene* **398**: 202-207.

Safo, M.K., Ahmed, M.H., Ghatge, M.S., Boyiri, T. (2011). Hemoglobin-ligand binding: understanding Hb function and allostery on atomic level. *Biochimica et Biophysica Acta* **1814**: 797-809.

Sakay-Kato, K., Ishikura, K. (2009). Integration of biomolecules into analytical systems by means of silica sol-gel technology. *Analytical Sciences* **25**: 969-978.

Samuni, U., Juszczak, Dantsker, D., Khna, I., Friedman, A.J., Perez-Gonzales-de-Apodeca, J., Bruno, S., Hui, H., Colby, J.E., Karasik, E., Kwiatkowski, L.D., Mozzarelli, A., noble, R., Friedman, J.M. (2003). Functional and spectroscopic characterization of half-liganded iron-zinc hybrid hemoglobin: evidence for conformational plasticity within the T-state. *Biochemistry* **42**: 8272-8288.

Samuni, U., Roche, C.J., Dantsker, D., Juszczak, L.J., Friedman, J.M. (2006). Modulation of reactivity and conformation within the T-quaternary state of human hemoglobin: the combined use of mutagenesis and sol-gel encapsulation. *Biochemistry* **45**: 2820-2835.

Sanna, M.T., Olianas, A., Castagnola, M., Sollai, L., Manconi, B., Salvadori, S., Giardina, B., Pellegrini, M. (2004). Oxygen-binding modulation of hemocyanin from the slipper lobster *Scyllarides latus*. *Comparative Biochemistry and Physiology. Part B: Biochemistry and Molecular Biology* **139**: 261-268.

Scherer, G.W. (1998). Coarsening in a viscous matrix. *Journal of the American Ceramic Society* **81**: 49-54.

Schmidt, H., Scholze, H., Kaiser, A. (1984). Principles of hydrolysis and condensation reaction of alkoxysilanes. *Journal of Non-Crystalline Solids* **63**: 1-11.

Shaklai, N., Daniel, E. (1970). Fluorescence properties of hemocyanin from *Levantina hierosolima*. *Biochemistry* **9**:564-568.

Shibayama, N., and Saigo, S. (1995). Fixation of the quaternary structures of human adult haemoglobin by encapsulation in transparent porous silica gels. *Journal of Molecular Biology* **251**: 203-209.

Shibayama, N., and Saigo, S. (2001). Direct observation of two distinct affinity conformations in the T state human deoxyhemoglobin. *FEBS Letters* **492**: 50-53.

Silveira, C.M., Gomes, S.P., Araujo, A.N., Montebegro, M.C., Todorovic, S., Viana, A.S., Silva, R.J., Moura, J.J., Almeida, M.G. (2010). An efficient non-mediated amperometric biosensor for nitrite determination. *Biosensors & Bioelectronics* **25**: 2026-2032.

Smith, T.A., Penner-Hahn, J.E., Berging, M.A., Doniach, S., Hodgson, K.O. (1985). Polarized x-ray absorption edge spectroscopy of single-crystal copper (II) complexes. *Journal of the American Chemical Society* **107**: 5945-5955.

Solomon, E.I., Tuczek, F., Root, D., Brown, C.A. (1994). Spectroscopy of binuclear dioxygen complexes. *Chemical Reviews* **94**: 827-856.

Spinozzi, F., Beltramini, M. (2012). QUAFIT: a novel method for the quaternary structure determination from small-angle scattering data. *Biophysical Journal* **103**: 511-521.

Spinozzi, F., Mariani, P., Micetic, I., Ferrero, C., Pontoni, D., Beltramini, M. (2012). Quaternary structure heterogeneity of oligomeric proteins: a SAXS and SANS study of the dissociation products of *Octopus vulgaris* hemocyanin. *Plos One* **7**: e49644.

Srere, P.A., Kosicki, G.W., Lumry, R. (1961). Isotope rate effects with D_2O in several enzyme systems. *Biochimica et Biophysica Acta* **50**: 184-185.

Stuhrmann, H. (2004). Unique aspects of neutron scattering for the study of biological systems. *Reports on Progress in Physics* **67**: 1073-1115.

Taylor, A.C., Astall, C.M., Atkinson, R.J.A. (2000). A comparative study of the oxygen transporting properties of the hemocyanin of five species of thalassinidean mud-shrimps. *Journal of Experimental marine Biology and Ecology* **244**: 265-283.

Teixeira, J. (1988). Small-angle scattering by fractal systems. *Journal of Applied Crystallography* 21: 781-785.

Terwinlliger, N.B. (1998). Functional adaptations of oxygen-transport proteins. *Journal of Experimental Biology* **201**: 1085–1098.

Truchot, J.P. (1980). Lactate increases the oxygen affinity of crab hemocyanin. *Journal of Experimental Biology* **214**: 205-208.
Truchot, J.P. (1992). Respiratory function of arthropod hemocyanins. *Advances in Comparative and Environmental Physiology* **13**, 377–410.

Uhlhorn, R.J.R., Keizer, K., Burggraaf, A.J. (1992). Gas transport and separation with ceramic membranes. Part II. Synthesis and separation properties of microporous membranes. *Journal of Membrane Science* **66**: 271-287.

Volbeda, A., Feiters, M.C., Vincent, M.G., Bouwman, E., Dobson, B., Kalk, K.H., Reedijk, J., Hol, W.G.J. (1989). Spectroscopic investigations of *Panulirus interruptus* hemocyanin in the crystalline state. *European Journal of Biochemistry* **181**: 669-673.

Wachter, B., Sartoris, F.J., Portner, H.O. (1997). The anaerobic endproduct lactate has a behavioural and metabolic signaling function in the shore crab. *Journal of Experimental Biology* **200**: 1015-1024.

Weber, R. E., Behrens, J. W., Malte, H., Fago, A. (2008). Thermodynamics of oxygenation-linked proton and lactate binding govern the temperature sensitivity of O2 binding in crustacean (*Carcinus maenas*) hemocyanin. *Journal of Experimental Biology* **211**:1057-1062.

West, J.W., LaTorre, G., Hench, L.L. (1996). The UV-visible spectrum in porous type VI silica: application and theory. *Journal of Non Crystalline Solids* **195**: 45-53.

Wheeler, K.E., Lees, N.S., Gurbiel, R.J., Hatch, S.L., Nocek, J.M., Hoffman, B.M. (2004). Electrostatic influence on rotational mobilities of sol-gel encapsulated solutes by NMR and EPR spectroscopies. *Journal of the American Chemical Society* **2004**: 13459-13463.

Yashina, E.I., Borisova, A.V, Karyakina, E.E., Shchegolikhina, O.I., Vagin, M.Y., Sakharov, D.A., Tonevitsky, A.G., Karyakin, A.A. (2010). Sol-gel immobilization of lactate oxidase from organic solvent: toward the advanced lactate biosensor. *Analytical Chemistry* **82**: 1601-1604.

Yoon, J., Fujii, S., Solomon, E.I. (2009). Geometric and electronic structure differences between the type 3 copper sites of the multicopper oxidases and hemocyanin/tyrosinase. *Proceedings of the National Academy of Science* **106**: 6585-6590.

Zhou, G., Ho, P.S., van Holde, K.E. (1989). An analytic solution to the Monod-Wyman-Changeux model and all parameters in this model. *Biophysical Journal* **55**: 275-280.

.

Supplementary materials

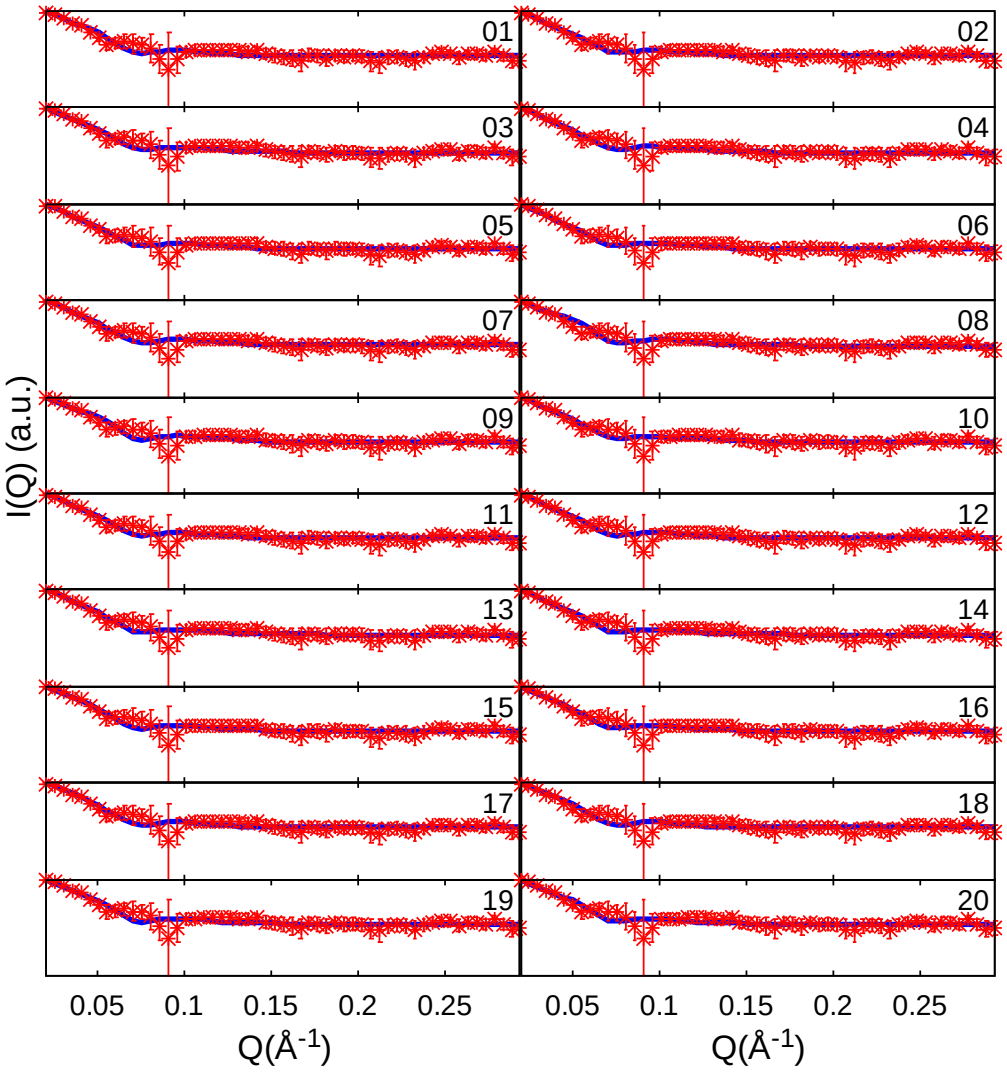

FIGURE 1. Independent QUAFIT fitting curves (20 runs) (in *blue*) of the SANS spectra of the oxygenated R-state (in *red*).

Subrun	χ^2	*k*	B	*α*	*β*	*γ*	*d*	*p*
1	0.31	0.31	2.23E-03	268.13	65.19	212.61	115.68	1.01
2	0.29	0.30	2.24E-03	259.22	36.00	204.20	109.40	1.01
3	0.31	0.32	2.23E-03	251.54	45.52	226.40	113.99	1.02
4	0.23	0.31	2.22E-03	233.86	19.08	210.52	98.58	1.09
5	0.26	0.30	2.24E-03	228.75	18.36	219.23	103.78	1.02
6	0.23	0.30	2.23E-03	219.84	14.05	170.06	99.14	1.07
7	0.23	0.30	2.23E-03	233.99	17.23	135.20	97.47	1.07
8	0.41	0.35	2.19E-03	283.12	21.44	79.74	123.70	1.07
9	0.32	0.33	2.20E-03	286.11	36.07	49.71	114.36	1.08
10	0.22	0.31	2.23E-03	289.77	10.77	71.74	98.98	1.10
11	0.26	0.31	2.23E-03	214.74	19.05	108.31	104.99	1.04
12	0.26	0.29	2.23E-03	248.75	44.95	46.97	102.24	1.02
13	0.24	0.30	2.24E-03	147.39	94.09	78.01	100.26	1.07
14	0.25	0.30	2.23E-03	161.67	96.50	148.70	101.37	1.07
15	0.24	0.29	2.24E-03	129.24	86.48	82.45	99.99	1.06
16	0.24	0.29	2.25E-03	122.53	82.96	47.87	100.77	1.05
17	0.23	0.29	2.23E-03	162.66	86.23	80.26	94.84	1.08
18	0.27	0.32	2.23E-03	300.76	89.79	67.92	105.75	1.10
19	0.29	0.32	2.22E-03	331.89	71.44	206.06	110.91	1.07
20	0.31	0.32	2.24E-03	356.12	57.96	237.29	116.79	1.03

TABLE 1. Fitting parameters of the SANS spectra of the oxygenated R-state, calculated through 20 independent QUAFIT runs. $\chi^2$is the goodness-of-fit value. *k* and B are the scaling factor and the flat background, respectively. *α, β* and *γ* are the three rotational axis of the two hexamers against each other; *d* is the interhexameric distance; *p* is the relative mass density of hydration water.

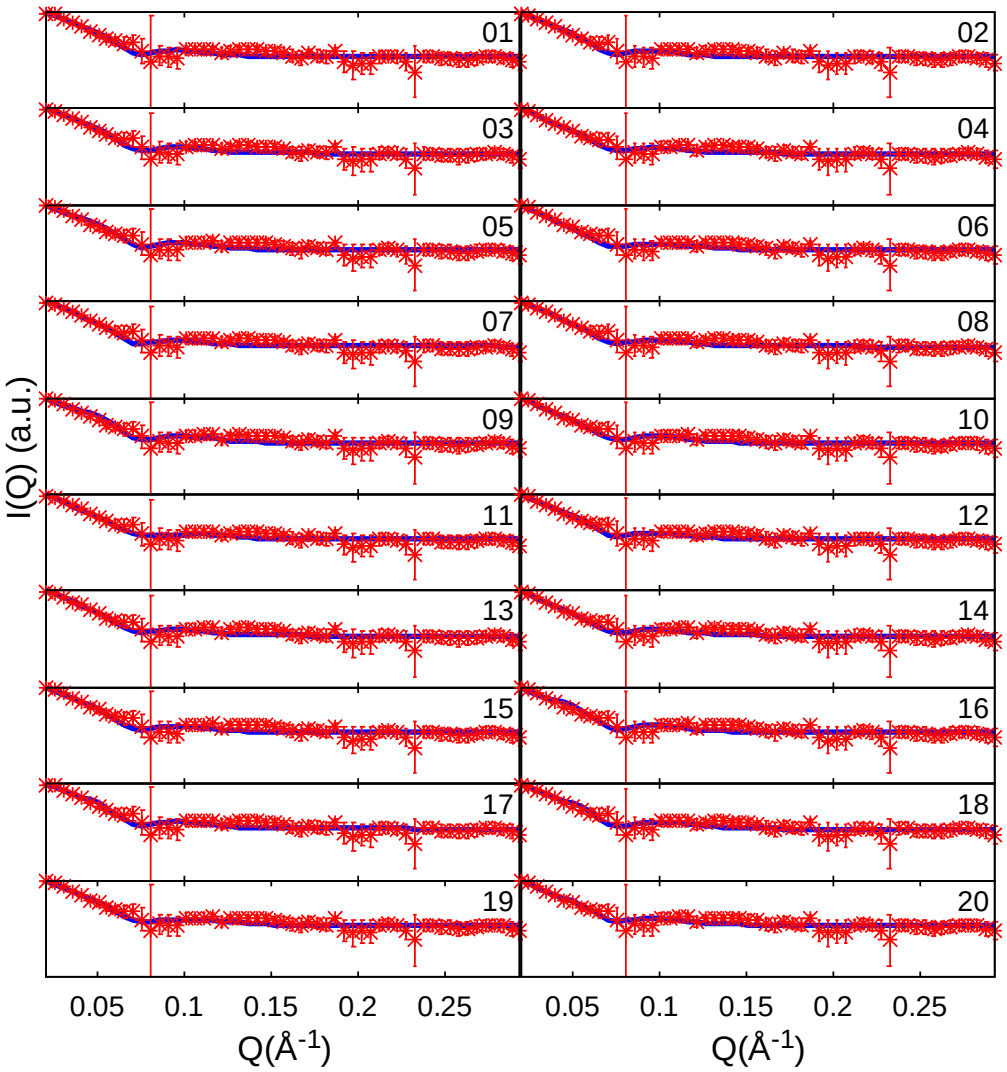

FIGURE 2. Independent QUAFIT fitting curves (20 runs) (in *blue*) of the SANS spectra of the deoxygenated R-state (in *red*).

Subrun	χ^2	*k*	B	*α*	*β*	*γ*	*d*	*p*
1	0.33	0.37	2.10E-03	254.36	60.74	230.31	103.72	1.04
2	0.35	0.36	2.12E-03	238.40	60.00	230.97	105.03	1.02
3	0.35	0.39	2.08E-03	233.55	72.96	208.24	107.10	1.09
4	0.35	0.37	2.12E-03	240.80	83.55	229.57	109.36	1.02
5	0.41	0.41	2.05E-03	239.18	46.21	274.39	111.93	1.10
6	0.33	0.34	2.14E-03	227.41	16.93	260.01	94.69	1.01
7	0.33	0.34	2.13E-03	237.26	70.51	224.45	98.43	1.02
8	0.32	0.36	2.09E-03	274.35	92.05	218.57	102.72	1.03
9	0.56	0.42	2.05E-03	310.99	135.70	173.95	124.36	1.07
10	0.34	0.34	2.09E-03	254.50	172.62	132.66	100.47	1.00
11	0.33	0.37	2.12E-03	270.92	172.62	66.72	105.82	1.01
12	0.35	0.38	2.10E-03	299.93	108.49	21.84	108.62	1.06
13	0.32	0.36	2.11E-03	253.73	67.37	14.82	101.31	1.04
14	0.33	0.35	2.12E-03	293.79	25.29	85.21	101.23	1.01
15	0.33	0.36	2.12E-03	358.24	75.87	202.71	101.99	1.03
16	0.51	0.42	2.05E-03	271.78	103.24	143.93	122.22	1.08
17	0.39	0.40	2.06E-03	214.41	103.41	209.78	112.14	1.09
18	0.40	0.41	2.06E-03	212.61	155.00	320.39	115.29	1.07
19	0.32	0.37	2.11E-03	165.40	163.84	324.77	104.72	1.03
20	0.33	0.38	2.08E-03	284.34	152.83	188.06	105.07	1.06

TABLE 2. Fitting parameters of the SANS spectra of the deoxygenated R-state, calculated through 20 independent QUAFIT runs. $\chi^2$is the goodness-of-fit value. *k* and B are the scaling factor and the flat background, respectively. *α, β* and *γ* are the three rotational axis of the two hexamers against each other; *d* is the interhexameric distance; *p* is the relative mass density of hydration water.

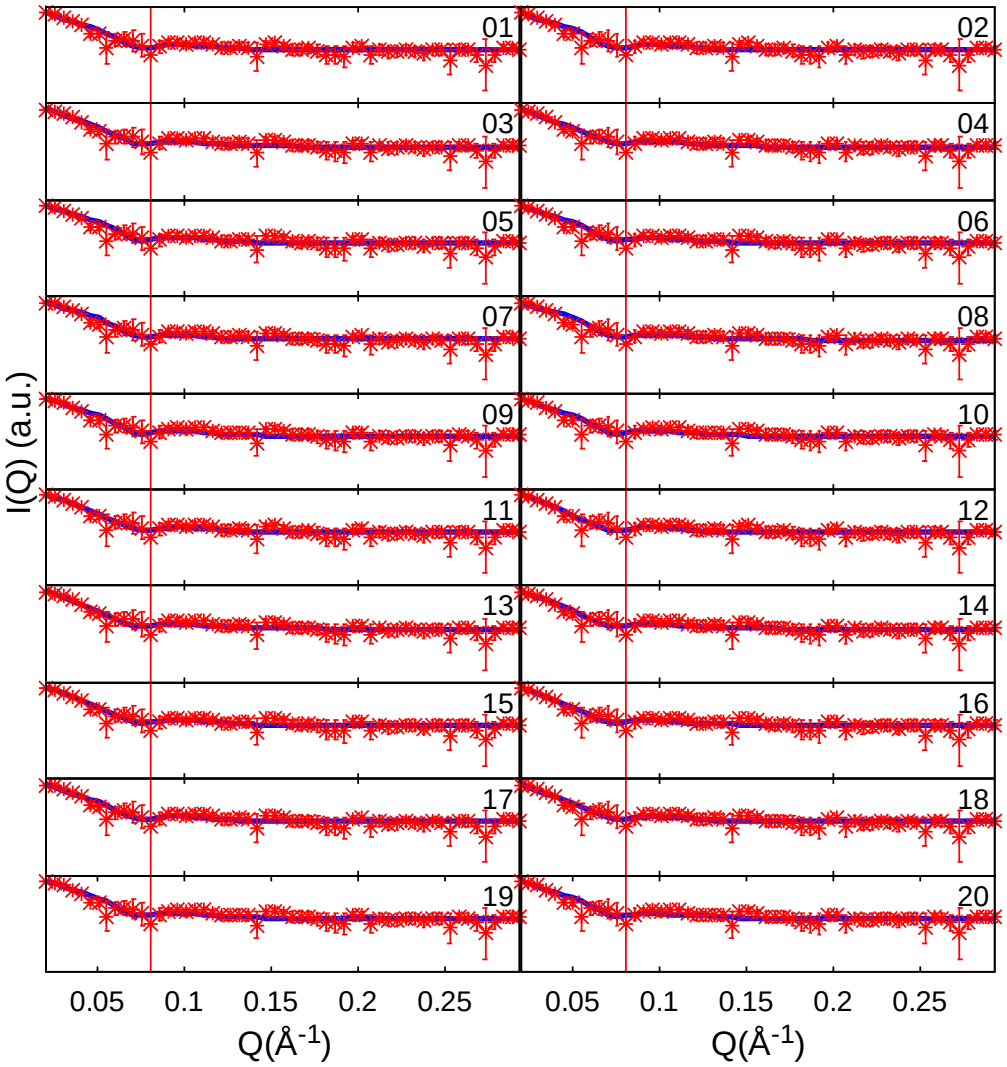

FIGURE 3. Independent QUAFIT fitting curves (20 runs) (in *blue*) of the SANS spectra of the oxygenated T-state (in *red*).

Subrun	χ^2	*k*	B	*α*	*β*	*γ*	*d*	*p*
1	0.48	0.37	2.22E-03	303.34	142.24	239.15	117.33	1.01
2	0.58	0.39	2.20E-03	272.11	130.74	231.99	121.07	1.06
3	0.40	0.36	2.23E-03	285.35	127.40	244.33	106.87	1.03
4	0.37	0.35	2.23E-03	341.04	153.98	241.08	105.11	1.01
5	0.52	0.40	2.19E-03	352.65	154.33	243.11	113.44	1.10
6	0.55	0.38	2.22E-03	342.00	131.33	231.44	123.47	1.00
7	0.64	0.39	2.23E-03	274.24	101.12	188.93	132.80	1.01
8	0.76	0.41	2.19E-03	197.60	25.60	150.07	132.73	1.05
9	0.48	0.37	2.23E-03	162.90	126.36	163.51	115.73	1.02
10	0.41	0.38	2.20E-03	208.93	151.13	124.41	109.68	1.02
11	0.37	0.34	2.24E-03	258.91	67.28	70.01	103.78	1.02
12	0.33	0.31	2.26E-03	181.12	27.26	0.30	96.52	1.04
13	0.33	0.32	2.26E-03	229.17	81.88	101.32	95.77	1.00
14	0.32	0.32	2.24E-03	350.24	86.42	104.81	90.28	1.04
15	0.31	0.33	2.24E-03	263.52	26.96	75.44	94.81	1.02
16	0.31	0.33	2.26E-03	264.35	20.92	9.71	91.26	1.05
17	0.40	0.36	2.22E-03	250.76	30.22	122.33	108.37	1.03
18	0.37	0.36	2.22E-03	236.68	28.06	295.08	104.16	1.04
19	0.45	0.36	2.22E-03	289.82	32.55	110.10	114.06	1.01
20	0.46	0.38	2.22E-03	326.29	34.17	2.67	111.50	1.06

TABLE 3. Fitting parameters of the SANS spectra of the oxygenated T-state, calculated through 20 independent QUAFIT runs. $\chi^2$is the goodness-of-fit value. *k* and B are the scaling factor and the flat background, respectively. α, β and γ are the three rotational axis of the two hexamers against each other; *d* is the interhexameric distance; *p* is the relative mass density of hydration water.

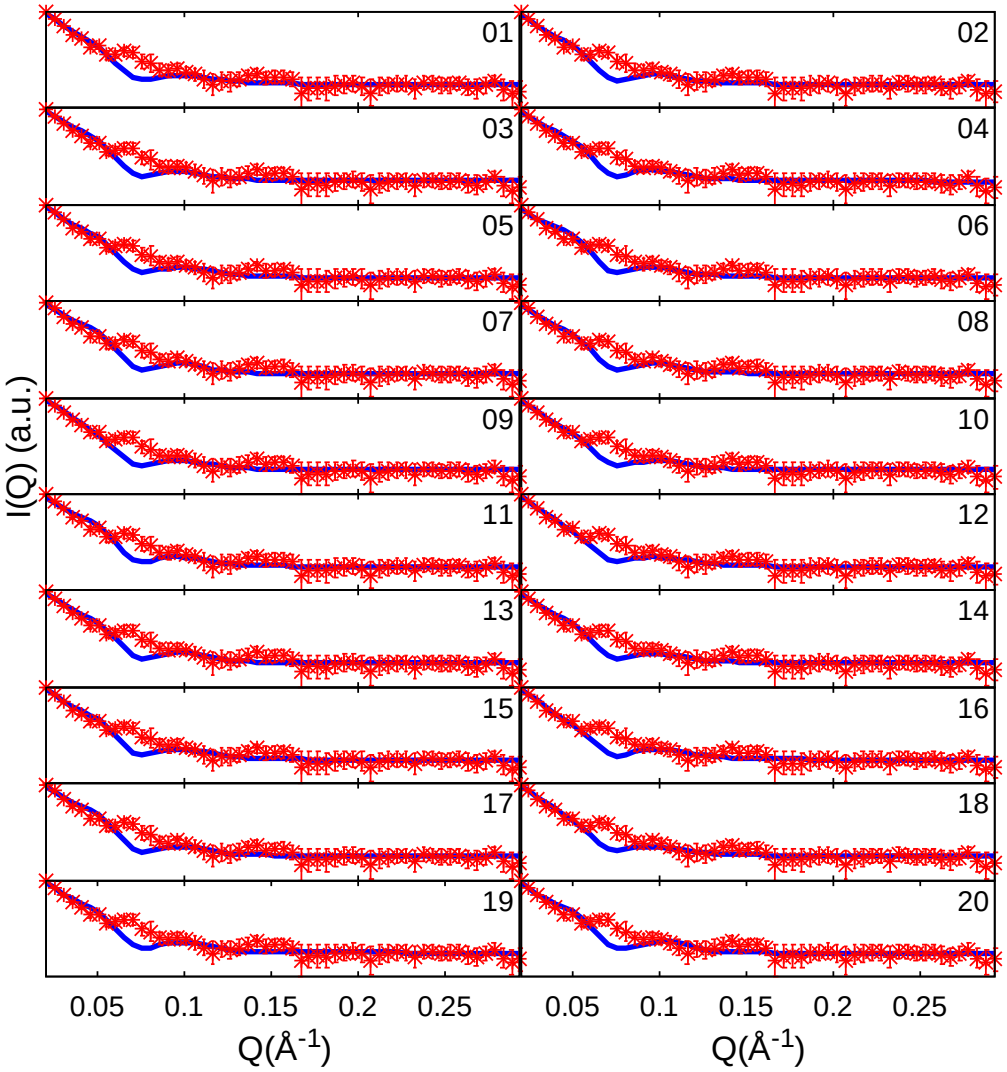

FIGURE 4. Independent QUAFIT fitting curves (20 runs) (in *blue*) of the SANS spectra of the deoxygenated T-state (in *red*).

Subrun	χ^2	*k*	B	*α*	*β*	*γ*	*d*	*p*
1	0.59	0.40	2.35E-03	267.08	86.20	216.63	106.67	1.03
2	0.66	0.43	2.32E-03	273.54	86.06	240.75	115.11	1.05
3	0.69	0.45	2.32E-03	266.30	107.46	236.57	125.59	1.01
4	0.65	0.45	2.29E-03	261.91	109.57	208.36	119.26	1.04
5	0.63	0.44	2.32E-03	307.93	134.60	184.17	121.27	1.02
6	1.02	0.47	2.29E-03	335.20	119.19	185.00	129.34	1.07
7	1.01	0.46	2.31E-03	329.04	82.56	167.53	132.58	1.05
8	0.69	0.44	2.32E-03	340.65	70.76	153.64	119.82	1.04
9	0.55	0.38	2.38E-03	353.58	69.47	153.20	111.97	1.01
10	0.57	0.41	2.34E-03	272.44	101.10	120.49	108.93	1.02
11	0.75	0.45	2.31E-03	281.67	76.93	240.09	127.34	1.02
12	0.56	0.38	2.36E-03	241.67	64.55	305.87	101.58	1.01
13	0.72	0.44	2.30E-03	267.69	116.11	287.45	114.58	1.08
14	0.73	0.44	2.32E-03	290.68	98.14	265.69	126.06	1.02
15	0.62	0.44	2.30E-03	301.64	39.48	296.65	121.09	1.01
16	0.53	0.38	2.36E-03	246.51	32.03	319.28	99.23	1.01
17	0.84	0.46	2.31E-03	98.26	57.18	255.46	125.34	1.06
18	0.60	0.39	2.37E-03	109.78	74.67	333.02	101.95	1.03
19	0.70	0.44	2.32E-03	152.99	62.40	336.77	125.41	1.01
20	0.62	0.47	2.28E-03	337.53	164.68	321.15	117.17	1.05

TABLE 4. Fitting parameters of the SANS spectra of the deoxygenated T-state, calculated through 20 independent QUAFIT runs. $\chi^2$is the goodness-of-fit value. *k* and B are the scaling factor and the flat background, respectively. *α, β* and *γ* are the three rotational axis of the two hexamers against each other; *d* is the interhexameric distance; *p* is the relative mass density of hydration water.

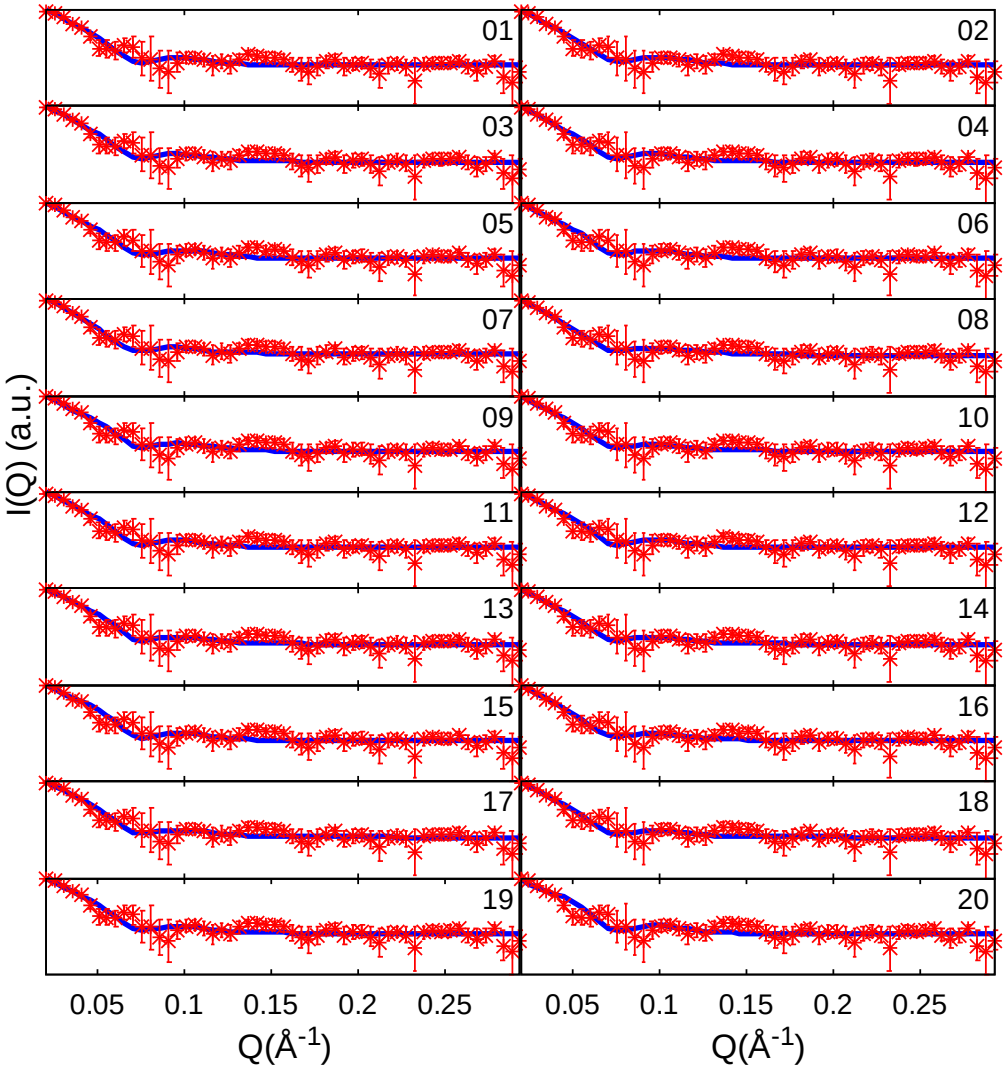

FIGURE 5. Independent QUAFIT fitting curves (20 runs) (in *blue*) of the SANS spectra of the oxygenated R-state in presence of 40mM L-lactate (in *red*).

Subrun	χ^2	*k*	B	*α*	*β*	*γ*	*d*	*p*
1	0.37	0.33	2.19E-03	309.59	100.25	234.99	98.24	1.04
2	0.37	0.34	2.15E-03	297.61	151.66	243.08	98.22	1.06
3	0.38	0.33	2.18E-03	299.81	123.60	262.79	97.93	1.03
4	0.38	0.33	2.17E-03	288.83	107.14	230.73	98.70	1.04
5	0.40	0.35	2.15E-03	306.80	149.62	251.86	101.45	1.06
6	0.44	0.36	2.15E-03	282.19	119.19	206.49	106.38	1.07
7	0.33	0.32	2.19E-03	291.19	172.61	212.60	87.35	1.05
8	0.35	0.32	2.20E-03	266.14	168.56	217.34	94.84	1.01
9	0.45	0.36	2.16E-03	202.68	146.18	257.68	109.95	1.03
10	0.39	0.34	2.18E-03	202.80	96.31	156.44	103.55	1.04
11	0.40	0.34	2.18E-03	234.06	81.70	191.66	99.73	1.07
12	0.41	0.35	2.14E-03	272.58	88.67	226.00	101.03	1.10
13	0.44	0.36	2.16E-03	318.78	82.34	344.77	109.30	1.06
14	0.37	0.33	2.17E-03	329.47	102.82	296.95	96.95	1.05
15	0.55	0.38	2.14E-03	300.60	85.22	214.99	119.27	1.08
16	0.36	0.32	2.19E-03	285.14	96.39	307.22	97.57	1.02
17	0.39	0.34	2.17E-03	313.11	105.41	291.42	101.37	1.04
18	0.38	0.33	2.19E-03	212.85	89.66	265.61	102.08	1.02
19	0.43	0.35	2.17E-03	50.16	103.66	276.44	109.79	1.03
20	0.66	0.40	2.14E-03	88.91	117.96	308.22	124.51	1.09

TABLE 5. Fitting parameters of the SANS spectra of the oxygenatged R-state in presence of 40mM L-lactate, calculated through 20 independent QUAFIT runs. $\chi^2$is the goodness-of-fit value. *k* and B are the scaling factor and the flat background, respectively. *α, β* and *γ* are the three rotational axis of the two hexamers against each other; *d* is the interhexameric distance; *p* is the relative mass density of hydration water.

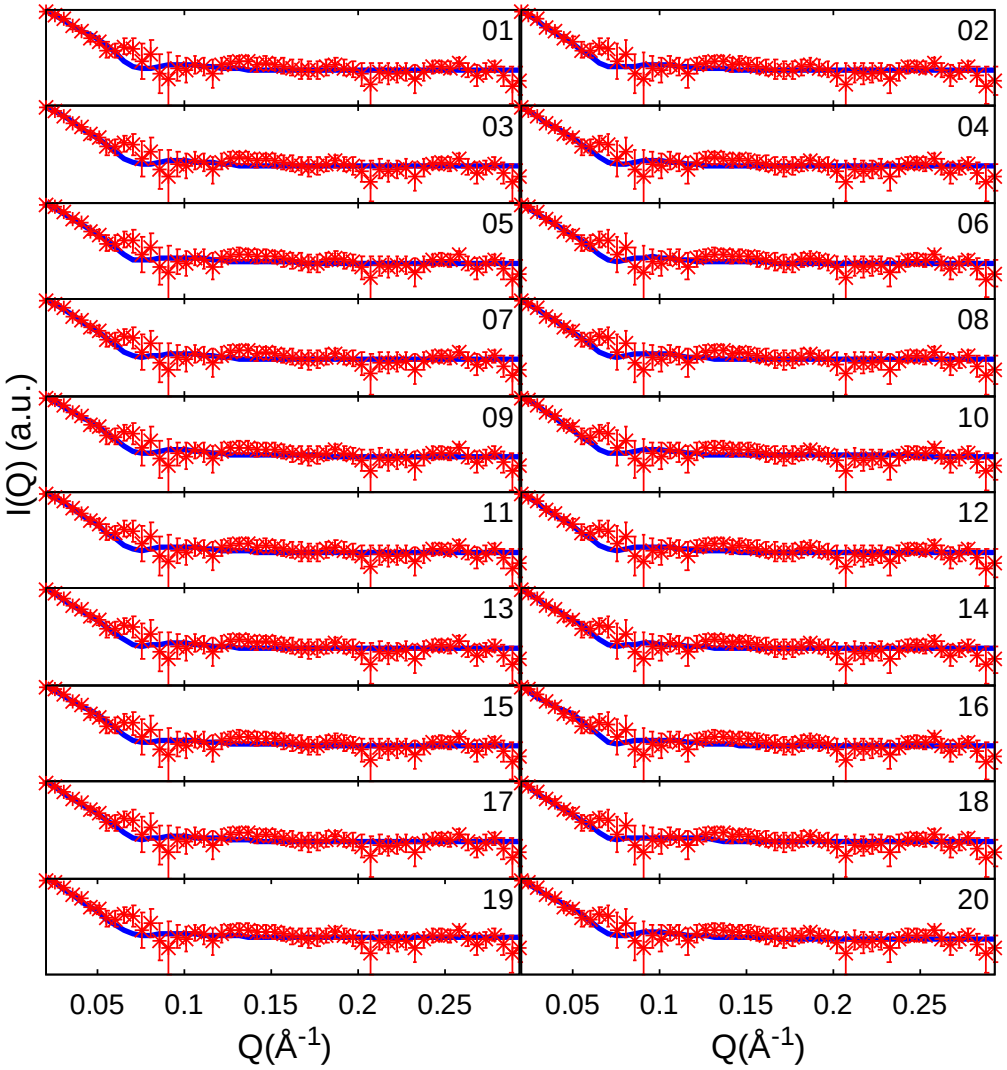

FIGURE 6. Independent QUAFIT fitting curves (20 runs) (in *blue*) of the SANS spectra of the deoxygenated R-state in presence of 40mM Lactate (in *red*).

Subrun	χ^2	*k*	B	*α*	*β*	*γ*	*d*	*p*
1	0.24	0.23	2.33E-03	273.35	97.56	275.13	114.03	1.09
2	0.22	0.19	2.36E-03	274.16	90.68	281.55	99.55	1.10
3	0.22	0.21	2.34E-03	270.90	93.66	277.06	100.27	1.08
4	0.22	0.21	2.34E-03	277.91	94.23	275.46	101.88	1.09
5	0.22	0.21	2.33E-03	282.02	102.69	284.41	103.07	1.09
6	0.23	0.22	2.34E-03	295.85	104.74	237.64	104.33	1.10
7	0.22	0.20	2.34E-03	283.43	103.96	257.71	99.70	1.07
8	0.23	0.20	2.35E-03	292.09	104.94	242.43	98.85	1.08
9	0.23	0.22	2.33E-03	290.65	115.86	244.07	105.04	1.09
10	0.23	0.18	2.36E-03	290.67	101.02	249.53	95.10	1.04
11	0.23	0.19	2.36E-03	314.52	99.36	246.99	99.51	1.04
12	0.24	0.19	2.36E-03	314.51	103.27	257.12	98.95	1.01
13	0.24	0.21	2.35E-03	298.86	117.25	328.56	106.74	1.04
14	0.23	0.22	2.34E-03	303.50	105.21	353.83	109.29	1.09
15	0.23	0.22	2.33E-03	245.91	85.80	339.58	113.40	1.08
16	0.27	0.22	2.33E-03	279.39	40.85	337.40	125.02	1.00
17	0.24	0.21	2.35E-03	298.37	29.83	337.44	108.27	1.02
18	0.24	0.21	2.35E-03	305.26	5.87	351.87	106.91	1.04
19	0.24	0.20	2.37E-03	330.30	18.13	356.50	96.24	1.04
20	0.24	0.22	2.32E-03	353.07	45.93	173.14	109.84	1.09

TABLE 6. Fitting parameters of the SANS spectra of deoxygenated R-state in presence of 40mM L-lactate, calculated through 20 independent QUAFIT runs. $\chi^2$is the goodness-of-fit value. *k* and B are the scaling factor and the flat background, respectively. *α, β* and *γ* are the three rotational axis of the two hexamers against each other; *d* is the interhexameric distance; *p* is the relative mass density of hydration water.

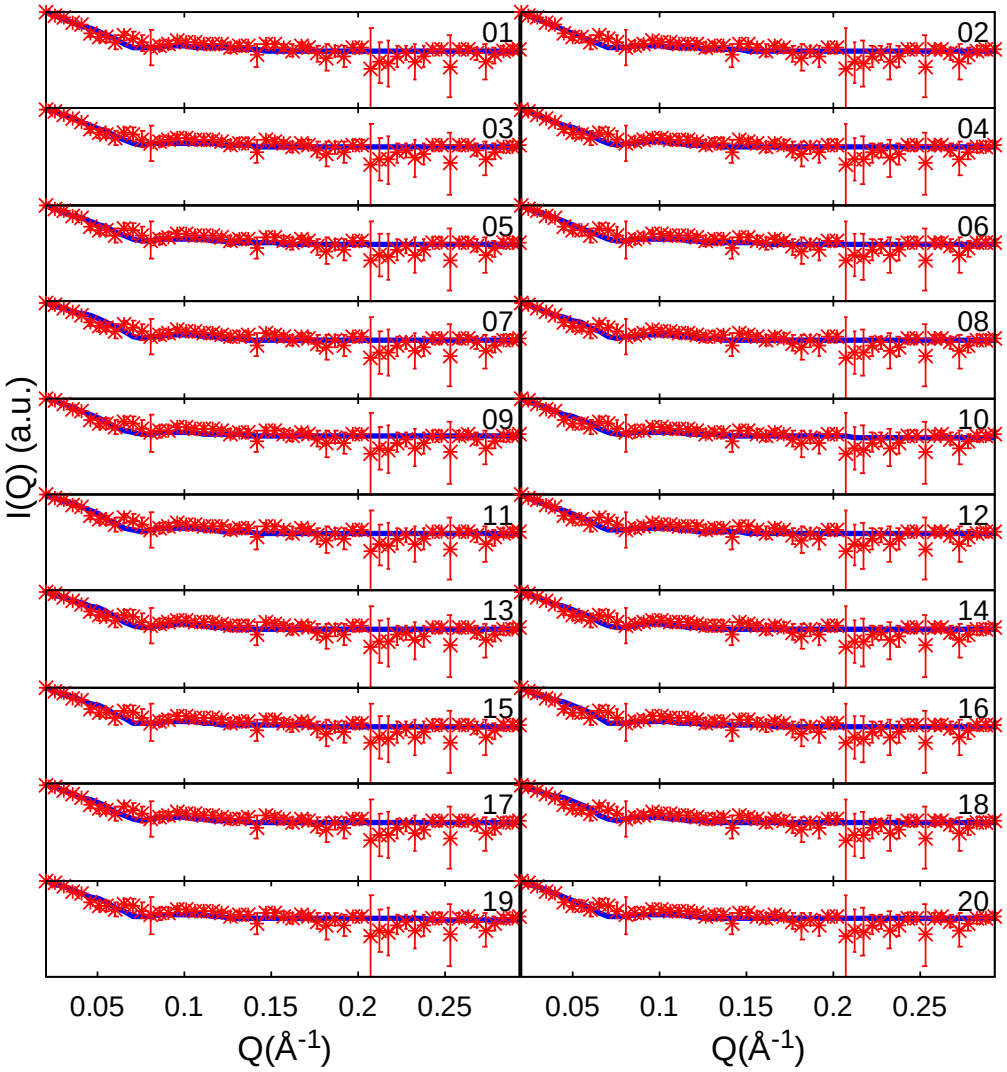

FIGURE 7. Independent QUAFIT fitting curves (20 runs) (in *blue*) of the SANS spectra of the oxygenated T-state (in *red*).

Subrun	χ^2	*k*	B	*α*	*β*	*γ*	*d*	*p*
1	0.39	0.35	2.11E-03	281.38	170.71	246.82	98.35	1.04
2	0.38	0.33	2.13E-03	289.07	167.02	229.39	94.35	1.04
3	0.41	0.35	2.11E-03	287.01	169.94	237.98	99.16	1.08
4	0.42	0.34	2.09E-03	292.60	139.00	207.45	98.76	1.08
5	0.42	0.35	2.10E-03	317.89	156.07	214.40	107.90	1.03
6	0.41	0.35	2.10E-03	280.59	158.11	207.42	103.63	1.06
7	0.60	0.38	2.09E-03	295.44	134.15	185.65	121.52	1.06
8	0.45	0.37	2.08E-03	259.57	160.47	170.06	106.69	1.09
9	0.38	0.32	2.13E-03	252.21	159.92	56.16	94.46	1.03
10	0.44	0.35	2.12E-03	213.74	153.51	3.23	107.10	1.04
11	0.47	0.30	2.10E-03	283.71	99.56	8.51	101.48	1.09
12	0.42	0.33	2.11E-03	279.56	75.97	39.84	104.99	1.01
13	0.56	0.37	2.10E-03	268.46	90.20	48.36	124.17	1.02
14	0.48	0.36	2.11E-03	183.82	77.92	240.95	115.59	1.01
15	0.47	0.35	2.11E-03	175.27	82.20	303.96	110.22	1.04
16	0.54	0.37	2.11E-03	107.60	64.94	248.22	115.60	1.06
17	0.44	0.34	2.12E-03	299.86	103.91	358.06	98.22	1.07
18	0.63	0.39	2.08E-03	289.68	68.34	194.69	122.69	1.08
19	0.45	0.35	2.10E-03	260.47	74.27	147.50	103.86	1.06
20	0.44	0.34	2.13E-03	197.08	91.40	90.46	107.14	1.02

TABLE 7. Fitting parameters of the SANS spectra of the oxygenated T-state in presence of 40mM L-lactate, calculated through 20 independent QUAFIT runs. $\chi^2$is the goodness-of-fit value. *k* and B are the scaling factor and the flat background, respectively. α, β and γ are the three rotational axis of the two hexamers against each other; *d* is the interhexameric distance; *p* is the relative mass density of hydration water.

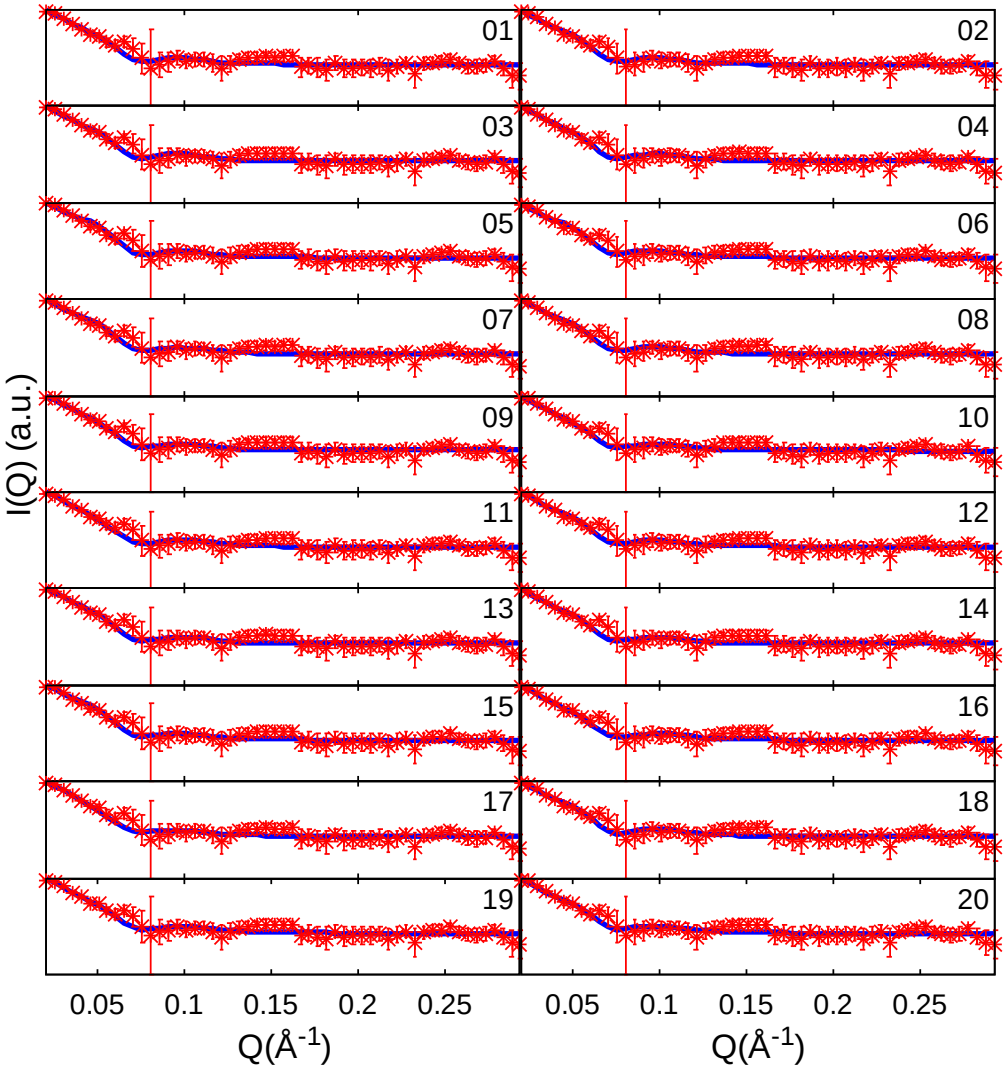

FIGURE 8. Independent QUAFIT fitting curves (20 runs) (in *blue*) of the SANS spectra of the deoxygenated T-state in presence of 40mM L-Lacate (in *red*).

Subrun	χ^2	*k*	B	*α*	*β*	*γ*	*d*	*p*
1	0.37	0.32	2.32E-03	283.51	67.09	210.68	113.58	1.02
2	0.41	0.34	2.31E-03	279.88	75.02	212.13	123.68	1.03
3	0.38	0.33	2.32E-03	261.21	63.66	193.78	115.61	1.04
4	0.33	0.32	2.31E-03	243.36	64.95	168.57	106.46	1.09
5	0.48	0.36	2.30E-03	269.92	82.40	180.74	128.51	1.07
6	0.44	0.33	2.32E-03	210.66	57.90	182.89	126.05	1.00
7	0.45	0.34	2.31E-03	146.28	50.67	179.69	126.09	1.02
8	0.42	0.34	2.31E-03	139.81	71.18	177.45	123.06	1.05
9	0.34	0.32	2.33E-03	117.12	74.92	157.43	108.74	1.06
10	0.36	0.32	2.33E-03	177.03	112.68	166.61	111.06	1.04
11	0.32	0.30	2.32E-03	172.75	147.71	193.60	96.89	1.07
12	0.37	0.34	2.31E-03	238.41	99.81	188.80	115.06	1.08
13	0.34	0.32	2.32E-03	326.54	98.09	252.33	109.51	1.07
14	0.36	0.32	2.33E-03	303.85	99.11	168.75	113.14	1.05
15	0.40	0.34	2.31E-03	238.35	93.19	103.98	122.66	1.05
16	0.36	0.31	2.34E-03	336.78	89.96	45.57	111.47	1.03
17	0.36	0.29	2.37E-03	294.03	96.06	22.84	101.01	1.00
18	0.38	0.34	2.29E-03	328.70	128.88	162.62	114.52	1.10
19	0.39	0.31	2.34E-03	118.27	36.26	33.49	112.57	1.00
20	0.39	0.33	2.31E-03	27.94	33.48	154.00	117.27	1.04

TABLE 8. Fitting parameters of the SANS spectra of the deoxygeanated T-state in presence of 40mM L-lactate, calculated through 20 independent QUAFIT runs. $\chi^2$is the goodness-of-fit value. *k* and B are the scaling factor and the flat background, respectively. α, β and γ are the three rotational axis of the two hexamers against each other; *d* is the interhexameric distance; *p* is the relative mass density of hydration water.

Multiple sequence alignment (CLUSTALW): arthropod hemocyanin.

is a *cod number* that allow to correlate each sequence to the name of the species. The sequences **# 6**,**7** and **45** (in bold) are those of the subunit *a* and *c* of *Panulirus interruptus* and the one of the subunit CaeSS2 of *Carcinus aestuarii*, respectively. In *green*: His302; in *red*: Tyr339; in *orange*: His344; in *blue*: non-conserved AA.

```
#
3  ------------------------------------------------------
22 APHTSYKYGG-EFPTRPDNKNFEDVDG------VARIRDLKEMENRIRDAIAHGYADN 320
21 APHTSYKYGG-EFPTRPDNKNFEDVNG------VARIRDMKIMESRIRDAIAHGYADN 320
1  APHTMY------------------------------------------------- 239
44 APHTMYKYGG-YFPSRPDNVNFEDVDG------VARVRDMLILESRIRDAIAHGYFTG 330
2  ------------------------------------------------------
20 DPQAMYKYGG-YFPSRPDNIHFEDVDG------VADVRDMLLYEERILDAIAHGYVRD 325
18 APHTMYKYGG-YFPSRPDNVHFEDVDG------VARVRDMLILESRIRDAIAHGYVTG 330
19 APHTMYKYGG-YFPSRPDNVHFEDVDG------VARVRDMLILESRIRDAIAHGYVTG 329
17 VPHTMYKYGG-YFPSRPDNVHFEDVDG------VARVRDMLILESRIRDAIAHGYVTG 330
45 APHTSYKYGG-YFPDRPDNVNFEDVDG------VARVRDMLLFEERIQDAIAHGYLR- 307
12 ------------------------------------------------------
39 APHTTYKYGG-QFPSRPDNVNFEDVDG------VARIRDLLIVESRIRDAIAHGYIID 330
6  APHTAYKYGG-YFPSRPDNVHFSDVDG------VARVRDMSMTEDRIRDAIAHGYIDA 313
5  APHTTYKYGG-QFPSRPDNVDFEDVDG------VARIRDLLIVESRIRDAIAHGYIVD 335
25 APHTTYKYGG-QFPSRPDNVDFDDMDG------VARIRDLLIIESRIRDAIAHGYIVD 325
23 APHTTYKYGG-QFPSRPDNVRFEDVDG------VARIRDLLIVESRIRDAIAHGYIVD 171
8  APHTSYKYGG-EFPVRPDNIRFENVDG------VAHVHDMEITENRIRDAIAHGYITA 336
11 APHTSYKYGG-EFPVRPDNIRFEDVDG------VAHVHDMEITENRIRDAIAHGYITA 335
9  APHASYKHGG-EFPTRPDNIRFKNVDG------VARVHDMEITESRIRDAIAHGYITA 335
10 APHASYKYGG-EFPTRPDNTQFKNVDG------VARVRDMEITESRIRDAIAHGYITA 335
7  APLTSYKYGG-EFPVRPDNIHFEDVDG------VAHVHDLEITESRIHEAIDHGYITD 307
36 ------------------------------------------------------
37 APHTSYKYGG-EFPARPDNVHFEDVDG------VAHVRDMIIESRIRDAIAHGYVTD 323
13 APHTSYKFGG-EFPARPDNVHFEDVDG------VARVRDMVILESRIRDAIAHGYIID 336
24 APHTIYKYGG-EFPARPDHIHFEDVDG------VARVRDMIIMESRIHDAISHGYITD 319
40 APHTIYKYGG-EFPARPDHIHFEDVDG------VARVRDMVITESRIRDAIAHGYITG 319
14 APHTSYKYGG-EFPARPDNVHFEDVDG------VAHVRDMVIVESRIRDAIAHGYVTD 198
38 APHTTYRYGG-EFPTRPDHVNFEDVDG------LVRVRDMIIHETRIRDAIAHGYITA 327
43 APHTTYRYGG-EFPARPDNVNFEDVDG------AVRVRDMIVHETRIRDAIAHGYITS 328
4  APHTTYKYGG-EFPSRPDNVHFSDVDG------IARIRDLIITESRIRDAIAHGYVTG 127
42 APHTTYKFGG-EFPSRPDNVRFEDVDG------VARIRDMIIYESRIRDAIAHGYVTA 331
41 APHTTYKFGG-EFPSRPDNVRFEDVDG------VARIRDMIIYESRIRDAIAHGYVTA 326
31 APHTTYKYGG-EFPARPDNVNFEDVDG------VARIRDMVIFETRIRDAIAHGYVTA 332
32 APHTTYKYGG-EFPARPDNVNFEDVDG------VARIRDMVIFETRIRDAIAHGYVTA 322
33 APHTTYKYGG-EFPARPDNVNFEDVDG------VARIRDMIIIETRIRDAIAHGYVTA 331
34 APHTTYKYGG-EFPARPDNVNFEDVDG------VARIRDMIIYETRIRDAIAHGYITG 331
15 APHTSYKYGG-EFPFRPDNKEFEDVDG------VAHIRDMKEIESRIRDAIAHGYITN 195
16 APHTTYRHGG-EFPSRPDNIDFEDVDG------VARVRDMKIMENRIRDAIAHGYIEN 323
27 SAHLTSLVSGLHYASRPEGMHLHDLKG------VVNLHDMERWRERIMDAIERGLVYD 286
30 SAHLTSLVSGLHYASRPEGLHIRDLN-------DVSLQEMERWRERILEGINLGHVHD 285
28 SPHLTSLISGLNYGTRPDGLKLHDLH-------DVTIQDMERWRERIHDAIDLKMVHD 284
29 APHLTHVASGKYYSPRPDGLKLRDLG-------DIEISEMVRMRERILDSIHLGYVIS 288
26 SSHLSSSINGLPYPSRPDGMTLQDLK-------EVSVQDLERWRDRISDAIHIGHVED 289
35 FSKLTVNNSGRAWGTRQDNTFLKDFRRNDFGLQPLDITELEVWRSRLLDAIHQGYMKN 318
```

```
#
3  ------------------------------------------------------------
22 DGTHLDINN-----DEGINVLGAAIESSTS-SIHPSYYGALHNQAHRVLGQQADPHGKF 374
21 DGTHLDINN-----DEGINVLGAAIESSTS-SIHPSYYGALHNQAHRVLGQQADPHGKF 374
1  ------------------------------------------------------------
44 DGSVISIRD-----AHGIDILGDVIESSTY-SPNPEYYGSLHNTAHVMLGRQGDPHGKF 384
2  ------------------------------------------------------------
20 NGKIVDLRN-----NDGIDVLGDVIESSLY-SPNPQYYGALHNTAHMMLGRQGDPHGKF 379
18 DGSIISISD-----SHGIDVLGDVIESSLY-SPNPEYYGALHNTAHMMLGRQGDPHGKF 384
19 DGSIISISD-----SHGIDVLGDVIESSLY-SPNPEYYGALHNTAHMMLGRQGDPHGKF 383
17 DGSIISISD-----SHGIDVLGDVIESSLY-SPNPEYYGALHNTAHMMLGRQGDPHGKF 384
45 NGSTINIRD-----NHGIDVLGDVFESSMY-SPRQDYYGALHNQAHRVLGSQADPHGKF 361
12 ------------------------------------------------------------
39 QGNRIDIMN-----ERGIDILGDIIESSMY-SPNVQYYGALHNTAHIVLGRQADPHGKY 384
6  DGHSIDIMN-----SHGIEFLGDIIESSGY-SANPGFYGSLHNTAHIMLGRQGDPTGKF 367
5  AGNHIDIMN-----ERGIDVLGDVIESSLY-SPNVQYYGALHNTAHIVLGRQSDPHGKY 389
25 VGNHIDIMN-----ERGIDVLGDVIESSLY-SPNVQYYGALHNTAHIVLGRQSDPHGKY 379
23 EGKHIDIMN-----ERGIDVVGDIIES------------------------------ 194
8  DGHTIDIRQ-----PNGIELLGDIIESSMY-SSNPHYYGSLHNTAHMMLGRQGDPHGKF 390
11 DGHTIDIRQ-----PNGIELLGDIIESSMY-SSNPHYYGSLHNTAHMMLGRQGDPHGKF 389
9  DGHTIDIRQ-----PNGIELLGDIIESSMY-SSNPHYYGSLHNTAHMMLGRQGDPHGKF 389
10 DGHTIDIRQ-----PNGIELLGDIIESSMY-SSNPQYYGSLHNTAHMMLGRQGDPHGKF 389
7  DGHTIDIRQ-----PKGIELLGDIIESSKY-SSNVQYYGSLHNTAHVMLGRQGDPHGKF 361
36 ------------------------------------------------------------
37 HGDNINIRN-----DHGIDVLGDIIESSVY-SPNAQYYGALHNTAHIMLGRQGDPHGKF 377
13 SGNKIDIKN-----EHGIDTLGDIIESSVY-SPNVQYYGALHNTAHIMLGRQGDPHGKF 390
24 DGKVIDIMN-----DEGIDKLGDIIESSMY-SPNAQYYGALHNTAHVMLGRQGDPHGKY 373
40 DGKVIDIMN-----DQGVDKLGDIIESSMY-SPNVQYYGALHNMAHIMLGRQGDPHGKY 373
14 EGHHINIRN-----DHGIDILGDIIESSVY-SPNAQYYGALHNTAHIMLGRQGDPHGKF 252
38 DGSHININD-----EHGIDHLGDIIESSLY-SPNAQYYGALHNEAHIILGRQADPHGKF 381
43 DGSRVDIRD-----ENGINLLGDIIESSVY-SLNAGYYGALHNDAHILLGRQSDPHGKF 382
4  DGERKDIRN-----EHGIEILGDVIESSEY-SPNPEYYGALHNLAHIVLGRQGDPHGKF 181
42 DGSHIDIRN-----EHGIDVLGDVIESSTY-SPNAGYYGALHNLAHIILGRQGDPHGKF 385
41 DGSHIDIRN-----EHGIDVLGDVVESSTY-SPNAGYYGALHNLAHIILGRQGDPHGKF 380
31 DGSKIDIRN-----EHGIDILGDVIESSVY-SPNPGYYGALHNLAHIILGRQGDPHGKF 386
32 DGSKIDIRN-----EHGIDILGDVIESSVY-SPNPGYYGALHNLAHIILGRQGDPHGKF 376
33 DGSKIDIRN-----EHGIDVLGDVIESSVY-SPNAGYYGALHNLAHIILGRQGDPHGKF 385
34 NGEKIDIRN-----ENGIDILGDVIESSVY-SPNAGYYGALHNLAHIILGRQGDPHGKF 385
15 DGSHTDIDN-----DHGIDVLGDIMESSTY-STNVAYYGALHNQAHRILGAQSDPHHKF 249
16 HDEHISLNN-----THGIDILGDLIESSVY-SPNAQYYGALHNLAHIMLGRQADPHGKY 377
27 HGHEHKLEE-----PHGIDILGAMIESSHD-SLNHEFYGSIHNWGHVMFARLHDPDGRY 340
30 HGKEVELDE-----EHGIDILGALIESSHE-SKNEEYYGSLHNWGHVMLARVHDHDGRF 339
28 HGKEVAVDD-----EHGIDILGALVESSHE-SVNQGFYGSLHNWGHVLTARAHDPEGKF 338
29 DGSHKTLDE-----LHGTDILGALVESSYE-SVNHEYYGNLHNWGHVTMARIHDPDGRF 342
26 NGSHVPLDD-----TRGIDILGAMVEASYE-SINQAFYGSIHNWGHVISARVLDPDGRY 343
35 NGDTIPLSDDVTSGKRGIDILGDTLEADADLSPHYQFYGDLHNMSHVLISFSHDNDNAH 378
```

#	
1	*Portunus pelagicus* subunit 4
2	*Portunus pelagicus* subunit 3
3	*Portunus pelagicus* subunit 1
4	*Porcellio scaber*
5	*Penaeus monodon*
6	*Panulirus interruptus* subunit c
7	*Panulirus interruptus* subunit a
8	*Palinurus elephas* subunit 4
9	*Palinurus elephas* subunit 3
10	*Palinurus elephas* subunit 2
11	*Palinurus elephas* subunit 1
12	*Palaemonetes varians*
13	*Pacifastacus leniusculus*
14	*Nephrops norvegicus* I
15	*Nephrops norvegicus* II
16	*Nebalia kensleyi*
17	*Metacarcinus magister* subunit 6
18	*Metacarcinus magister* subunit 5
19	*Metacarcinus magister* subunit 4
20	*Metacarcinus magister* subunit 3
21	*Metacarcinus magister* subunit 2
22	*Metacarcinus magister* subunit 1
23	*Marsupenaeus japonicus*
24	*Macrobrachium nipponense*
25	*Litopenaeus vannamei*
26	*Limulus polyphemus* subunitVI
27	*Limulus polyphemus* subunit IIIb
28	*Limulus polyphemus* subunit IIIa
29	*Limulus polyphemus* subunit II
30	*Limulus polyphemus* subunit IV
31	*Limnoria quadripunctata* HC4
32	*Limnoria quadripunctata* HC3
33	*Limnoria quadripunctata* HC2
34	*Limnoria quadripunctata* HC1
35	*Homarus gammarus*
36	*Homarus americanus* beta subunit
37	*Homarus americanus* alpha subunit
38	*Gammarus roeselii* subunit 1
39	*Fenneropenaeus chinensis*
40	*Exopalaemon carinicauda*
41	*Eurydice pulchra* subunit 2
42	*Eurydice pulchra* subunit 1
43	*Cyamuss cammoni*
44	*Callinectes sapidus*
45	Carcinus aestuarii subunit *CaeSS2*

Acknowlegments

My first appreciation goes to my supervisor Prof. Mariano Beltramini for his help and support in all stages of this thesis.
I would like to thank also Prof. Luigi Bubacco, that has contributed to this thesis with his insightful comments.
My sincere thanks also go to Prof. Francesco Spinozzi and Dr.ssa Maria Grazia Ortore of the Marche Polytechnic University, for their fundamental help in the elaboration of the SAX and SANS spectra.
My sincere gratitude to Prof. Gerard Canters of Physics Department of the University of Leiden (Netherlands) and Dr. Leandro Tabares for training me for the sol-gel technique.
Also, I want to thank Olivier Mathon of beamline ID24 at ESRF, Lionel Porcar of beamline D22 at ILL, José Texeira of beamline PAXE at LLB and Heinz Amenitsch of ELETTRA for their suggestions to improve XAS, SANS and SAXS measurements.
Finally, I would like to thank all the people of my laboratory, in particular Dr. Paolo Di Muro for his helpful hand when needed.